NASA-CR-137880

COPY ON MICROFICHE

Fiche-NASA N77-14296

COST ITEM

CR 137880

(NASA-CR-137880) PREENTRY COMMUNICATION DESIGN ELEMENTS FOR OUTER PLANETS ATMOSPHERIC ENTRY PROBE (Hughes Aircraft Co.) 125 p HC A06/MF A01 CSCL 17B

N77-14296

Unclas

G3/32 56988

DO NOT DESTROY
RETURN TO LIBRARY

JULY 1976

PREENTRY COMMUNICATION DESIGN ELEMENTS FOR OUTER PLANETS ATMOSPHERIC ENTRY PROBE

NASA Contract NAS-2-9008

3 MAY 1977
MCDONNELL DOUGLAS
RESEARCH & ENGINEERING LIBRARY
ST. LOUIS

JAN 1977
RECEIVED
NASA STI FACILITY
INPUT BRANCH

HUGHES
HUGHES AIRCRAFT COMPANY
SPACE AND COMMUNICATIONS GROUP

N77-13003

CR 137880

JULY 1976

PREENTRY COMMUNICATION DESIGN ELEMENTS FOR OUTER PLANETS ATMOSPHERIC ENTRY PROBE

NASA Contract NAS-2-9008

This report and the study leading to it correspond to Task 4 1 3 of the Outer Planet Atmospheric Entry Probe Support Research and Technology Study

HUGHES
HUGHES AIRCRAFT COMPANY
SPACE AND COMMUNICATIONS GROUP

Page intentionally left blank

Page intentionally left blank

CONTENTS

		Page
1.	INTRODUCTION AND SUMMARY	
	1.1 Link Analysis and Design	1-1
	1.2 System Conceptual Design	1-2
	1.3 Doppler Measurement Analysis	1-2
	1.4 Electronically Despun Antenna	1-3
2.	LINK ANALYSIS AND DESIGN	
	2.1 Environmental Factors	2-3
	2.1.1 Atmospheric Attenuation	2-3
	2.1.2 Ionospheric Scintillation	2-5
	2.1.3 Noise Temperature	2-7
	2.2 Transmission Frequency	2-11
	2.2.1 Fixed Gain Antennas	2-13
	2.3 System Implementation Factors	2-13
	2.3.1 Receiver Noise	2-14
	2.3.2 Transmitter Power	2-14
	2.3.3 Probe Antenna Pattern	2-14
	2.3.4 Spacecraft Antenna Pattern	2-15
	2.4 Link Studies and Performance Analysis	2-15
	2.4.1 Trajectory Parameters	2-19
	2.4.2 Carrier Frequency	2-19
	2.4.3 Preentry and Entry	2-19
	2.4.4 Probe Lead Time	2-21
	2.4.5 Spacecraft Antenna Beamwidth	2-21
	2.4.6 Spacecraft Antenna Squint Angle	2-27
	2.4.7 Probe Beamwidth	2-27
	2.4.8 Higher Latitude Entry	2-27
	2.5 Comments and Conclusions	2-36
	2.6 References	2-37
3.	SYSTEM CONCEPTUAL DESIGN	3-1
4.	DOPPLER MEASUREMENT ANALYSIS	
	4.1 Introduction and Summary	4-1
	4.2 Probe Transmitter Options	4-2
	4.3 Operational Environment Assumptions	4-5
	4.3.1 Doppler Shift and Doppler Rate	4-5
	4.3.2 Scintillation Environment	4-7
	4.3.3 Scintillation Computer Modeling	4-8
	4.4 Spacecraft Receiver Carrier Tracking Simulation	4-9
	4.4.1 System Configuration Assumptions	4-9
	4.4.2 Simulation Parameter Assumptions	4-15
	4.4.3 Simulation Input Characterization	4-19
	4.4.4 Simulation Verification	4-21
	4.4.5 Carrier Tracking Simulation Results	4-21

4.5	Doppler Extractor Configuration	4-33
4.6	Counter/Resolver Limitations	4-35
4.7	Summary and Conclusions	4-40
4.8	References	4-40
5.	ELECTRONICALLY DESPUN ANTENNA	
5.1	Array Element	5-3
5.1.1	Design	5-3
5.1.2	Radiation Characteristics	5-3
5.1.3	Construction and Weight	5-3
5.2	General Array Analysis	5-5
5.3	Discussion of Array Pattern Results	5-9
5.4	Electronics	5-23
5.4.1	Description	5-23
5.4.2	Phase-Jump and Loop Stability	5-26
5.4.3	Physical Description	5-26
5.4.4	Development Considerations	5-29
5.5	Summary	5-29
APPENDIX		A-1

1. INTRODUCTION AND SUMMARY

This study dealt with four related tasks associated with data transmission from a probe prior to entering the atmosphere of Jupiter to an orbiting spacecraft in a trajectory past the planet: 1) link analysis and design, 2) system conceptual design, 3) doppler measurement analysis, and 4) an electronically despun antenna. For tasks 1, 3, and 4, an analytical approach was developed and combined with computational capability available at Hughes to produce quantitative results corresponding to requirements and constraints given by NASA, ARC. One constraint having a major impact on the numerical results of the link analysis was the assumption of a nonsteerable antenna on a spinning orbiter. Other constraints included the interplanetary trajectory and the approach trajectory. Because the Jupiter Orbiter Probe (JOP) program is currently in a state of evolution, all requirements and constraints applied during this study are subject to change. However, the relationships of parameters as developed here will remain valid and will aid in planning Jupiter missions. Thus, the value of this study lies in a combination of the technical approaches developed and the quantitative results produced. The above four tasks are treated successively in the following four sections but brief introductions are presented here

1.1 LINK ANALYSIS AND DESIGN

Both the probe and orbiter are moving with respect to each other and with respect to the planet Jupiter; thus, an analytical approach was selected to allow link capacity to be computed as a function of time. A computer program was employed to calculate aspect angles and distances as a function of time for each set of mission and trajectory parameters of interest. Also included in this program are analytical models of antenna patterns and environmental effects with which the computed geometrical quantities and other input parameters are combined to simultaneously yield a computation of link margin as a function of time. This approach allows the effect of parameters for the communication system, environmental models, and trajectories to be determined and their relationships developed.

The link margin as a function of time for one set of parameters was compared with that for another set. For the mission parameters and constraints given by NASA, ARC (near equatorial flyby and probe trajectory, periapsis distance = 1.8 R_j), a nominal set of optimum antenna and approach

trajectory parameters was selected as follows: 1) probe antenna beamwidth = 70°, 2) orbiter antenna beamwidth and peak gain aspect angle (squint angle) with respect to the orbiter spin axis = 60° and 45°, respectively, and 3) probe lead time between entry and orbiter periapsis = 26.7 minutes. For specific system parameters of 60 watts of probe transmitter RF power, 50 bps data rate, and probability of error = 10^{-3} with binary FSK modulation, the link calculations indicated that the margin will be positive from 20 minutes prior to entry until approximately 30 minutes after entry with peak link margins greater than 4 dB.

The approach developed in this study and employed in determining these parameters and relationships can be applied to other sets of mission constraints and parameter ranges as they are proposed or set during JOP program evolution.

1.2 SYSTEM CONCEPTUAL DESIGN

In Section 3, a design concept is presented for a preentry communication package separate from, but attached to, the probe. In addition to communication, this concept allows instruments, data handling, and possibly power subsystems to be included. The preentry communication subsystem discussed in Section 3 produces a discrete carrier with data on a subcarrier which facilitates doppler measurement Further, provision is made for transmitting a second carrier allowing dual frequency doppler measurement which will allow more accurate determination of the electron density in the ionosphere. This subsystem and support structure for other subsystems has an estimated mass of 2.9 kg and is jettisoned prior to entry into the atmosphere.

1.3 DOPPLER MEASUREMENT ANALYSIS

It may be possible to derive both trajectory and ionosphere content information from a measurement of the doppler shift. Since current concepts for the Jupiter probe do not include a transponder, the measurement must be made from a one-way transmission from the probe to the orbiter. The four basic sources of error in making this measurement are: 1) uncertainty in the probe transmitter frequency, 2) receiver tracking error, 3) scintillation induced error, and 4) received frequency measurement error.

Probe transmitted frequency uncertainty is likely to be the largest single error source. By proper warmup procedures, a probe transmitted frequency accuracy ($\Delta f/f$) of 2×10^{-9} (1.2 Hz at 600 MHz) could be achieved. Receiver tracking error for the assumed maximum doppler rates and worst case signal-to-noise ratio (SNR) is of the order of 1 to 2 Hz, for measurement periods of 0.1 second. The scintillation error contribution, primarily through the introduction of an additive pseudo-doppler, introduces additional error depending on the amplitude and bandwidth of the scintillation encountered. The combined receiver tracking and scintillation induced error, for a 0.10 Hz scintillation bandwidth is estimated at 2.3 Hz based on present

scintillation amplitude estimates at entry. Onboard measurement of the receiver frequency estimate introduces only negligible additional error.

1.4 ELECTRONICALLY DESPUN ANTENNA

Communication performance and/or capacity in the probe-to-orbiter link can be enhanced relative to that achievable with an axisymmetric antenna on a spinning orbiter by using an electronically despun antenna (EDA). This spinning antenna electronically phases the component elements such that the field pattern is focused into a receiving beam pointed toward the probe. In conjunction with this study, a methodology and computational capability was developed for generating conceptual EDA designs and optimizing them with respect to given constraints and requirements. Thus, although the design, briefly summarized below, operates at 400 MHz and is configured for a particular spinning spacecraft, the approach to EDA design developed for this task can be readily applied to a different set of conditions and constraints to develop an optimum design.

For this task, the EDA was to be designed for the Ames Research Center, Pioneer Jupiter Orbiter baseline spacecraft concept of the fall of 1975. Specific requirements were: 1) an operating frequency of 400 MHz, 2) a minimum beamwidth of 50°, and 3) a minimum gain over the beamwidth of 7 dB. General design goals were to minimize the impact on the orbiter, minimize mass, and provide high reliability.

The EDA configuration selected consists of 12 quadrifilar helical elements evenly spaced angularly around a 137 cm diameter mounting ring. The desired field pattern is achieved by activating and properly phasing five of these elements at a time, turning each element on and off once per orbiter revolution. The estimated mass for the entire EDA including electronics is 7.49 kg. Field pattern analysis indicates that a peak gain of 13 dB is possible and that a gain greater than 10 dB for the majority of the probe mission can be accomplished.

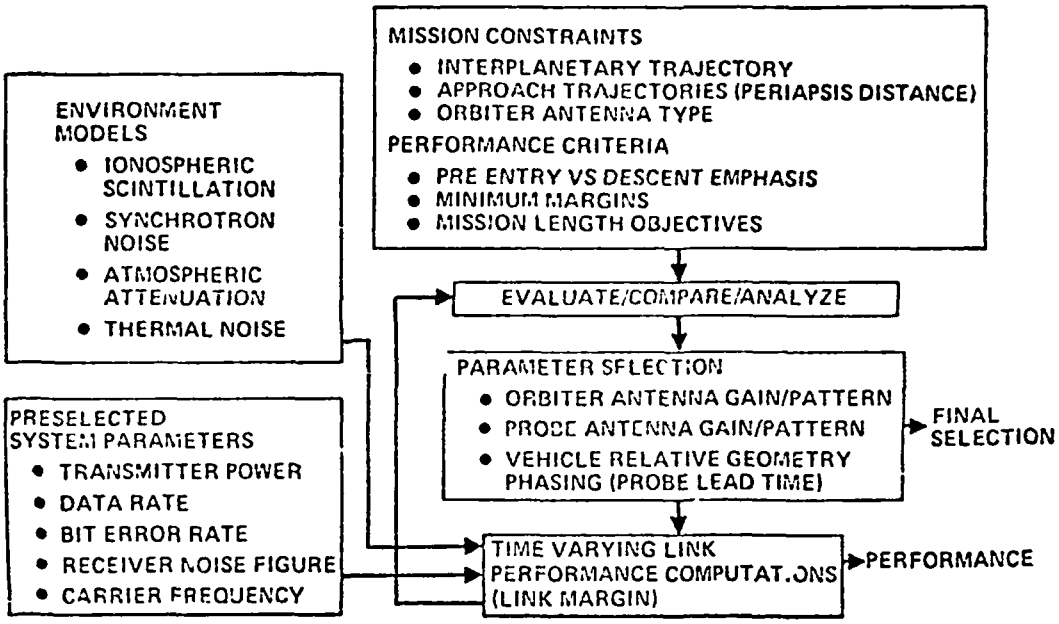
2. LINK ANALYSIS AND DESIGN

The objective of the link analysis was to determine the effect of each significant factor contributing to link performance. In order to achieve this, a procedure and computational capability was employed to determine link performance as a function of time. This procedure can be described by referring to Table 2-1. Mission constraints for this study included 1) an interplanetary trajectory, 2) approach trajectory inclinations, and 3) an axisymmetric antenna on a spinning spacecraft For the simple basic antenna patterns employed in this study, the time variation of link margin was dependent on: 1) the 3 dB beamwidths of the probe and orbiter antennas, 2) the aspect angle between the orbiter's beam center and spin axis, and 3) the probe lead time (defined as the period between probe entry into the Jupiter atmosphere and the orbiter periapsis) Other system parameters, which do not result in a time varying effect on the link, include the transmitter power, data rate, required bit error rate, receiver noise figure, and carrier frequency.

The selected carrier frequency is a factor in all of the environmental models listed in Table 2-1, and its impact on the communication link can be determined nearly independent of the time varying geometry. Thus, initial study efforts were directed to determining the effect of the carrier frequency selection on link performance. Environmental effects influence the frequency selection; thus, data concerning ionospheric scintillation and synchrotron radiation noise, which became available at the beginning of this study, were used together with available information on atmospheric attenuation, Jupiter thermal radiation, and the relationship between frequency and spacecraft receiver noise figures to determine the relationship between frequency and link performance. This resulted in the selection of 600 MHz as a preferred frequency under the mission constraint of an axisymmetric, nonsteerable antenna on a spinning orbiter.

Other mission constraints which were given by NASA, ARC included a nominal interplanetary trajectory and a nominal orbiter periapsis distance of 1.8 R_J. For these parameters, the link will allow preentry data transmission for at least 20 minutes and postentry data transmission for approximately 30 minutes. In addition, the effect of the periapsis distance was investigated with the conclusion that smaller distances result in a larger peak link capacity but a shorter allowable postentry transmission period, while larger distances reduce the peak capacity of the link but allow a longer period

TABLE 2-1 LINK ANALYSIS AND PARAMETER SELECTION



for postentry data transmission. The numerical results supporting these conclusions are presented later in this section.

The performance criteria for selecting system parameters were somewhat arbitrary: they are as follows: 1) peak link margin for both pre- and postentry should be nearly equal and greater than 3 dB, 2) margin immediately following entry should be greater than 1.0 dB, and 3) the period of positive postentry link margin should be maximized. These criteria allowed a selection of a nominal set of optimum parameters which gave comparatively better performance. These selected parameters are as follows: 1) orbiter antenna beamwidth = 50°, 2) orbiter squint angle = 45°, 3) probe antenna beamwidth = 70°, and 4) probe lead time = 26.7 minutes.

As mentioned earlier in Section 1, due to program evolution, the mission constraints such as interplanetary trajectory, approach trajectories of the orbiter and probe, and orbiter antenna limitations are subject to change. In addition, new models of the communication environment, especially ionospheric scintillation and synchrotron radiation noise, may be developed or assumed, and the performance criteria may be more specific and/or different from that mentioned above. Thus, as new requirements, parameters, and data become available, the time varying link calculation approach can be used to optimize system parameters. Many of the general effects of and relationships between parameters presented here will aid in further studies.

2.1 ENVIRONMENTAL FACTORS

2.1.1 Atmospheric Attenuation

Although the emphasis of this study is on preentry, i.e., that period of the probe trajectory just prior (20 to 30 minutes) to encountering the atmosphere, the descent through the atmosphere must be considered. In selecting trajectory and antenna parameters, both the preentry and descent phases must be studied together in order that the selected trajectories and communication system accommodate both phases.

Attenuation of the radio signal in Jupiter's atmosphere for the frequency range of interest (400 to 2400 MHz) is due primarily to absorption by ammonia and water vapor. Defocusing causes a small additional loss. The majority of absorption loss is due to ammonia; however, estimates of its abundance in Jupiter's atmosphere vary greatly. From Reference 2-1, estimates of ammonia mass for the cool and nominal atmosphere models are 0.22 and 0.11 percent respectively, a factor of two difference. Also in Reference 2-1 are temperature versus pressure profiles for cool, nominal, and warm atmosphere models. Recent data from Pioneer 11 indicates that the atmosphere corresponds to a model near the nominal but between nominal and warm.

Atmospheric attenuation has been analyzed in depth by Martin Marietta Corporation and discussed in References 2-2 and 2-3. As an

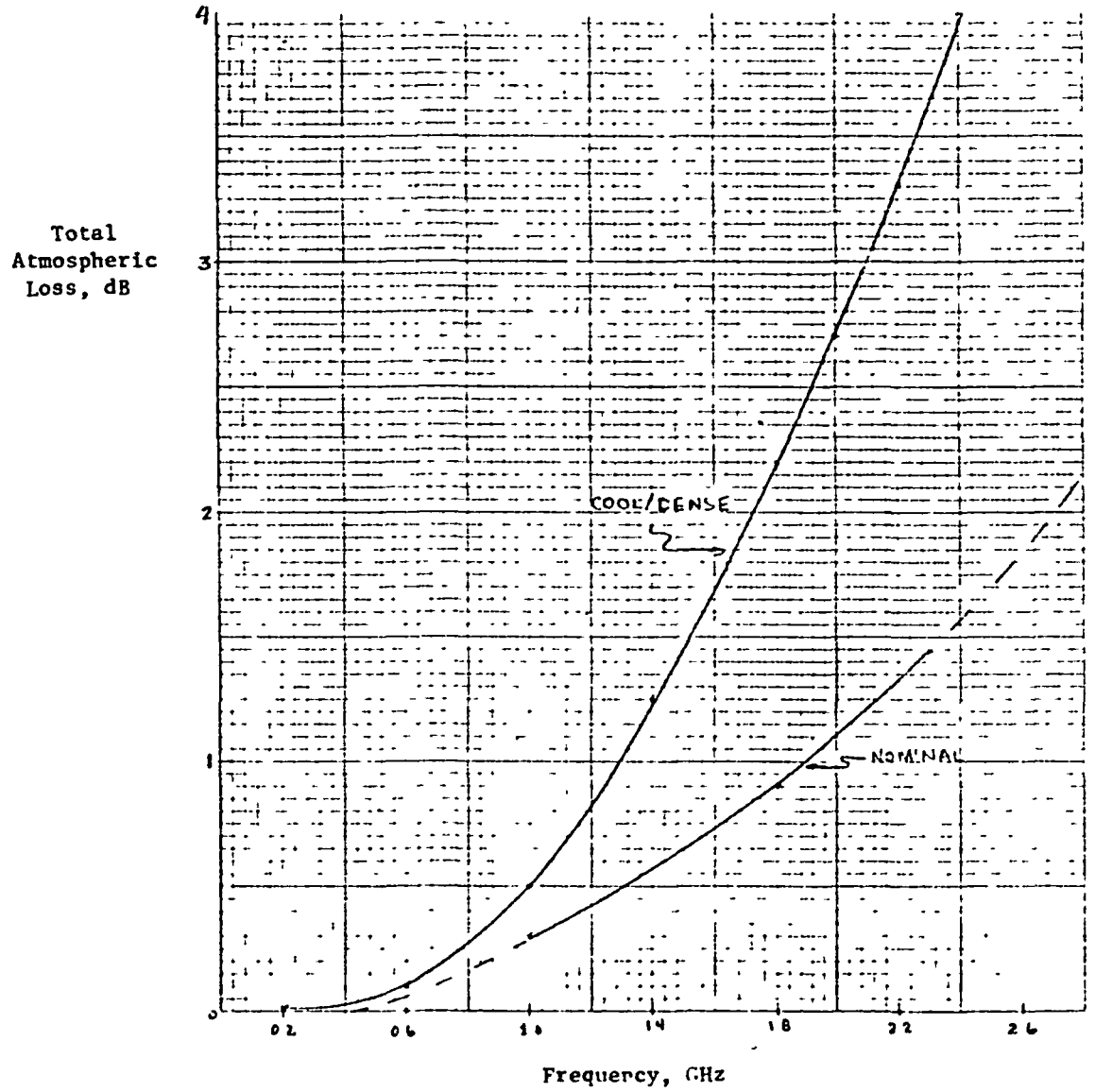


FIGURE 2-1 JUPITER–ATMOSPHERIC LOSS FOR A 10 BAR PRESSURE LEVEL

example, the results of those references were used to produce Figure 2-1. For this study, the nominal model was assumed. The corresponding estimated descent profile together with the attenuation estimates in References 2-2 and 2-3 yield the following formula for attenuation, A:

$$A = [(0.49)f_{GHz} + (0.722)f^2_{GHz}] (0.02725P + 0.00022P^2)/\cos\theta_p \quad (2-1)$$

where

$$P = 0.1962t + 0.0268t^2$$

θ_p = probe aspect angle

and t is time from entry in minutes

2.1.2 Ionospheric Scintillation

Signal fading due to transmission through the ionosphere of Jupiter is, for this study, based on the work of Richard Woo in References 2-4 and 2-5. His estimates are derived from: 1) a theoretical analysis of the fading and 2) processing of the radio signal from Pioneer 10 corresponding to a few minutes before and after occultation by Jupiter. More recent data from Pioneer 11 has led to similar numerical results. The theoretical analysis begins with the assumption that the signal amplitude has a log-normal probability distribution, i.e., that the logarithm of the normalized amplitude (log-amplitude) is normally distributed. The theoretical expression for the frequency spectrum of the log-amplitude, based on diffraction of the signal, is compared with that determined by processing the recorded radio signals. Parameters in the theoretical expression are thus determined, resulting in an analytical expression for the frequency spectrum. The same analysis for a probe transmitting through the ionosphere from below it yields a similar expression with two common parameters. The variance of the log-amplitude for each of these cases is related to the power spectra and the expressions for the variance in each case have a common parameter called the structure constant which is related to the amplitude fluctuations. For probe transmission through the ionosphere, the variance is given by

$$\sigma_x^2 = 0.308\, C_n^2\, K^{7/6}\, L^{11/6} \quad (2-2)$$

where C_n is the structure constant determined from radio measurements as described above, L is the distance from the probe to the outer extent of the portion of the ionosphere with scintillation producing irregularities, and K is the free space wave number = $2\pi f/c$ where f is the carrier frequency and c is the speed of light.

It is shown in Reference 2-- that C_n is proportional to f^{-2} thus

$$\sigma_x^2 \propto (f^{-4})(f^{7/6}) = f^{-17/6}$$

and also it is shown that for $f = 2292$ MHz, C_n lies between 3.3×10^{-8} and 5×10^{-8} $km^{-1/3}$. Woo has used the maximum of this range in his estimates. There is evidence to indicate that the thickness of the ionosphere with irregularities is conservatively estimated at 3000 km.

Using these values, the standard deviation (rms value) of the log-amplitude is given by

$$\sigma_x = 1323.3 \, f_{MHz}^{-17/12} \left(\frac{L_{km}}{3000}\right)^{11.12} \tag{2-3}$$

where L_{km} is the transmission path distance in km determined from the probe altitude and aspect angle to the orbiter. This is the rms value of the natural logarithm of the normalized amplitude, A Thus, $20 \log_{10} A$ represents the fluctuation in decibels, and so

$$\Gamma_{rms} = 20 (\log_{10} e) \sigma_x = 8.686 \, \sigma_x \tag{2-4}$$

is the rms fluctuation in decibels.

This rms value represents fades below the average value as well as signal enhancement above the average value, however, it is the problem of fading that is of concern here. Thus, F of Equation 2-4 will be called the rms fade depth. In this study, an allowance or margin was added to the link requirements large enough to ensure that the probability of a fade greater than this amount is less than 1 percent. For the assumed log-normal fading of Reference 2-4, this fade margin, F is given by

$$F = 2.327 \, F_{rms} \tag{2-5}$$

and hence combining Equations 2-3, 2-4, and 2-5:

$$\text{Fade margin} = \Gamma = (26747) \, f_{MHz}^{-17/12} \left(\frac{L_{km}}{3000}\right)^{11/12} \tag{2-6}$$

where f_{MHz} is the carrier frequency in MHz, and L_{km} is the distance transmitted through the ionosphere in km. Due to limited supporting measurement data, there is a factor of 2 or 3 uncertainty in the estimated fade level, in decibels, given by these formulas.

2.1.3 Noise Temperature

The noise which degrades the communication performance consists of the sum of four major sources: 1) synchrotron radiation noise, 2) planet thermal radiation, 3) cosmic noise, and 4) receiver noise. For this study, the first three, which are environmental effects, were combined with the receiver noise. For the latter, the relationship between noise temperature, T_R, and frequency is shown in Figure 2-2 taken from Reference 2-6. A number of different first-stage devices are shown there, but for this study a straight line approximation was used passing through the intersection of the curves corresponding to a standard bipolar transistor and a standard tunnel diode amplifier (TDA). Because of the log-log scale this line is given by

$$T = 15.36\, f_{MHz}^{0.45} \text{ kelvins} \qquad (2\text{-}7)$$

The effective noise temperature due to synchrotron radiation and planet thermal radiation depends on the spacecraft antenna pattern and its orientation with respect to the planet. The current approach to the antenna pattern is to make it symmetrical about the spin axis of the spacecraft, but to limit its beamwidth in any plane containing the spin axis. An illustration of the general pattern is shown in Figure 2-3. A loop-vee antenna implementation is the current baseline approach to produce this type of pattern.

In Reference 2-7 it is stated that with this type of antenna with beamwidths of 50° or greater, the planet thermal noise is estimated to be 70 K or less. It is shown in Reference 2-1 that the dependence on frequency is small; thus the constant value of 70 K was used in the computations of this study. The contribution of cosmic noise is relatively small and is on the order of the approximations made here. Thus its contribution can be considered to be included in this constant term.

Synchrotron noise is due to radiation by relativistic electrons spiraling around Jupiter's magnetic field lines. Measurements were made by Berge of Jupiter's radiation (Reference 2-8), and these results together with analytical models, are used by Rasmussen, Grant, and Noble in Reference 2-7 to compute the effective noise temperature due to this source. A loop-vee antenna is modeled for their computations and disk brightness temperature is included, although it is a relatively small factor. The original measurements were made at 1.43 and 3 GHz but are converted to any frequency in the UHF range by a simple f^{-2} proportionality factor. Figure 2-4 presents the results of primary interest from Reference 2-7. Due

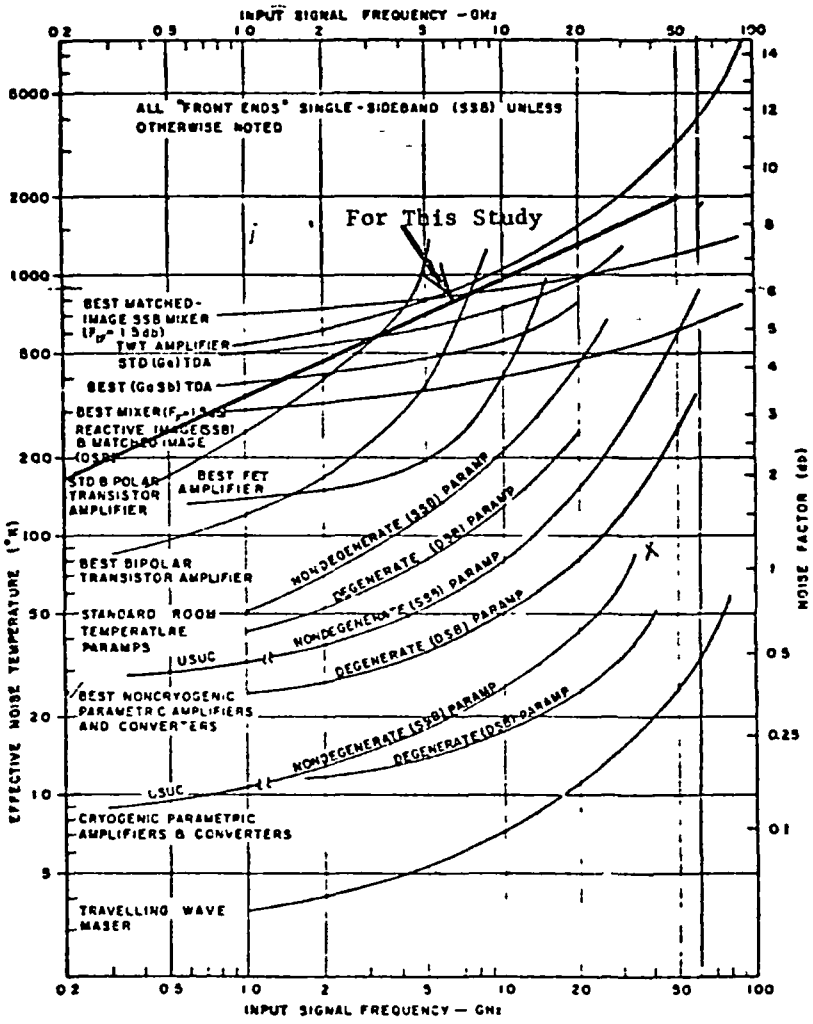


FIGURE 2 2 RECEIVER FRONT END NOISE PERFORMANCE AS FUNCTION OF INPUT SIGNAL FREQUENCY–STATE OF THE ART

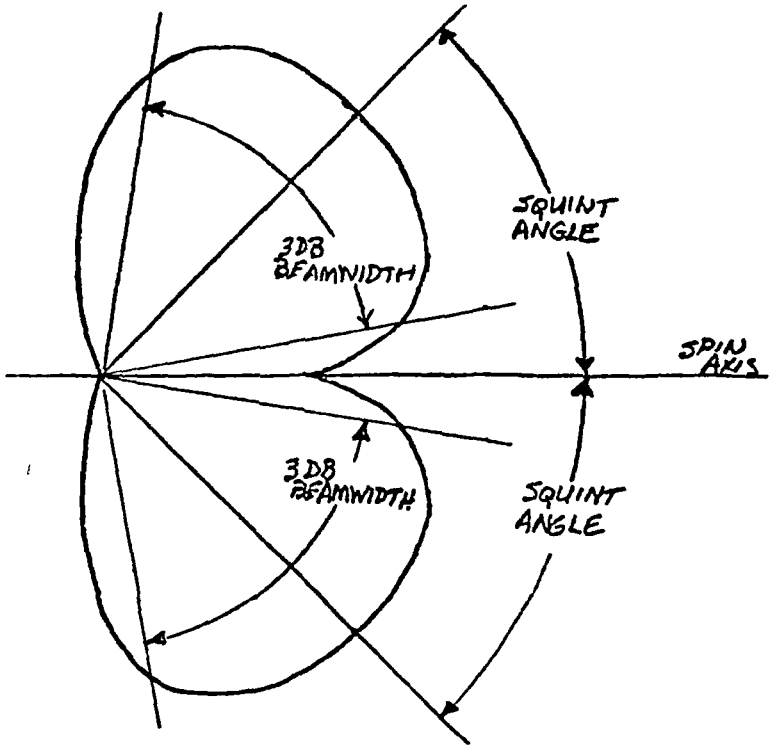


FIGURE 2 3 TYPICAL PATTERN CROSS-SECTION OF AN AXISYMMETRIC SPACECRAFT ANTENNA

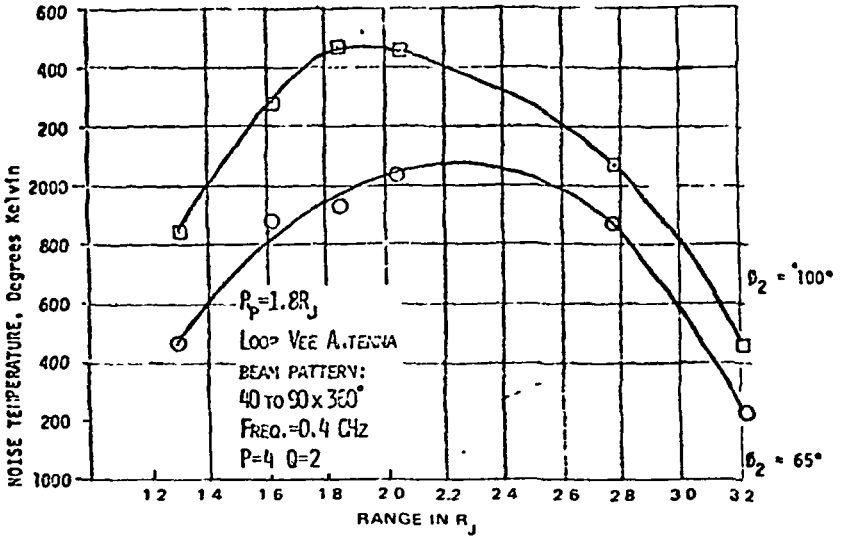


FIGURE 2-4 SYNCHROTRON NOISE TEMPERATURE VERSUS RANGE FROM JUPITER

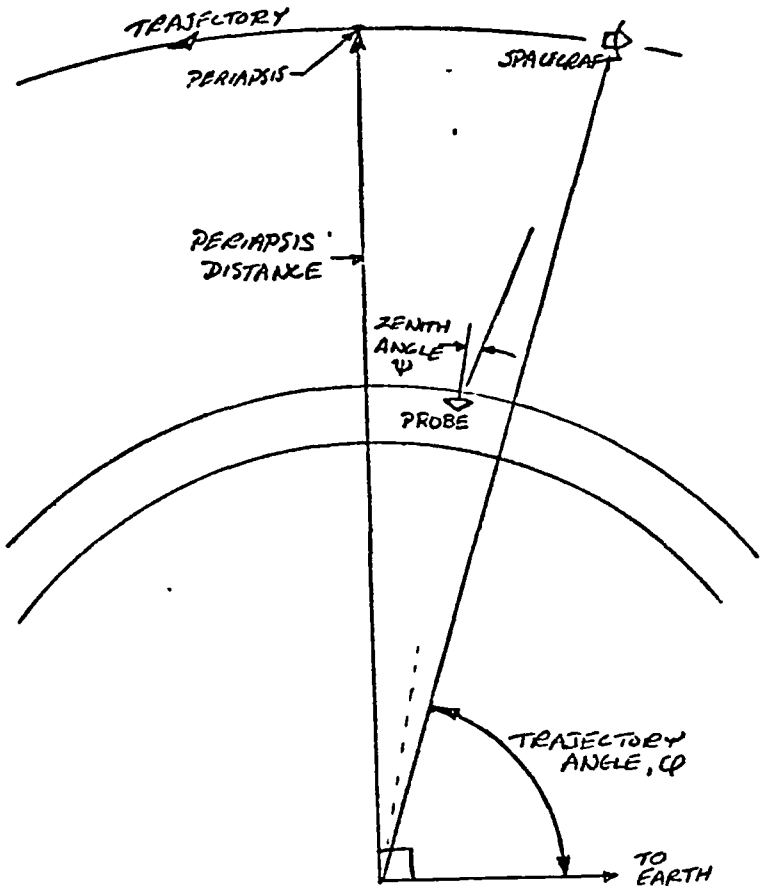


FIGURE 2-5 DEFINITION OF DESCENT GEOMETRICAL PARAMETERS

primarily to uncertainty in the original data, the curves of this figure are approximate and hence contribute another element of uncertainty to the results of this analysis.

The two curves correspond to two positions in a trajectory with respect to the periapsis and hence correspond to the antenna orientation with respect to Jupiter The angle φ is defined in Figure 2-5. Probe entry into the atmosphere corresponds most closely with $\varphi = 65°$ while periapsis occurs near $\varphi = 100°$. As mentioned above, the noise temperature due to thermal radiation contributes approximately 70 K or less to the values of Figure 2-4. Subtracting this amount, the synchrotron noise temperature, T_s, is given approximately by

$$T_s = [2400 - 11.4(90-\varphi)] \left(\frac{400}{f_{MHz}}\right)^2 \qquad (2-8)$$

where the first factor is a linear interpolation between the peak values (~70 K) of Figure 2-4.

Combining all factors discussed, the formula for the system noise temperature, T, is given by

$$T = 70 + 15.36 f_{MHz}^{0.45} + [2400 - 16(90 - \psi)] \left(\frac{400}{f_{MHz}}\right)^2 \text{ kelvins} \qquad (2-9)$$

2.2 TRANSMISSION FREQUENCY

The models for the link factors discussed to this point all have frequency as a parameter. These models as expressed by Equations 2-1, 2-6, and 2-9 have been combined to yield Figure 2-6 for three nominal conditions. These curves do not reflect the effect of space loss which occurs when the antenna gains on each vehicle are fixed Thus, Figure 2-6 represents the predesign situation where the probe has a fixed gain and antenna pattern and the spacecraft is assumed to have the capability to provide a constant effective aperture This could be implemented with an electronically despun antenna on the current Pioneer spacecraft baseline concept. For this case, i.e., constant gain with constant aperture, the combination of spaceloss and spacecraft antenna gain remains constant with frequency, leaving only the effects shown in Figure 2-6 as a function of frequency.

Referring to this figure, the rapid rise at lower frequencies is due to ionospheric scintillation and synchrotron noise while the more gradual rise at higher frequencies is due to atmospheric attenuation. Although a constant aperture antenna would probably result in an increase at higher frequencies in system noise than that indicated in Figure 2-6 due to a greater planet

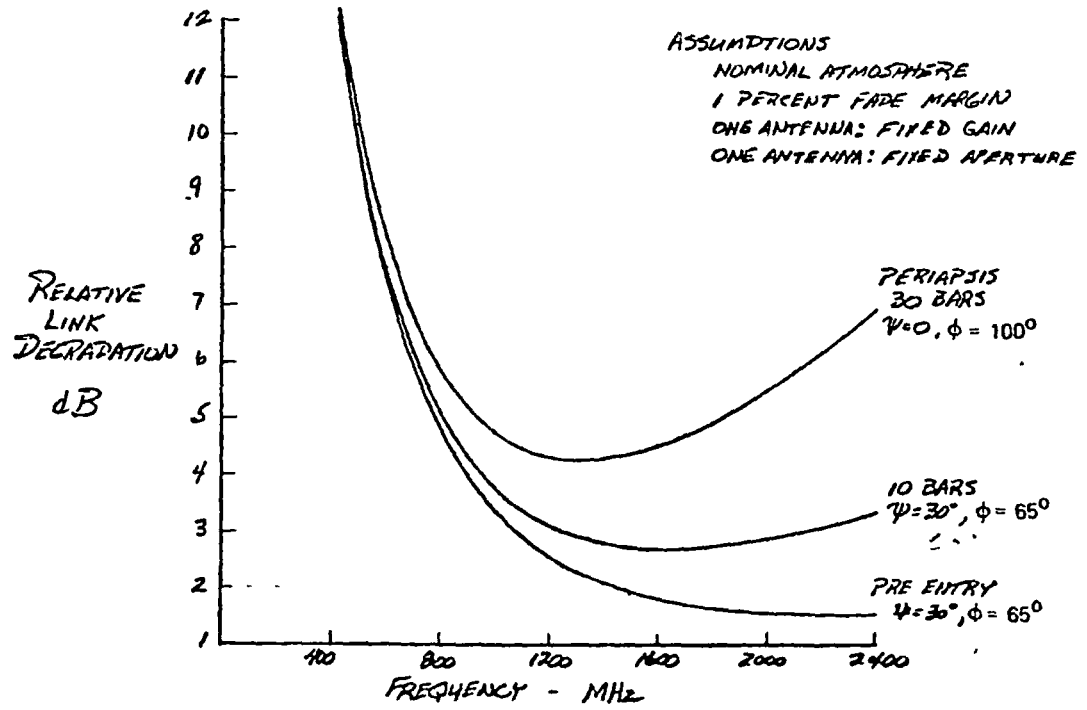


FIGURE 2 6. RELATIVE LINK DEGRADATION, ENVIRONMENTAL AND NOISE FACTORS

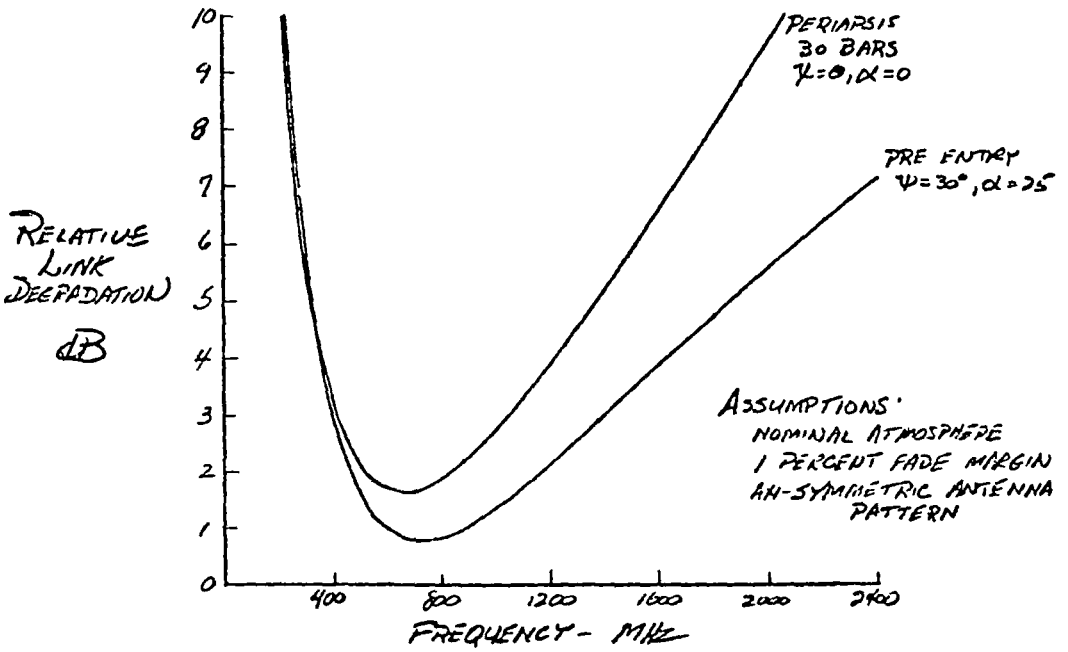


FIGURE 2-7 RELATIVE LINK DEGRADATION FOR FIXED GAIN ANTENNAS

noise contribution, this effect would be relatively small. Thus, if data to 30 bars is emphasized, a frequency in the range 1000 to 1700 MHz should be selected. If data to 10 bars is emphasized, then a frequency in the larger range 1200 to 2400 MHz will be appropriate. These ranges represent approximately 0.5 dB variation in link performance.

2.2.1 Fixed Gain Antennas

A straightforward approach to selecting antenna patterns is to investigate the range of possible trajectories for the spacecraft and probe and then select patterns, fixed relative to each vehicle, which will accommodate a nominal trajectory. The fixed patterns are equivalent to fixed gains and the result is that a "space loss" factor must be added to the link degradations proportional to the square of the frequency. That is, for fixed antenna patterns (gain) on both the spacecraft and probe, the link capacity is inversely proportional to the square of the frequency. Figure 2-7 shows the result. Note that the addition of space loss has caused the curves to rise more rapidly at higher frequencies resulting in sharper minima. For this case, it appears that the transmission frequency should be chosen from the range 550 to 900 MHz.

The current baseline approach to the probe mission is to employ fixed gain antennas. The selection of pattern beamwidths is discussed later. In order to allow use of a higher frequency for doppler measurement twice that of the data carrier (see Section 4), the choice of 600 MHz in the lower end of the above range has been made. From Figure 2-7, this appears to be a near optimum choice for maximizing link capacity to pressure depths of 30 bars if the nominal environmental models employed here are accurate.

2.3 SYSTEM IMPLEMENTATION FACTORS

The objective of the link analysis is to develop the capability to choose a system implementation and to select a preliminary nominal implementation. System implementation refers to the system parameters which determine the link performance during the execution of the probe mission. Specifically these factors are:

1) Transmission frequency

2) Receiver noise temperature

3) Probe transmitter power

4) Spacecraft antenna beamwidth

5) Spacecraft squint angle

6) Probe antenna beamwidth

7) Spacecraft periapsis distance

8) Probe lead time (between entry and spacecraft periapsis)

The first factor has been discussed above and the others are discussed below.

To aid in selecting these system design parameters, a previously developed computer program was modified to compute the link capacity as a function of time. The computation takes into account the time varying geometrical relationship between the spacecraft and probe and then computes the link budget parameters including antenna gains, space loss, system noise temperature, scintillation margin, and atmospheric attenuation.

The latter three environmental factors have been discussed above in subsection 2.1. This section discusses the other factors in the link computations.

2.3.1 Receiver Noise

Subsection 2.1.3 discusses the frequency dependence of receiver noise, and Equation 2-7 represents an approximation used for the parametric trades of this study. For 600 MHz, the temperature given by Equation 2-7 is 273°K. This corresponds to a 3 dB noise figure and represents a good quality receiver at 600 MHz. This value was used in the link computations.

2.3.2 Transmitter Power

The baseline value for probe transmitter power has been taken as 60 watts. The power reflects directly on the link capacity, but, inasmuch as this study emphasized the factors such as trajectory parameters and antenna patterns, whose effects on link performance were less obvious, the baseline value was used in all link computations.

2.3.3 Probe Antenna Pattern

A simple expression was employed, representative of broad beam antennas.

$$\text{Gain} = G(\theta_p) = G_{pkp} \left[\frac{\cos(\beta_p \sin\theta_p)}{\cos\theta_p} \right]^2$$

where

θ_p = probe aspect angle (see Figure 2-8)

G_{pkp} = peak gain = $27000/\psi_p$

ψ_p = half power beamwidth, degrees

$$\beta_p = \frac{\cos^{-1}\left[\cos\left(\psi_p/2\right)/\sqrt{2}\right]}{\sin\left(\psi_p/2\right)}$$

2.3.4 Spacecraft Antenna Pattern

As with the probe antenna.

$$\text{Gain} = G(\theta_o) = G_{pko}\left[\frac{\cos\left(\beta_o \sin\theta_o\right)}{\cos\theta_o}\right]^2$$

where

θ_o = [spacecraft aspect angle - squint angle] (see Figures 2-8 and 2-3)

G_{pko} = peak gain = $\frac{27000}{360\psi_o}$

ψ_o = half power beamwidth, degrees

$$\beta_o = \frac{\cos^{-1}\left[\cos\left(\psi_o/2\right)/\sqrt{2}\right]}{\sin\left(\psi_o/2\right)}$$

The pattern is axially symmetric about the spacecraft spin axis (see Figure 2-3).

2.4 LINK STUDIES AND PERFORMANCE ANALYSIS

In order to study the effect of the many system factors on the probe-to-spacecraft link, transmission distance, antenna gains, system noise temperature, ionospheric scintillation, and atmospheric attenuation were computed as a function of time. The design parameters which can be varied are the probe antenna pattern (beamwidth), the spacecraft antenna beamwidth, and the angle (squint angle) between the spacecraft antenna beamcenter and the spin axis. In addition, the preentry approach trajectories can be chosen as desired.

This study has concentrated on one interplanetary trajectory and two approach trajectories, although the effect of changing periapsis distance is shown. The parameters for these cases are listed in Table 2-2. The spacecraft remains in the equatorial plane but two different probe entry latitudes were investigated. Entering at a 16° latitude (case II) decreases the

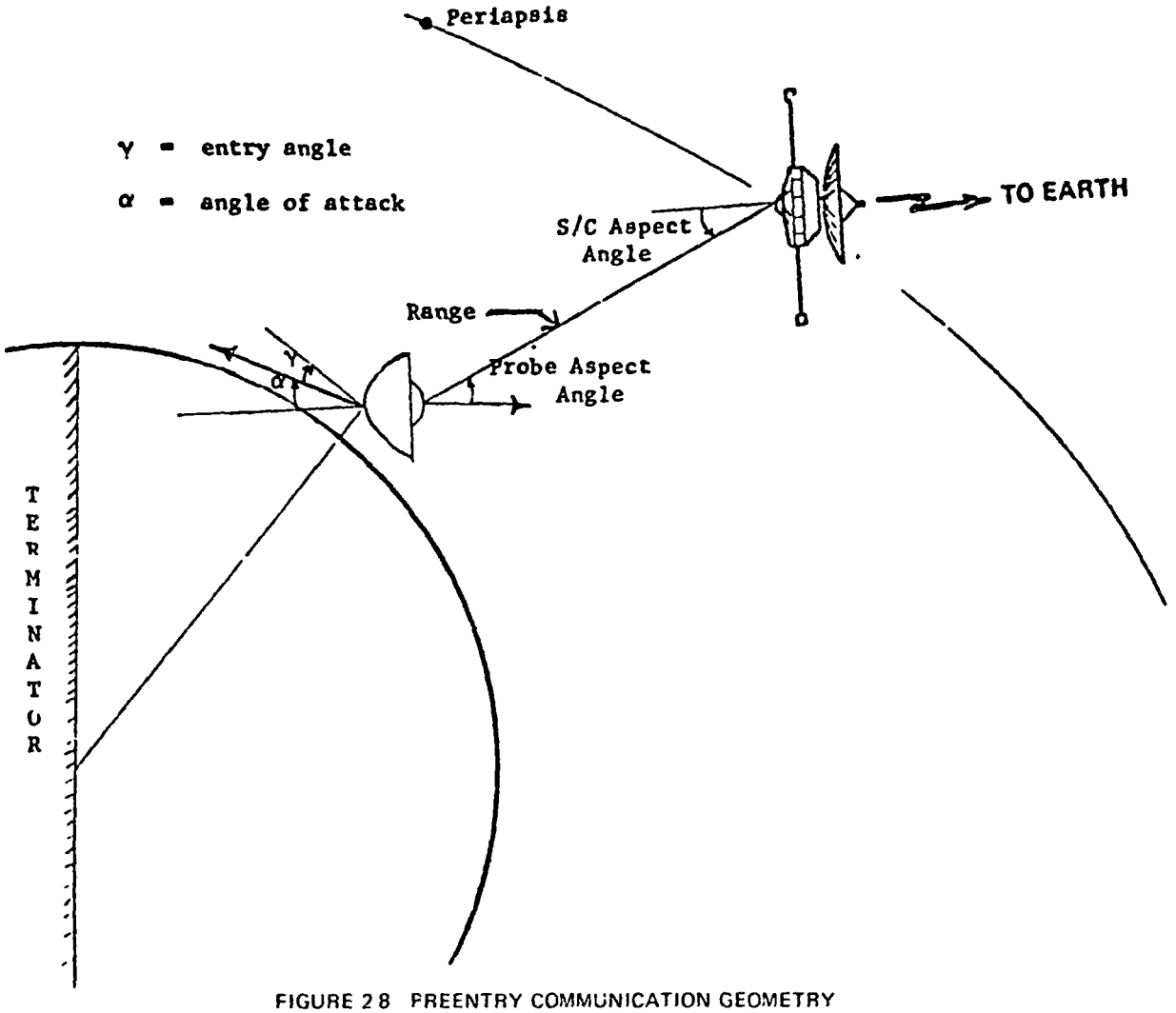


FIGURE 2 8 FREENTRY COMMUNICATION GEOMETRY

radiation dosage experienced by the probe; however, as is shown later, the resulting geometry is unfavorable, reducing communication link capability because the transmission line of sight corresponds to low probe antenna gain.

The measure of link performance for this study is margin, i.e., excess capability based on nominal equipment and demodulation parameters. The nominal parameters used in these calculations are listed in Table 2-3. All other factors affecting link capacity are time varying, depending on the geometrical relationship of the spacecraft and the probe with respect to each other and to the planet Jupiter, its ionosphere, and its atmosphere.

TABLE 2 2 TRAJECTORY PARAMETERS

Launch date	22 December 1981	
Arrival date	24 November 1984 (2446028 8)	
Trip time	1068 days	
C_3	90 15 km^2/sec^2	
v_∞	5 79 km/sec	
Equatorial declination of asymptote	3 5°	
Spacecraft periapsis	1 8 R_j	
Probe parameters		
Entry angle	7 5° at 450 km	
	Case I	Case II
Entry latitude	3°	16°
Entry angle of attack		
No reorientation	8 1°	31 5°
With reorientation	–	10 0°

TABLE 2 3 COMMUNICATION SYSTEM PARAMETERS

1) Probe transmitter power	60 W
2) Line and polarization loss	0 8 dB
3) Transmission frequency	600 MHz
4) Data rate (50 bps)	17 dB
5) Processing loss	1 5 dB
6) $E_b N_0$ for $P_e = 10^{-5}$	10 6 dB*
7) Required power to noise density (4 +5 +6)	29 1 dB Hz

*Assumes noncoherent FSK with convolutional coding

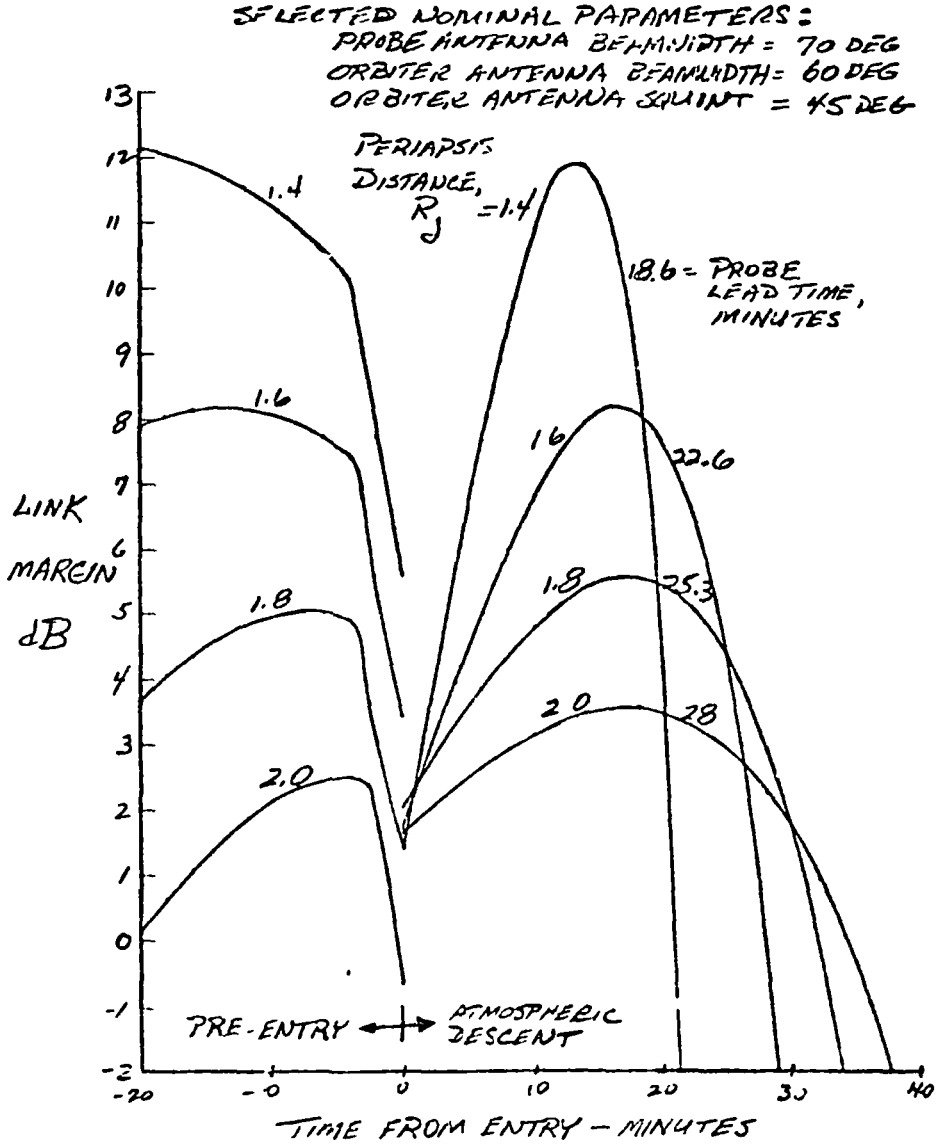


FIGURE 2 9 LINK MARGIN AS A FUNCTION OF PERIAPSIS DISTANCE

2.4.1 Trajectory Parameters

Figure 2-9 shows the link margin as a function of time for four values of periapsis distance. The probe lead time, i.e., time from probe entry to spacecraft periapsis, was chosen in each case so that the margin at the beginning of the atmospheric descent was greater than 1.0 dB but gave the longest time from entry until the margin reached 1.0 dB. The granularity in probe lead time used in the computations did not allow the initial entry margin to be the same for each periapsis distance, but the overall effect differs only slightly for changes of 1 or 2 minutes. In general, smaller probe lead times improve the margin immediately following entry (t = 0+) but result in a shorter descent transmission period and decreased preentry margin.

Referring to Figure 2-9, it can be seen that smaller periapsis distances result in the following:

1) Greater preentry link capacity

2) Greater initial descent link capacity

3) Shorter descent transmission time

For this study, the value of 1.8 R_J was chosen as the nominal value of periapsis distance. It results in sufficient margin during most of preentry and descent and allows transmission for more than 30 minutes of descent.

The probe lead time depends on the squint angle selected for the spacecraft antenna; this will be discussed further below.

2.4.2 Carrier Frequency

This subject has been discussed previously, but the results of actual link calculations have not yet been shown. Figure 2-10 illustrates the effect of carrier frequency. Note that for the primary mission of atmospheric descent, 600 MHz provides the greatest link capacity. During preentry, the margin with 400 MHz peaks slightly higher but drops much more rapidly just prior to entry.

2.4.3 Preentry and Entry

The sharp drop in margin just before entry for all the curves of Figures 2-9 and 2-10 is due primarily to: 1) ionospheric scintillation and 2) increasing distance between the vehicles, with the former having the greater effect. As discussed in subsection 2.1.2, a fading margin has been added to the link as an effective degradation in order to compute link capacity with a probability of 90 percent. The ionosphere has been estimated to be 3000 km in depth (see Reference 2-2), and the probe enters this region approximately 4 minutes prior to entering the atmosphere. Thus, based on the estimated effects of ionospheric scintillation as discussed in subsection 2.1.2, the link capacity decreases significantly and rapidly during this

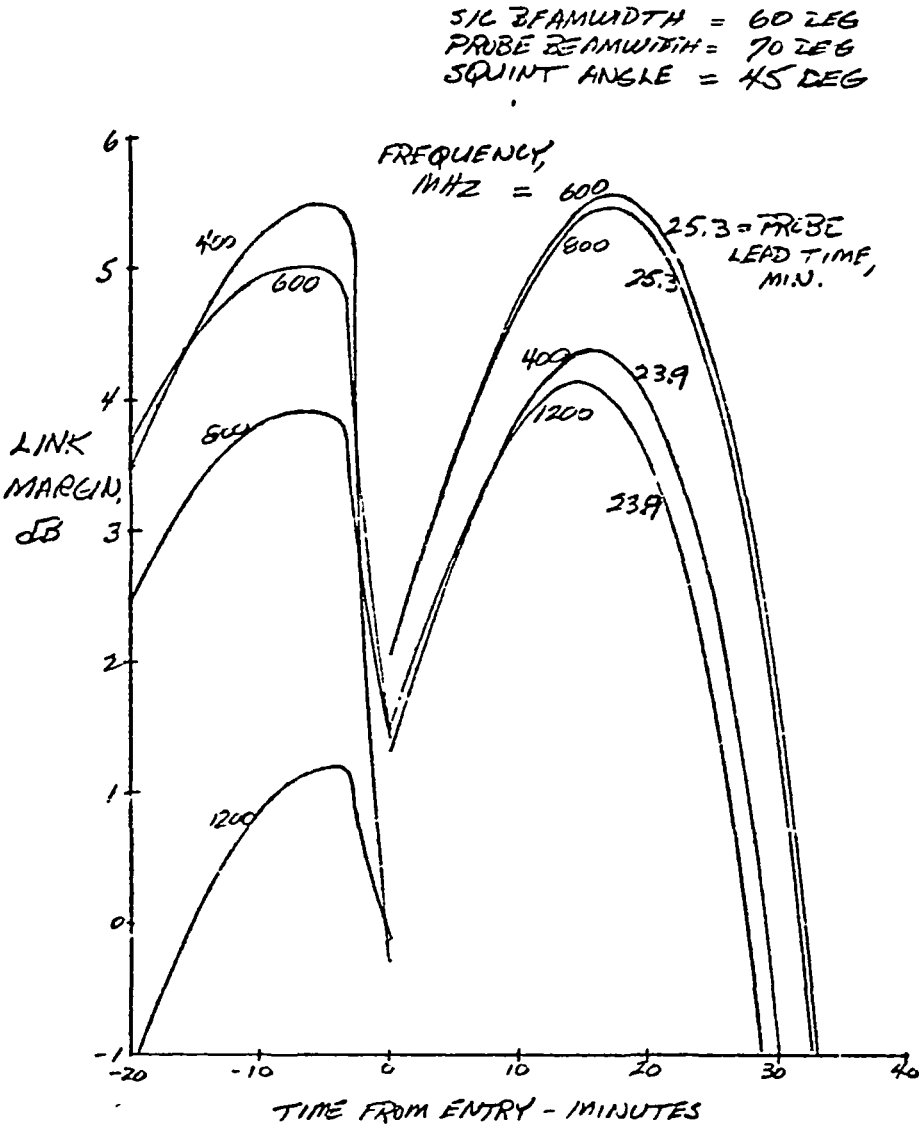


FIGURE 2 10 LINK MARGIN AS A FUNCTION OF FREQUENCY

period. Data transmission quality during this short period prior to entry becomes less certain while, at the same time, it becomes more valuable. The only solution to this dilemma is to use a higher carrier frequency and provide greater gain with the spacecraft antenna. This may require steering of the antenna beam. This alternative was beyond the scope of this study.

Immediately following entry into the atmosphere, the probe slows to less than sonic speeds and its spin axis rotates so as to nominally parallel the local vertical. Although this occurs during a period of about 1 minute, for the purposes of link computations, it was assumed to occur instantaneously at t = 0, resulting in the discontinuities of Figures 2-9 and 2-10. Thus, during the first 2 minutes following entry, the link margin will lie somewhere between the final preentry value at t = 0 and the curves for postentry. However, during this period, communication is precluded by the entry "blackout" phenomenon, thus link margin is academic only, and the simplifying assumption of instantaneous change at entry does not detract from the link calculations.

2.4.4 Probe Lead Time

Computed parameters which aid in understanding variations in performance are the range (distance between the vehicles), spacecraft aspect angle with respect to the spin axis, and the probe aspect angle also with respect to its spin axis. These parameters are defined in Figure 2-8. The relative positions of the two vehicles can be adjusted by a spacecraft ΔV maneuver; Figure 2-11 shows the effect of this phasing on the range for case 1 of Table 2-2. The time of periapsis for the spacecraft is measured from probe entry, and the time between these two events, as mentioned above, is defined as probe lead time. Figures 2-12 and 2-13 show the time variation of the two aspect angles and Figure 2-14 combines all effects to show the link margin above the nominal required signal-to-noise ratio as both a function of time and of the relative phasing for two probe antenna beamwidths. Note that link margin decreases rapidly just before probe entry, reaching a minimum at entry, and then increases for approximately 20 minutes, followed by a final decline as the probe descends deeper and deeper into the Jovian atmosphere.

2.4.5 Spacecraft Antenna Beamwidth

Figure 2-15 shows the effect of different spacecraft antenna beamwidths. The ordinate represents the difference in link margin between 50° and 70° beamwidths and a 60° beamwidth. A 70° beamwidth results in slightly lower margin (link capacity) until late in the probe descent when the spacecraft is near periapsis and almost directly above the probe. A 50° beamwidth has the opposite effect and would penalize communication after approximately 25 minutes of atmospheric descent. Since probe survival time and power source duration are unresolved, the choice between 50° and 60° is not clear. However, for the price of less than 1 dB, the 60° beamwidth will accommodate a longer descent and/or greater error in trajectory phasing. Further study, when mission details are better known, may indicate a preferred beamwidth between 50° and 60°, but for the purposes of preliminary system definition, 60° appears appropriate.

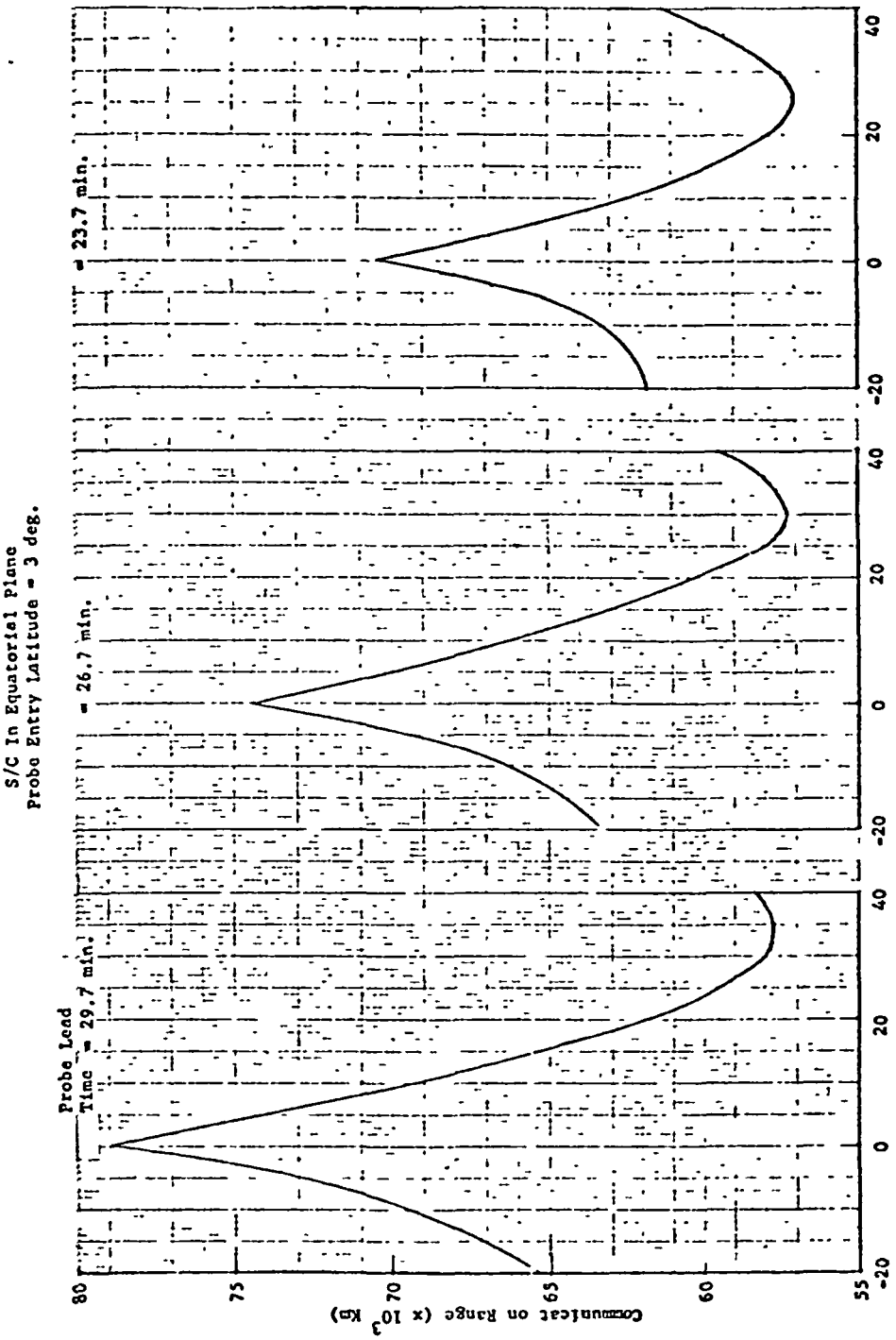


FIGURE 2.11 COMMUNICATION RANGE

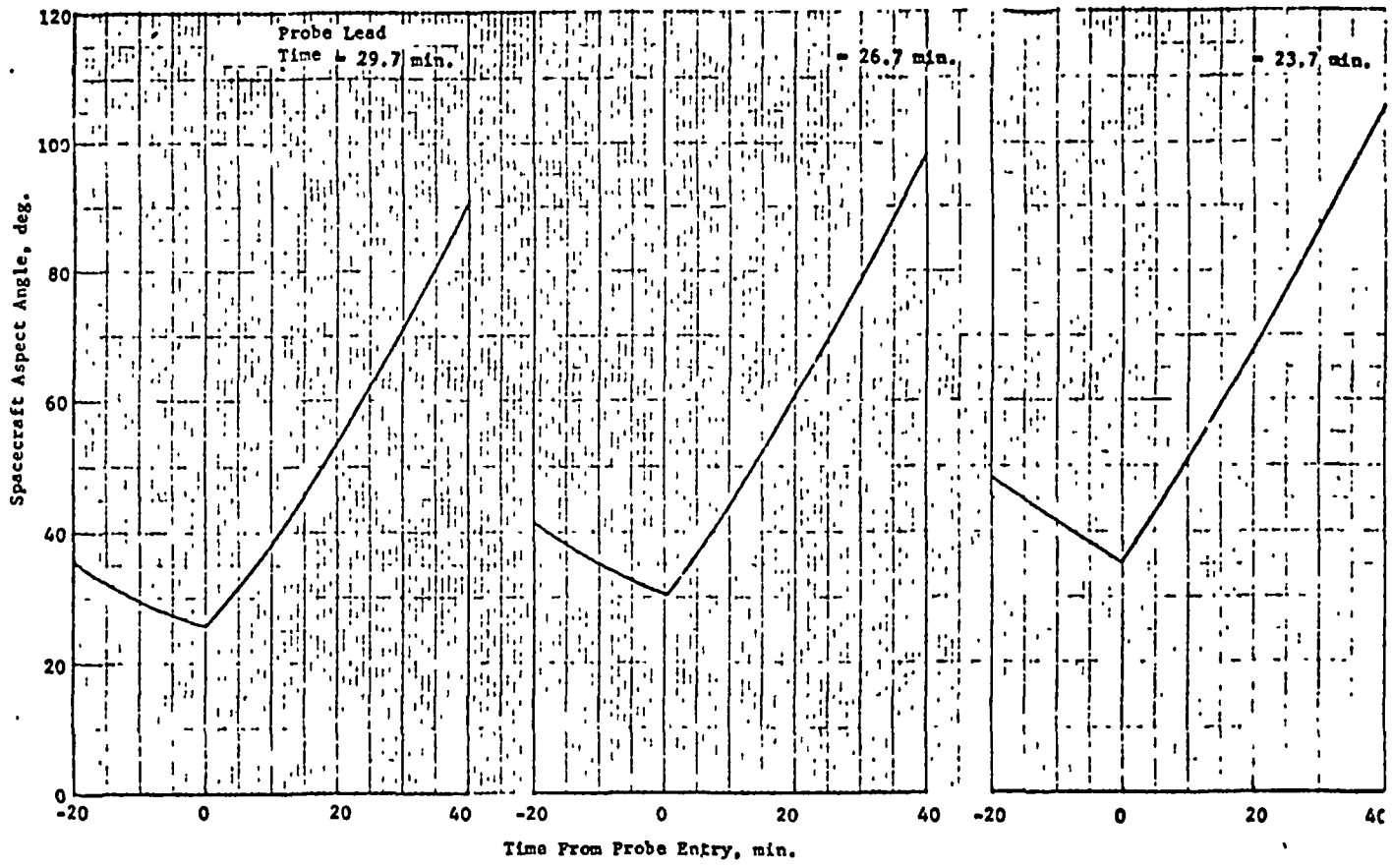


FIGURE 2-12 SPACECRAFT ASPECT ANGLE

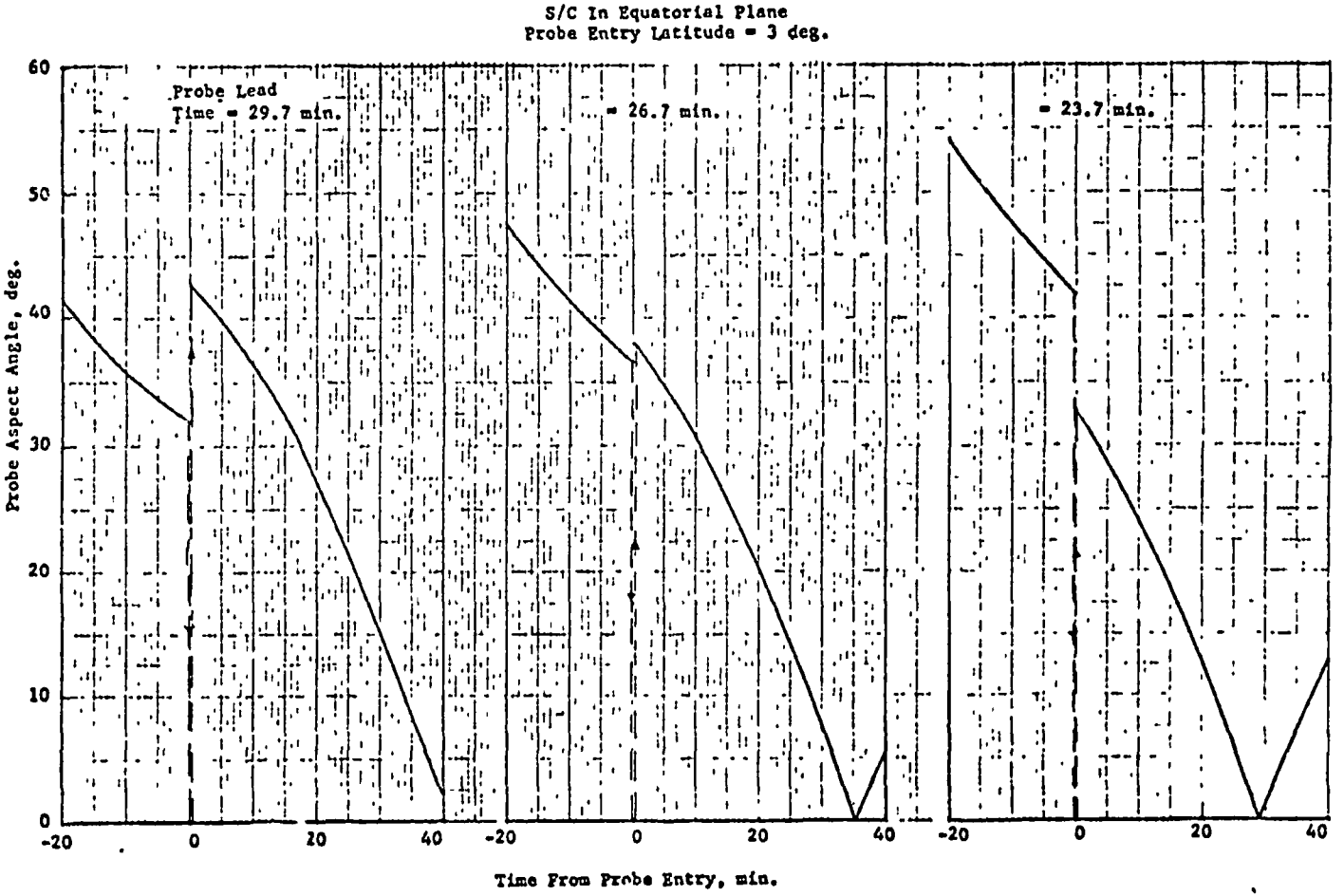


FIGURE 2-13 PROBE ASPECT ANGLE

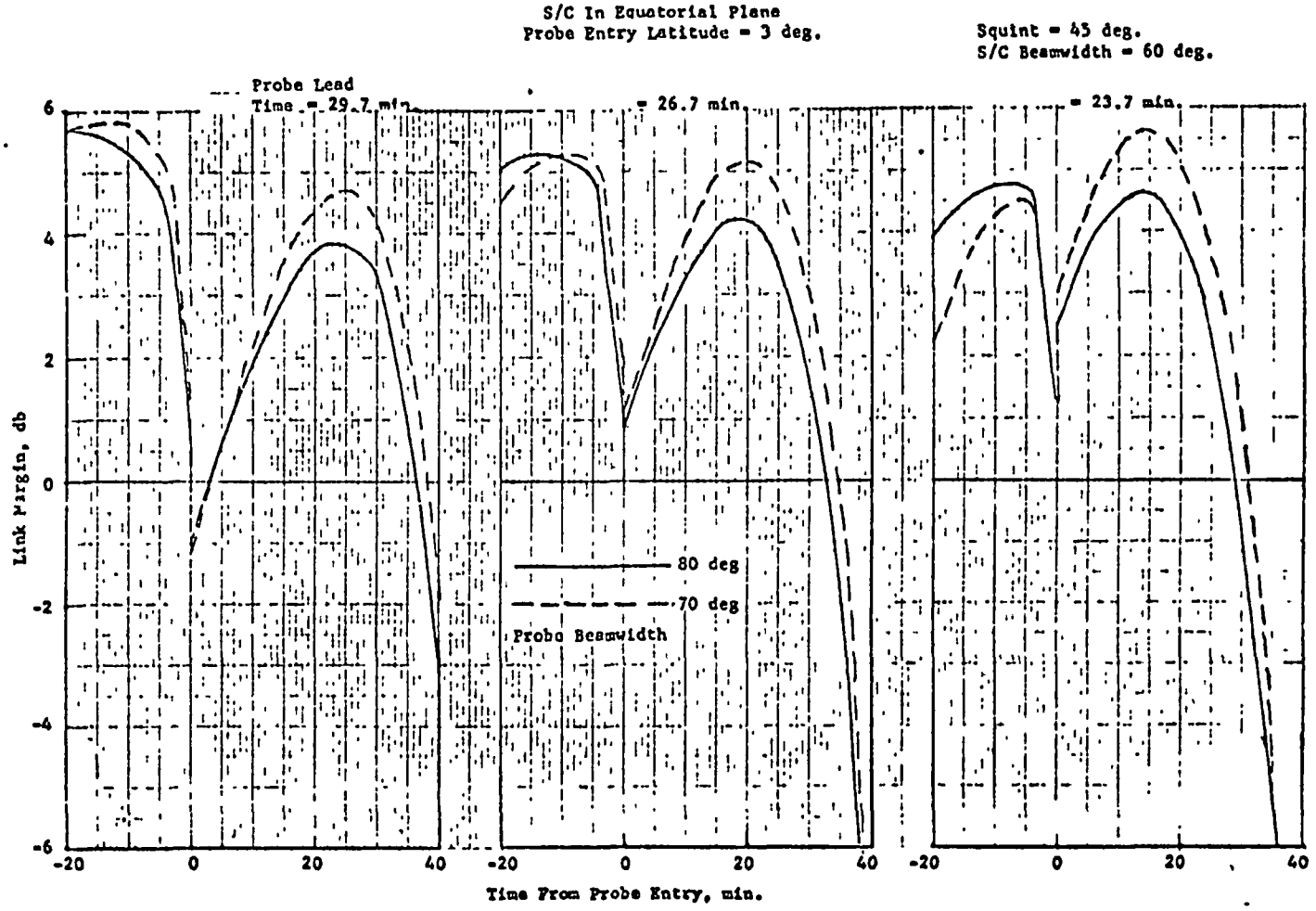


FIGURE 2 14 LINK MARGIN (600 MHz)

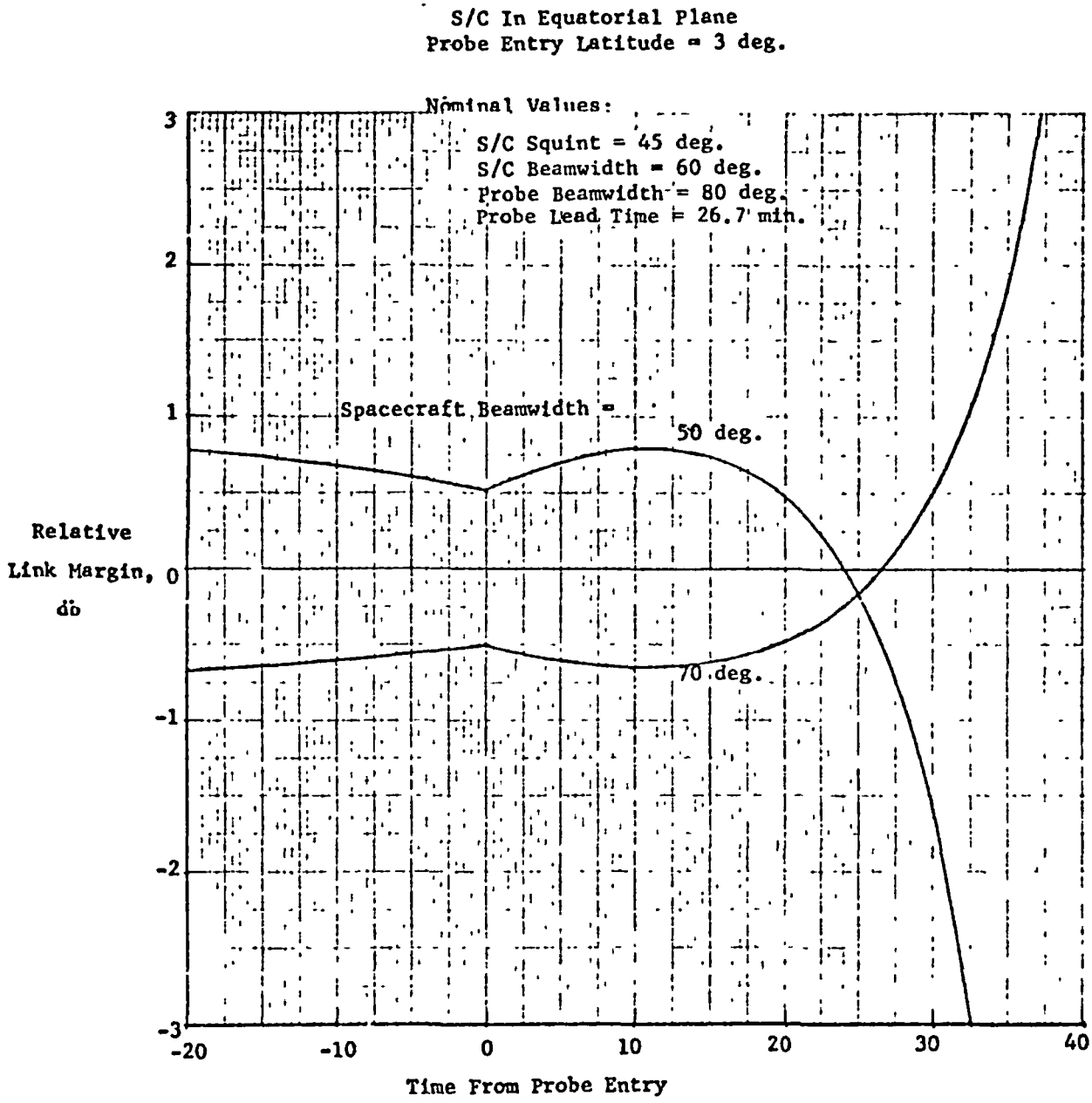


FIGURE 2 15 EFFECT OF SPACECRAFT ANTENNA BEAMWIDTH ON LINK MARGIN

2.4.6 Spacecraft Antenna Squint Angle

Figure 2-16 shows the difference in link margin which occurs between squint angles of 35°, 45°, and 55°. A squint angle of 35° provides a slight advantage to preentry and early descent but penalizes descent beyond approximately 8 minutes. A squint angle of 55° penalizes the communication link until about 10 minutes after entry and improves the link by about 2 dB at 30 minutes. In order to enhance data return from deeper in the atmosphere, the squint angle should lie in the range of 45° to 55°. Figure 2-17 may be compared to Figure 2-9; the only differences being the squint angle and two of the probe lead times. Note that for a 1.8 R_J periapsis distance, the postentry margin is higher and preentry margin is lower for a squint angle of 50° with the probe lead time shown. A larger probe lead time will equalize the peak margins for both pre- and postentry, but, 1) the initial postentry margin will be lower, and 2) the time of positive margin will be longer. Thus, there appears to be a range of squint angles from 45° to 55° and probe lead times from 24 to 27 minutes from which a best combination may be chosen. A nominal choice for a baseline mission corresponds to the center curve of Figure 2-14: squint angle = 45° and probe lead time = 26.7 minutes.

2.4.7 Probe Beamwidth

Figure 2-18 compares three different probe beamwidths. Compared to 80°, a larger beamwidth of 90° results in poorer performance over both preentry and descent periods. However, a smaller beamwidth of 70° improves performance over most of the region of interest. Since energy limits may restrict the beginning of transmission to 10 minutes or less before entry, a beamwidth of 70° may be most appropriate. This can also be seen in Figure 2-14 where the link margin for both a 70° and 80° probe beamwidth is shown. The 70° beamwidth results in better link performance except for the period between 20 and 10 minutes prior to entry as is shown in Figure 2-18.

Another consideration is the timing error; however, from Figure 2-14 it can be seen that for different probe lead times, a probe beamwidth of 70° is as good or better than one of 80° except for a portion of the preentry period.

2.4.8 Higher Latitude Entry

Because of the radiation environment which is most severe at the magnetic equator, it has been proposed that the probe enter at a higher latitude. Case II of Table 2-2 corresponds to an entry latitude of 16°, which without a spacecraft reorientation prior to release results in an entry angle of attack of 31.5°. For aerodynamic reasons, an angle of attack of 10° or less is desired so both cases were considered.

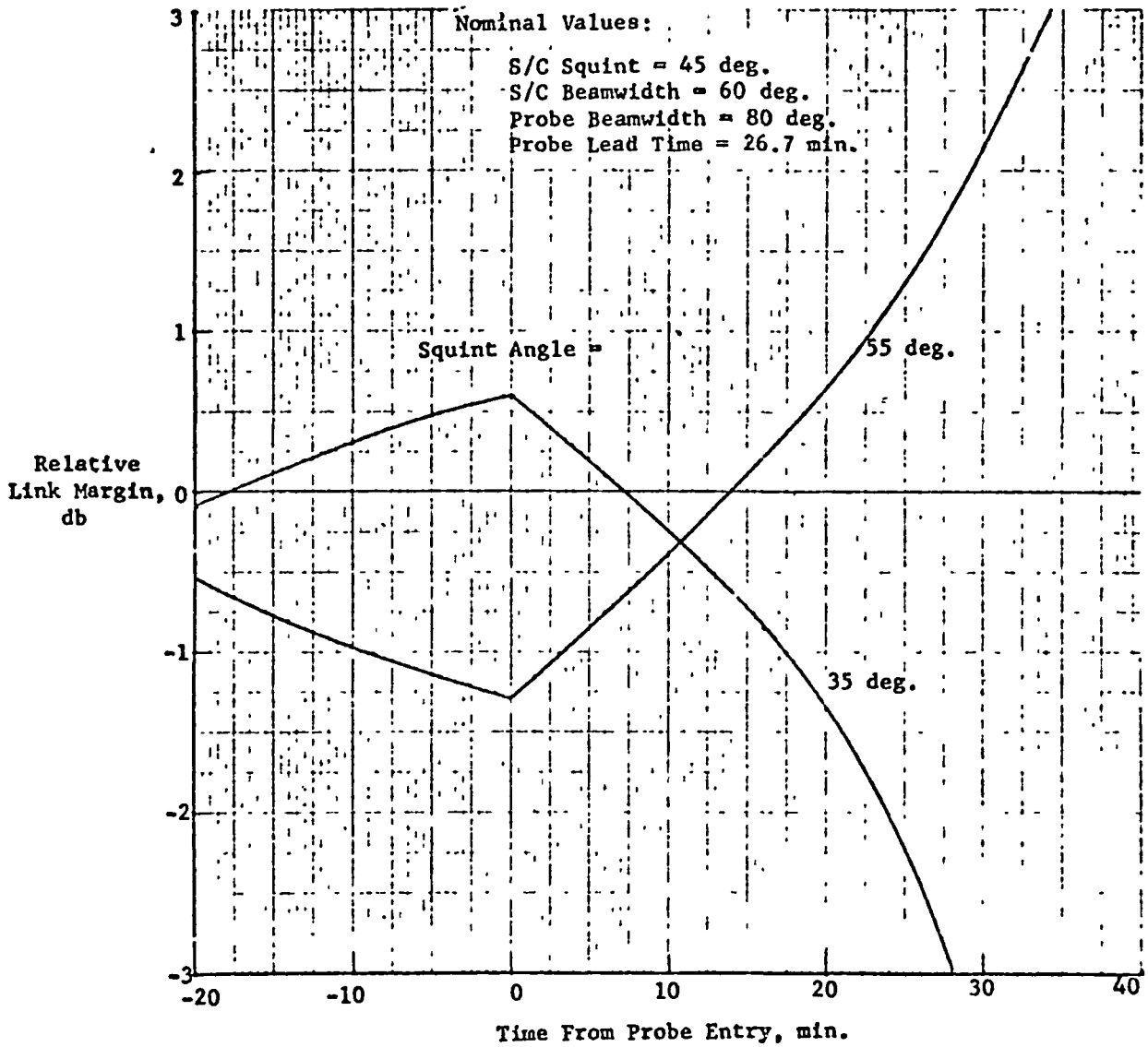


FIGURE 2-16 EFFECT OF SPACECRAFT ANTENNA SQUINT ANGLE ON LINK MARGIN

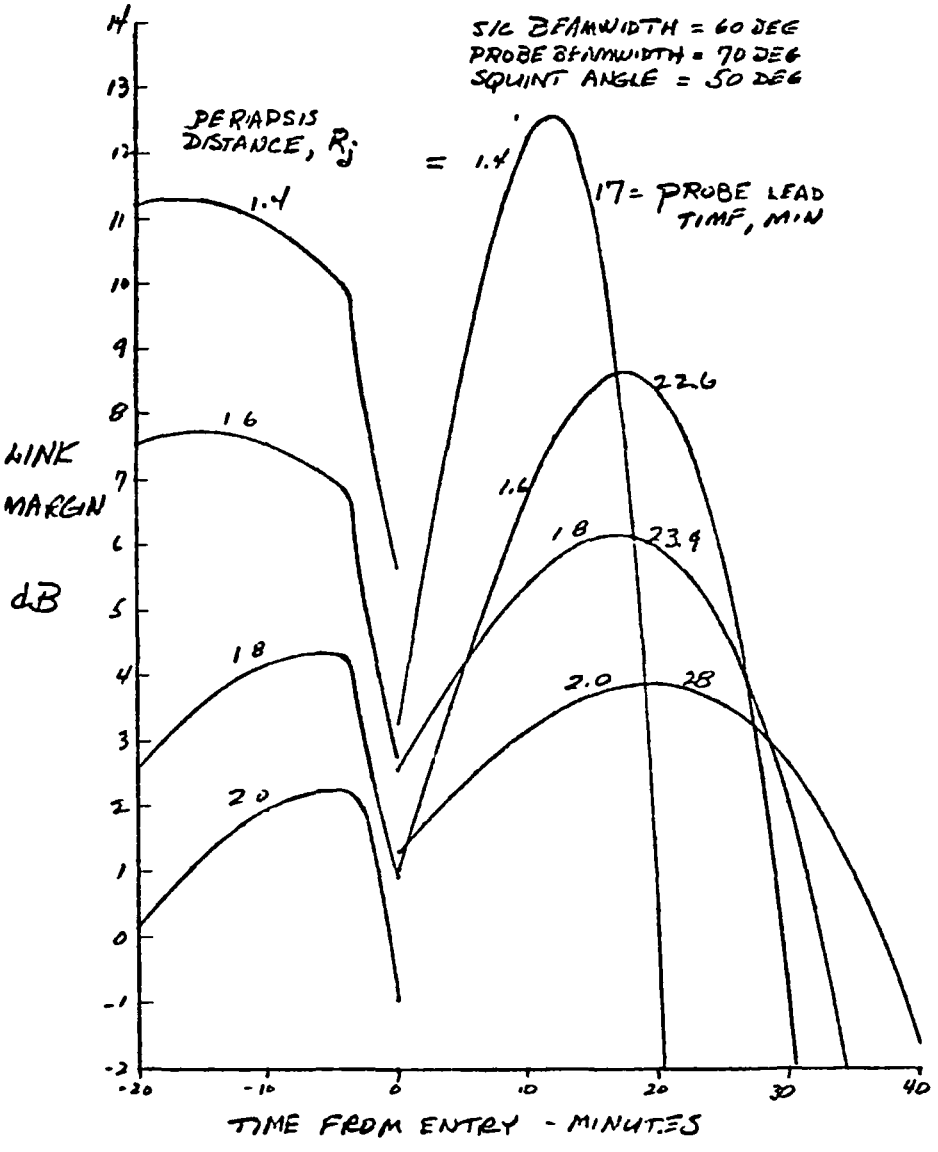


FIGURE 2 17 LINK MARGIN AS A FUNCTION OF PERIAPSIS DISTANCE

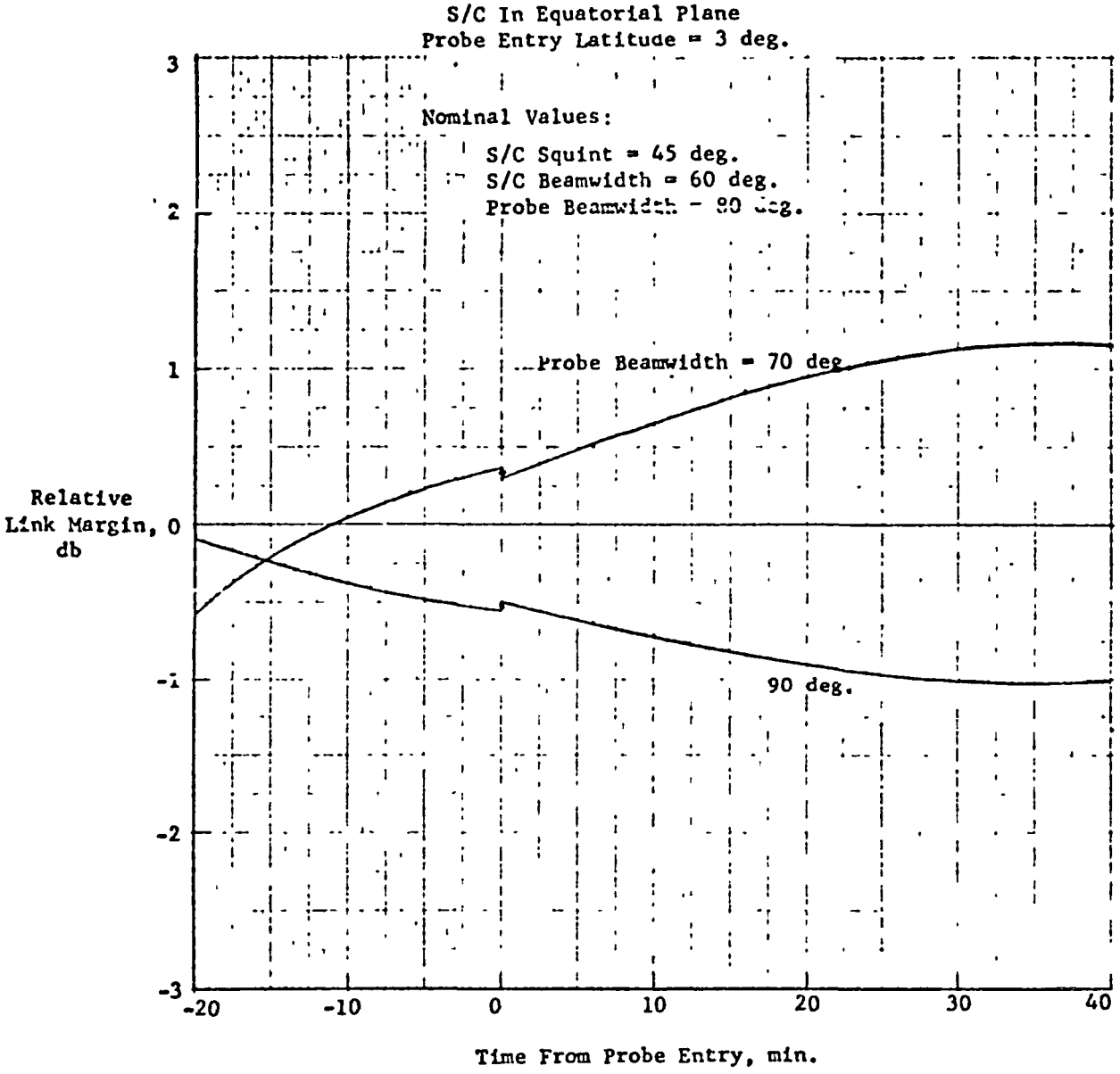


FIGURE 2 18 EFFECT OF PROBE ANTENNA BEAMWIDTH ON LINK MARGIN

The primary difference between a 3° and 16° latitude entry is the much larger probe aspect angle which occurs in the latter case if the spacecraft remains in the equatorial plane. This is illustrated in Figure 2-19. From Figure 2-20, which shows the link margin history for this case, it can be seen that the link performance will be unsatisfactory for the parameters of Table 2-3.

If the spacecraft is placed in the plane of the probe trajectory, then a higher latitude entry may be achieved with acceptable communication performance. The probe aspect angle and link margin histories are shown in Figures 2-21 and 2-22.

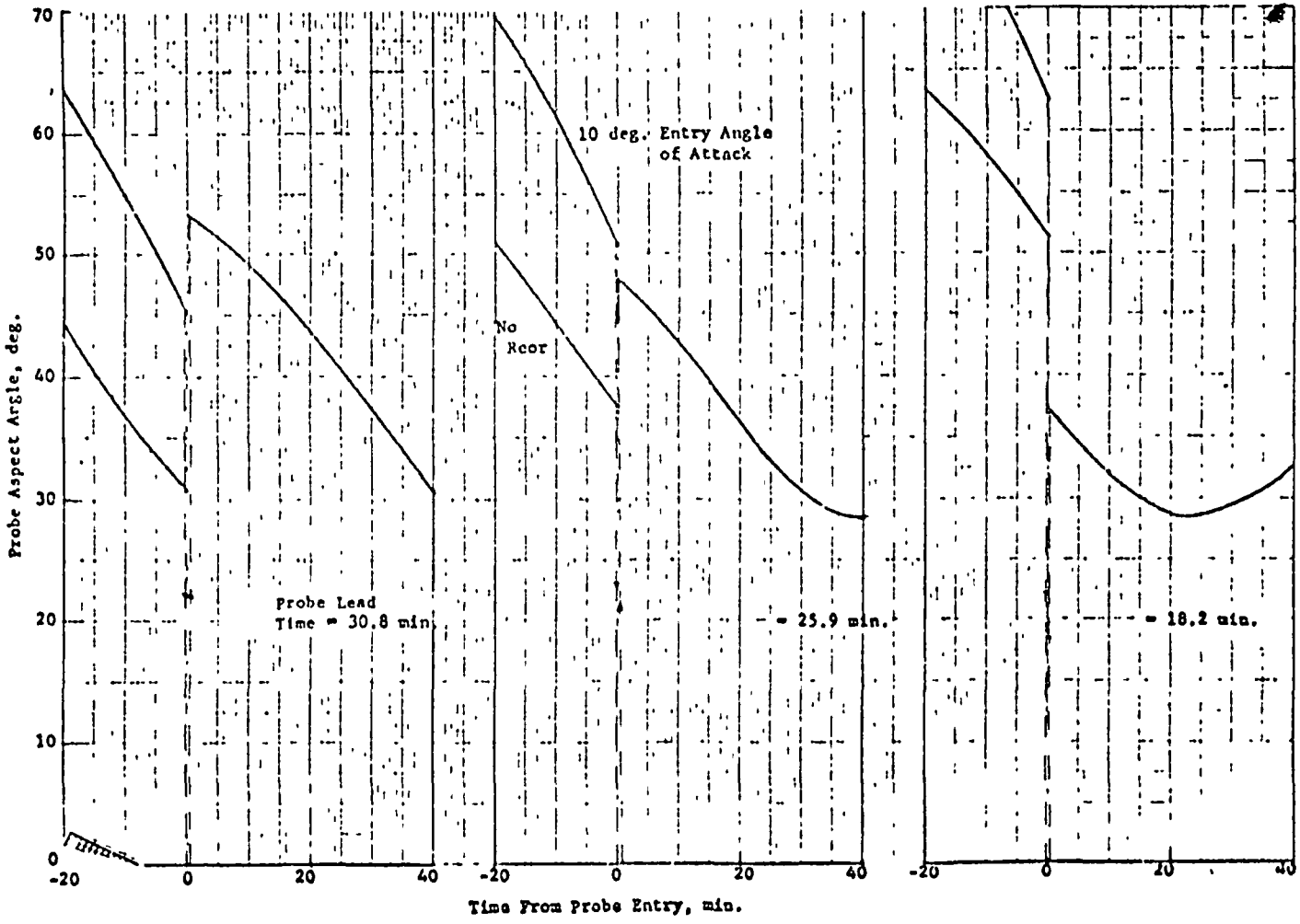


FIGURE 2 19 PROBE ASPECT ANGLE FOR SPACECRAFT IN EQUATORIAL PLANE AND PROBE ENTRY LATITUDE 16 DEGREES

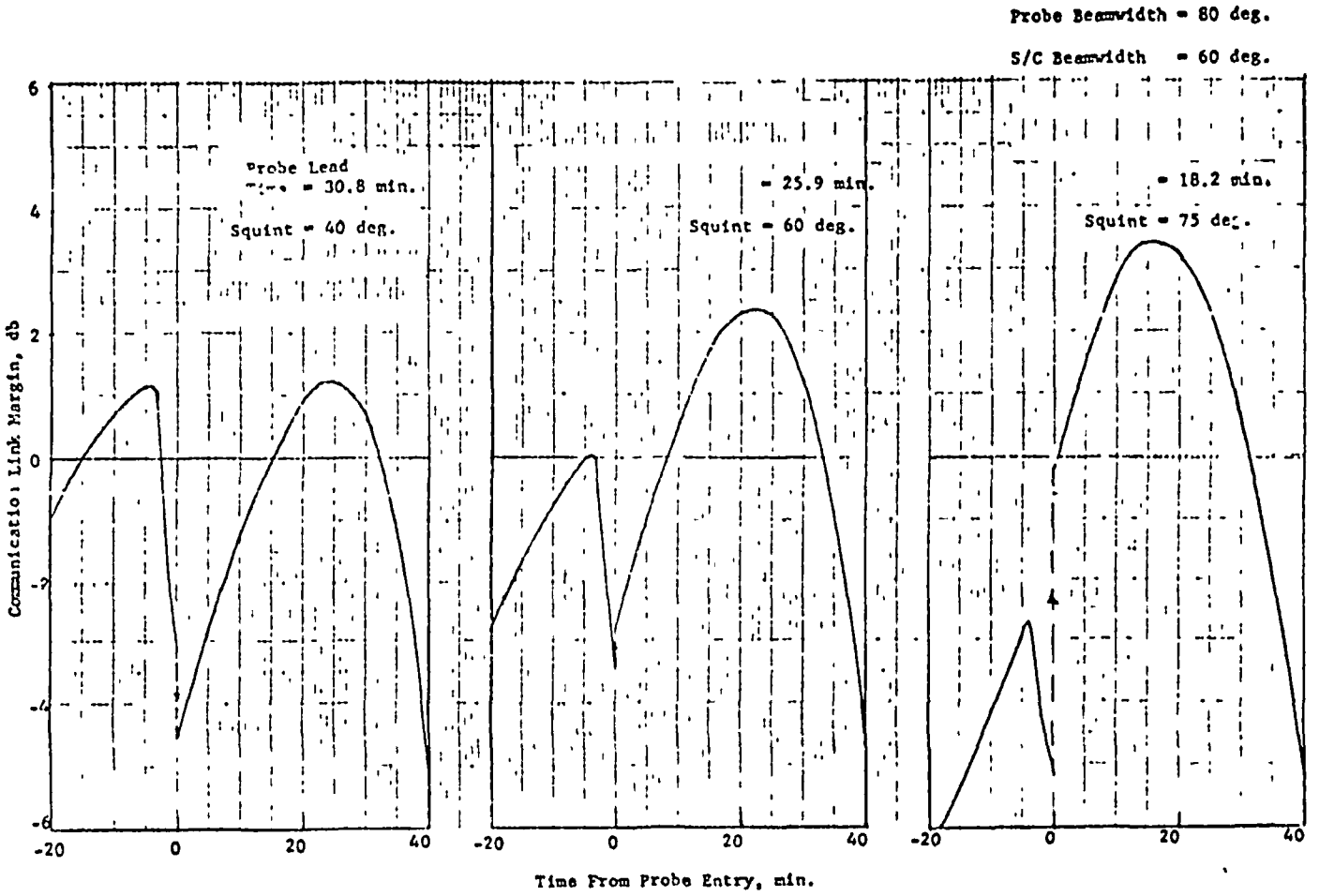


FIGURE 2 20 LINK MARGIN FOR SPACECRAFT IN EQUATORIAL PLANE AND A 16 DEGREE PROBE ENTRY LATITUDE

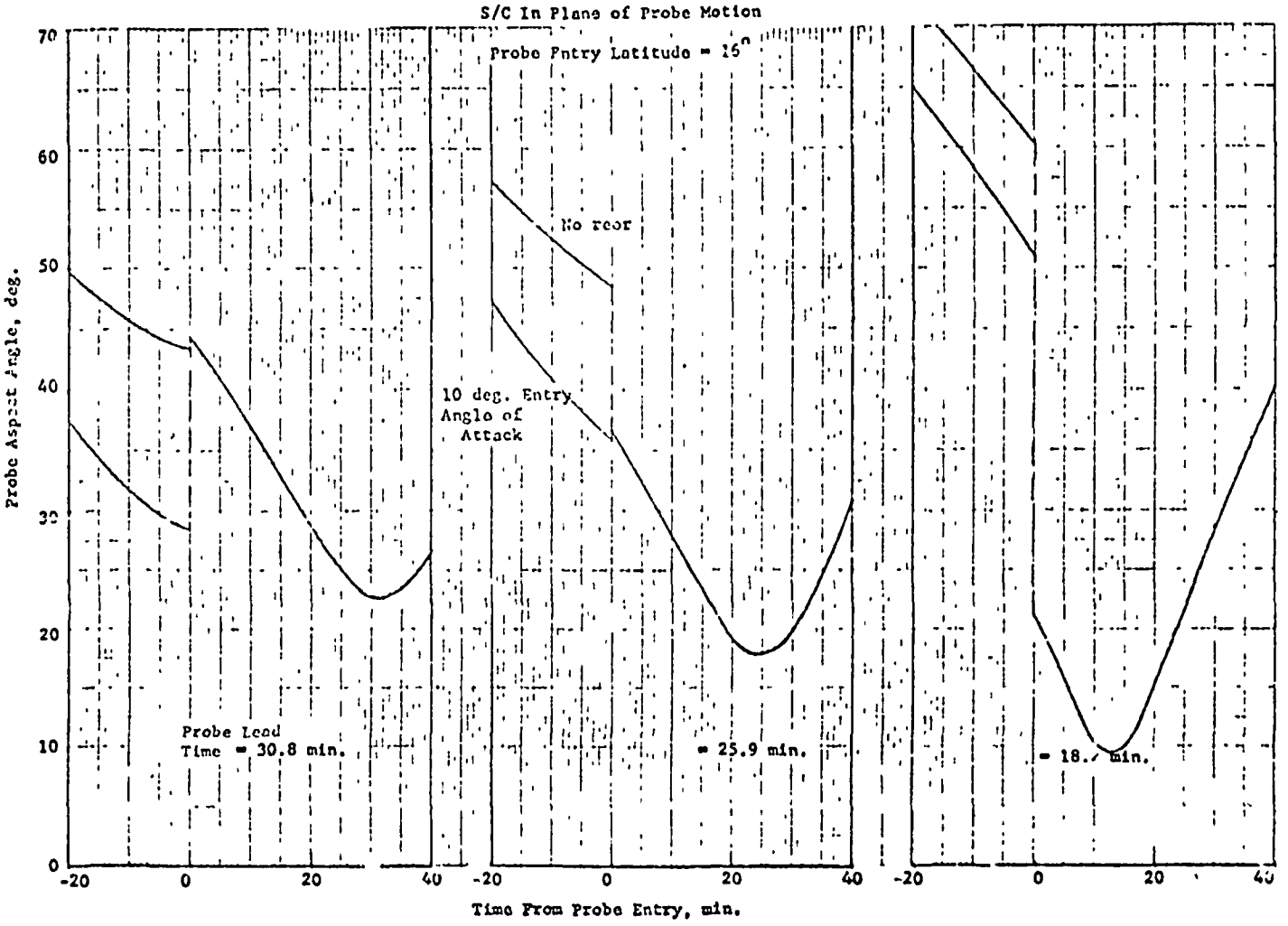


FIGURE 2 21 PROBE ASPECT ANGLE FOR SPACECRAFT IN PLANE OF PROBE MOTION

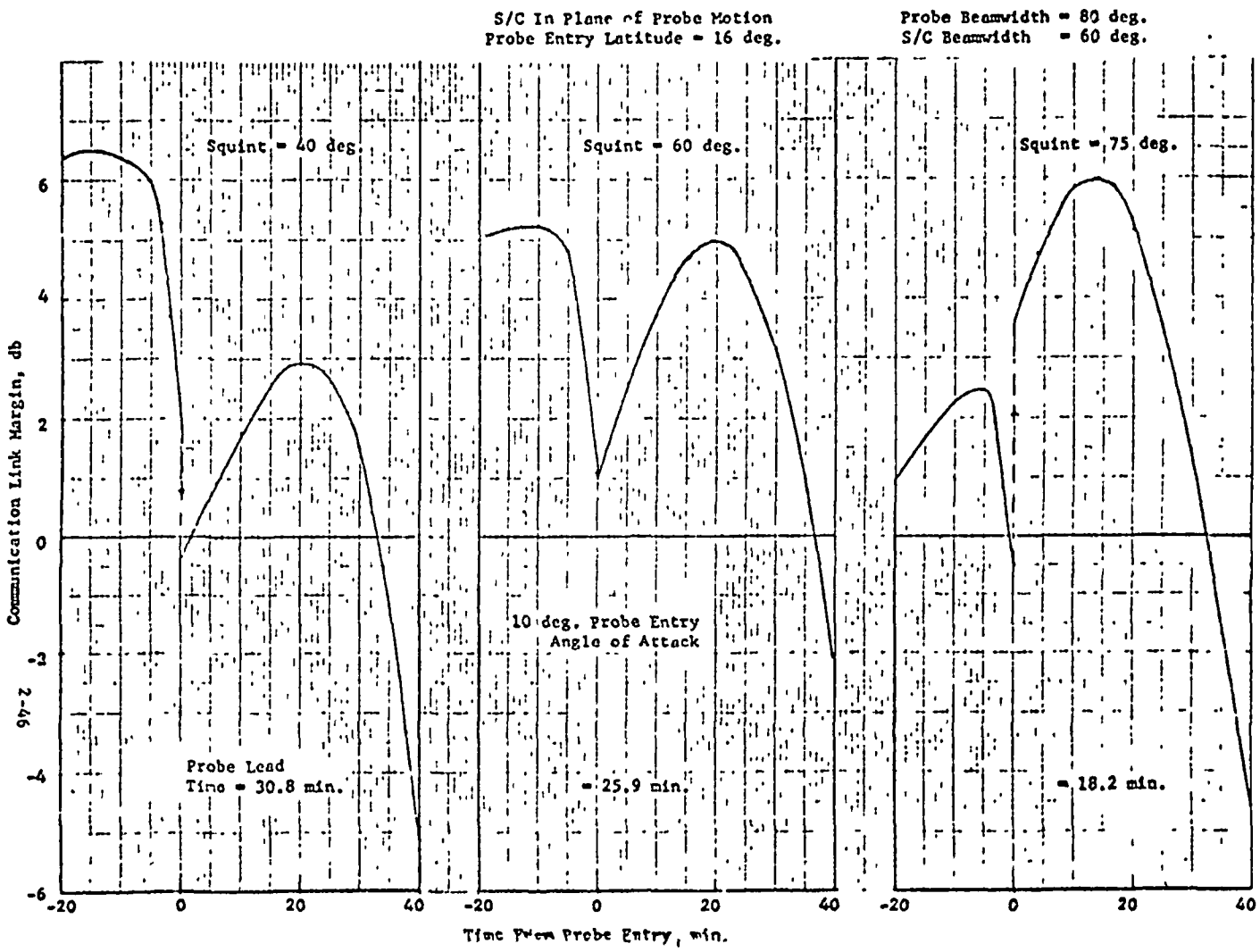


FIGURE 2 22 LINK MARGIN FOR SPACECRAFT IN PLANE OF PROBE MOTION

2.5 COMMENTS AND CONCLUSIONS

The above discussion has indicated that the environmental factors and antenna patterns can be modeled for machine computation to determine link capacity as a function of time. Then, given quantitative and/or qualitative criteria, a set of optimum system design parameters can be chosen.

A representative set of criteria might be:

1) Equalize peak capacity for both pre- and postentry.

2) Initial postentry margin must be greater than 1.0 dB.

3) Maximize the period of positive postentry margin, but not to be less than 30 minutes.

One set of parameters, not necessarily optimum, meeting these criteria are as follows:

1) Spacecraft periapsis distance = 1.8 R_J

2) Probe lead time = 26.7 minutes

3) Spacecraft antenna beamwidth = 60°

4) Spacecraft squint angle = 45°

5) Probe antenna beamwidth = 70°

When antenna constraints are more clearly defined, a finer variation of these parameters may lead to a more optimum choice, i.e., may increase link capacity.

In conclusion, it should be pointed out that there is considerable uncertainty in two of the environmental factors which significantly affect link capacity: ionospheric scintillation and synchrotron noise. Richard Woo in Reference 2-4 has stated that his estimate of scintillation has only order-of-magnitude accuracy. More recent analysis of Pioneer 11 data has led him to increase his confidence to within a factor of two or three. A factor of two or three greater (multiplied directly to the decibel fading loss) would greatly reduce the capacity of the link and probably require higher frequencies. Also the fading model used by Woo may be questioned at much higher levels. Synchrotron noise has been scaled from relatively crude, but best available, measurements at 10 and 21 cm wavelengths (see Reference 2-8). These environmental uncertainties overshadow all link analysis, including that discussed above, and raise the question of the viability of this link except for very low data rates less than 10 bps. Somewhat more accurate measurements of the synchrotron noise are possible with earth-based antennas, but ionosphere measurements require transmissions from flyby spacecraft and no more such missions to Jupiter are planned prior to design commitments to a probe mission.

The solution of this dilemma is not clear, but will probably require some combination of risk acceptance and communication link overdesign or the use of higher frequencies and higher gain antennas.

2.6 REFERENCES

2-1) "The Planet Jupiter (1970)," NASA Space Vehicle Design Criteria, NASA SP-8069, December 1971.

2-2) "Outer Planet Entry Probe System Study," Volume III, Final Report, Martin Marietta Corp. August 1972.

2-3) "Jupiter Atmospheric Entry Mission Study, Final Report," Volumes II and III, Martin Marietta Corp., April 1971.

2-4) Woo, R. and Yang, F. C., "Scintillation Estimates for a Jupiter Entry Probe — Phase I," Report No. TM33-745, NASA, JPL, November 1975.

2-5) Woo, R., Kendall, W., Ishimaru, A., and Berwin, R., "Effects of Turbulence in the Atmosphere of Venus on Pioneer Venus Radio — Phase I," Jet Propulsion Laboratory Technical Memorandum 33-644, 30 June 1973.

2-6) "Technology Forecasting for Space Communication, Task Three Report: STDN Antenna and Preamplifier Cost Tradeoff Study," Hughes Aircraft Company for NASA GSFC, SCG 30195R, May 1973.

2-7) Rasmussen, David A., Grant, Terry L., and Noble, Steve C., "Jupiter Antenna Noise Distribution Program," unpublished report prepared at NASA, ARC, 1975.

2-8) Berge, G. L., "An Interferometric Study of Jupiter at 10 and 21 cm," Radio Science, 69D, 1552, 1965.

3. SYSTEM CONCEPTUAL DESIGN

The previous section has discussed the selection of the overall communication link parameters. This section describes very briefly a design concept for a probe preentry communication subsystem to be used exclusively for preentry and jettisoned prior to entry. This system has the capability for optional dual frequency transmission to allow doppler measurements at two frequencies. Such measurements would allow more accurate determination of the ionosphere structure, eliminating the need for accurate knowledge of the probe carrier frequency.

In considering modulation, it was felt that a discrete carrier with a data subcarrier would simplify the spacecraft receiver and allow more accurate doppler measurement. Referring to Table 2-3, biphase FSK was assumed as a baseline for the link margin calculations, but if a discrete carrier system is assumed with approximately one-half of the transmitted power in the carrier, then the data power will be only 30 of the 60 watts assumed in Section 2. This 3 dB reduction in transmitted data power can be offset by using biphase PSK which requires approximately 3 dB less bit energy-to-noise density. With this approach, the link margin calculations of Section 2 apply to the system described here.

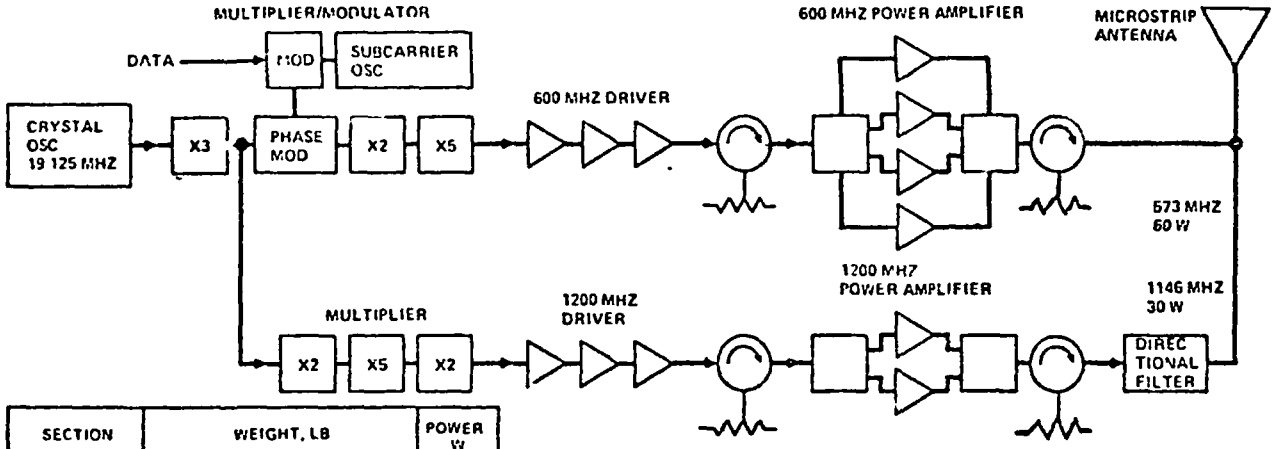
Figure 3-1 illustrates the design concept. The upper portion is the data communication subsystem which, as just mentioned, corresponds to a coherent link with a discrete carrier for doppler measurement and the data on a subcarrier. The primary frequency is a NASA standard, the same as on MJS and Pioneer Venus. The result of multiplication is an output carrier frequency of approximately 573 MHz (close to the recommended 600 MHz).

The lower portion of the block diagram represents the functions for producing an RF carrier at 1146 MHz (twice the above frequency). The power amplifiers feed a dual frequency microstrip antenna, and a directional filter in the high frequency line isolates the output stages The physical parameters are listed at the lower left of Figure 3-1. The values for power correspond to the 60 and 30 watts for the respective sections. These estimates were determined from more detailed estimates for each of the major functions.

The question of antenna implementation is not clear, but presents one of the greater difficulties if two frequencies are to be transmitted. Placing two antennas on the probe with less than a wavelength between them

will result in mutual interference and/or difficult antenna configurations in order to produce nearly identical radiation patterns. Although it is feasible to put two crossed dipole or helical antennas on a rear mounted package, the microstrip offers the potential for dual frequency operation. Because it is employed in the current baseline probe and offers a convenient configuration for this application, it has been selected for this concept for dual frequency use. Further analysis is required to determine its specific dual frequency performance.

Figure 3-2 illustrates a concept for mounting the antenna, communication, science, and other equipment on a probe, with minimum impact on probe design. The support structure attaches to the baseline probe at the three points used for attaching the combined vehicle to the orbiter. This is the only required contact with the probe, and these attach points must be designed to accommodate two separations: one from the orbiter and one to jettison the preentry package just prior to entry. The equipment is shown conceptually as three conformal sections, but will, in all likelihood, consist of considerably more individual boxes mounted on the support structure. The system of Figure 2-1 will require about 20 to 25 percent of the support structure capacity. The remainder is available for batteries, science, and/or data handling equipment. Figure 3-3 illustrates this concept with a back and side view.



SECTION	WEIGHT, LB	POWER W
600 MHZ	52 (INCLUDES ANTENNA)	142
1200 MHZ	31	85
SUPPORT STRUCTURE	63 (FOR ALL SUBSYSTEMS)	–

FIGURE 3 1 PROBE REENTRY COMMUNICATION SUBSYSTEM

A. E. Kuhlman, Microstrip Antenna Study for Pioneer Saturn/Uranus Atmosphere Entry Probe, McDonnell Douglas Report for NASA ARC under Contract NAS 2-7328, May 1974.

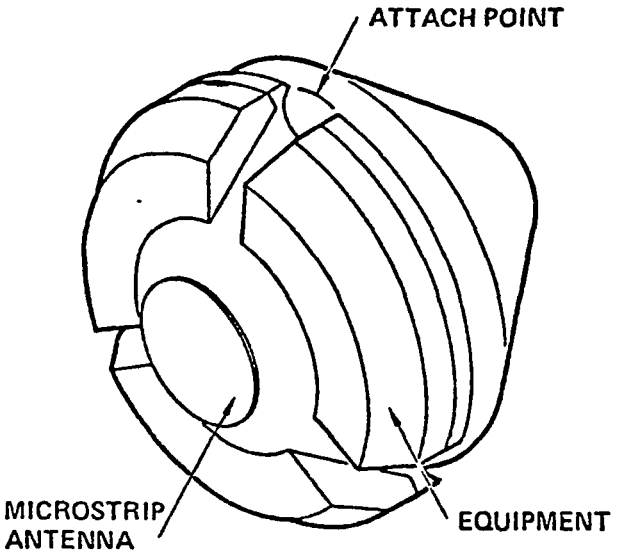


FIGURE 3-2 PREENTRY EXTERNAL COMMUNICATION SYSTEM

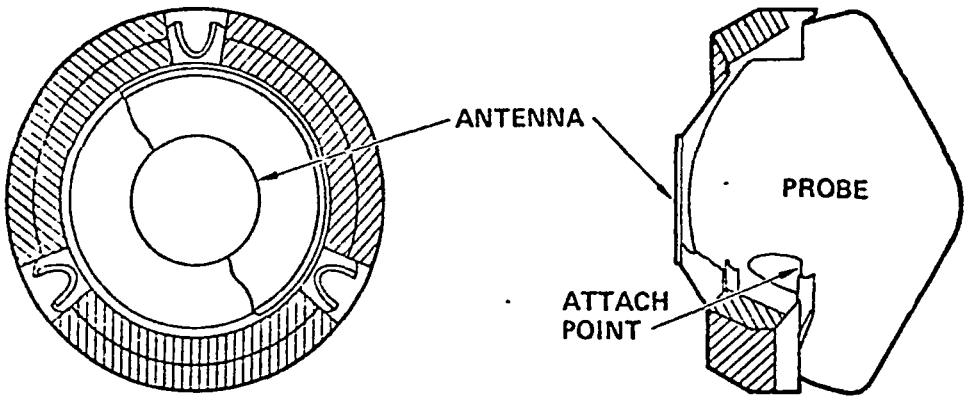


FIGURE 3-3 PREENTRY EXTERNAL COMMUNICATION SUBSYSTEM

4. DOPPLER MEASUREMENT ANALYSIS

4.1 INTRODUCTION AND SUMMARY

Accurate measurement of the doppler shift of the probe transmitted signal will provide a means for determining properties of the ionosphere and may aid in postmission determination of the probe descent trajectory and impact point. The purpose of this task was to investigate the sources of error in measuring the doppler shift of the carrier frequency transmitted by the probe. The measurement error results from: 1) error in the estimate of the probe transmitted frequency, 2) receiver frequency measurement error, and 3) error produced by the transmission environment. By limiting or minimizing the first two sources, the third can be estimated and used to derive information on the propagation environment. Estimation of the probe transmitted frequency is limited by attainable accuracy performance of space-qualified quartz oscillators; however, considerable latitude exists in configuring the spacecraft receiver for accurate determination of the received frequency. This investigation has considered both subjects but has emphasized the receiver performance.

The accuracy of the frequency measurement depends primarily on the fidelity of the receiver generated replica of the actual received frequency as well as the accuracy with which the replica frequency can be measured. The major error in determining the received frequency results from receiver tracking performance limitations due to noise, doppler, and scintillation. The doppler extractor and counter/resolver error contribution may be made relatively insignificant, so that receiver tracking performance is the major contribution to frequency measurement error. A computer simulation was developed employing the SYSTID time domain simulation software available at Hughes to determine the tracking performance of an appropriate designed carrier tracking receiver in the Pioneer Jupiter Orbiter Probe (PJOP) doppler and scintillation environment. The most severe expected doppler environment and conservative estimates of scintillation were assumed. A double heterodyne carrier tracking phase-locked receiver with bandpass limiting was taken as the basis of this computer simulation, corresponding to the system described in the previous section, where a discrete carrier is employed with data modulated on a subcarrier outside the carrier loop bandwidth. A carrier tracking loop SNR corresponding to 10 dB in the two-sided loop threshold noise bandwidth was assumed. For a typical

doppler measurement time of 0.10 second and a scintillation bandwidth of 0.10 Hz, the receiver doppler measurement error is approximately 2.3 Hz.

4.2 PROBE TRANSMITTER OPTIONS

Error in the probe transmitted frequency estimate contributes directly to error in the one-way doppler measurement. A one-way doppler measurement accuracy of several Hertz requires fractional Hertz accuracy in the probe transmitted frequency estimate. The probe frequency must be known to the required accuracy over the approximately 30 minute preentry communication period occurring some 50 days after probe-bus separation. During the 50 day coast period, the probe is dormant except for a warmup period (of critical duration) prior to the operating period. This performance approaches state of the art for quartz oscillators and may be the ultimate limitation in achievable one-way doppler measurement accuracy.

Atomic as well as quartz frequency standards have been investigated. Space-qualified atomic frequency standards have been developed in connection with the Air Force NAVSTAR Global Positioning System. Weight, volume, power, and relative stability of quartz and atomic frequency standards are compared in Table 4-1 (Reference 4-1). The values shown for quartz and rubidium standards are based on existing flight-qualified units. The cesium and hydrogen maser values reflect present capabilities rather than existing hardware. Despite their superior performance, atomic standards must be excluded from serious consideration for use on PJOP by their untenable power requirements, weight, and uncertain reliability.

Existing space-qualified quartz frequency standards are compared in greater detail in Table 4-2. Present capabilities are typified by the Mariner Jupiter-Saturn (MJS) and the Pioneer Venus (PV) small probe standards. The MJS oscillator represents state of the art performance for a double proportional oven unit with an extended warmup period. The PV small probe unit is a double proportional oven design required to survive the deceleration of planetary entry. The mechanical packaging required to assure entry survivability is not conductive to most efficient warmup and as a result, accuracy is compromised. Greatly improved accuracy (see Table 4-2) could be achieved

TABLE 4 1 QUARTZ AND ATOMIC SPACE FREQUENCY STANDARDS COMPARED

	Quartz (MJS)	Rubidium Vapor	Cesium	H_2 Maser
Weight lb	25	5	30	75
Power, W	15	13	25	30
Volume, ft^3	0 04	0 04	0 4	1
Stability $\Delta f/f$	10^{11}	10^{12}	10^{13}	10^{14}

TABLE 4 2 QUARTZ SPACE FREQUENCY STANDARDS COMPARED

	MJS	PV Small Probe	PJOP Preentry Communications
Cost (5 units) SK	300	150	150
Weight, lb	2 5	0 75	0 75
Stability, $\Delta f/f$	10^{-11}	10^{-9}	10^{-9}
Accuracy, $\Delta f/f$	10^{-7}	10^{-6}	10^{-8} to 2×10^{-9}
Warmup time	11 days	90 min	1 5 to 20 hr
Power	1 5 W	1 4 W	1 2 W

in the same mechanical package as the present PV unit if the deceleration tolerance were relaxed for preentry operation only, permitting more efficient thermal packaging (Reference 4-2). Figure 4-1 based upon discussions with Frequency Electronics, Inc., shows attainable frequency accuracy for such a unit as a function of warmup time. Warmup power is a constant 1.2 watts except for an initial 18 minutes at 5 watts. The critical performance parameter for one-way doppler measurement is accuracy. Stability in excess of accuracy is useful only if calibration can be performed with commensurate precision.

Three options were considered for achieving the required performance:

1) Provide required accuracy from launch to end of mission with commensurate stability over the preentry communication period. The most accurate existing space-qualified quartz frequency standard is the MJS unit which is capable of 10^{-7} accuracy over 3 years with an 11 day warmup period. For the nominal carrier frequency of 600 MHz $\Delta f/f = 10^{-7}$ represents a frequency uncertainty of 60 Hz and a corresponding R uncertainty (at 600 MHz) of 30 m/sec. Insufficient accuracy and prohibitive warmup energy preclude this approach.

2) A second approach, suggested for PV postmission calibration of the small probe oscillator, has been shown by analysis to provide frequency calibration to the limit of oscillator stability ($\Delta f/f = 10^{-9}$) by postmission analysis of received frequency and ephemeris data (Reference 4-3). The probe-earth asymptotic velocity, V_o, is accurately estimated from two-way DSN tracking of the bus and probe release conditions. The probe-bus acceleration during the preentry descent, derived from postmission analysis of received frequency data, is then used in conjunction with V_o to estimate probe-earth velocity versus time during the descent

$$V = V_o + at$$

The transmitted frequency may then be determined from

$$V = \left(1 - \frac{f_r}{f_t}\right) c$$

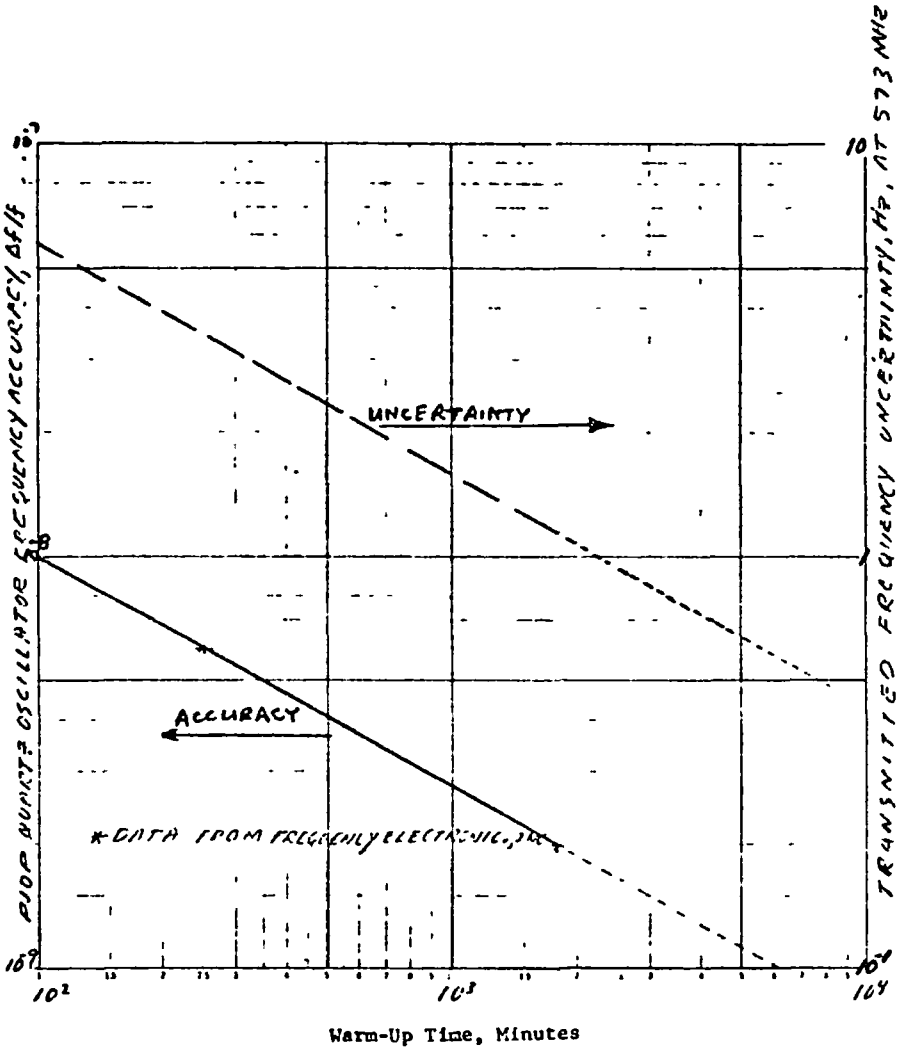


FIGURE 4-1. PJOP QUARTZ OSCILLATOR ACCURACY VERSUS PRE COMMUNICATION WARMUP TIME (AT 1 2 WATTS INPUT POWER)

The accuracy of this calibration technique depends on the existence of the direct probe-earth link. Probe-earth acceleration determined from

$$a = \frac{d(f_t)}{dt}\,\frac{c}{f_t} - \frac{cf_r}{f_t^2}\,\frac{d(f_t)}{dt}$$

during the low acceleration (<6 m/sec^2) portion of the probe descent introduces a small error in V since $V_o \gg$ at and V_o is known to relatively high accuracy from DSN tracking. This method is not applicable to the PJOP mission as presently envisioned, since a direct probe-earth link is required for accurate determination of the relative transmitter-receiver velocity.

3) A third and feasible approach is to calibrate the probe oscillator prior to separation from the bus in order to achieve required accuracy when it is activated at preentry. Prior to separation, the probe oscillator can be calibrated against the bus transponder auxiliary oscillator, which, in turn, may be calibrated against the DSN ground standard to an accuracy greater than 10^{-10}. Probe oscillator calibration could be accomplished either by a direct connection to the bus doppler counter/resolver or via RF coupling (which would verify performance of the doppler measurement subsystem as well). The latter option would minimize the probe-bus interface. Since provision will already exist for power transfer to permit preseparation charging of the probe batteries, oscillator warmup and testing would use the bus power supply rather than drain the probe battery. Vendor discussions indicate attainable frequency accuracy at preentry of $\Delta f/f = 1 \times 10^{8}$ to 2×10^{9} depending on prior warmup time (Figure 4-1) (neglecting radiation effects, which can be corrected for if the radiation levels are known). This performance would be attainable with a quartz standard having a mechanical package identical to the PV small probe oscillator but with more efficient warmup characteristics achievable by more thermally efficient packaging appropriate to relaxed deceleration tolerance requirements.

4.3 OPERATIONAL ENVIRONMENT ASSUMPTIONS

The environmental parameters critical to one-way doppler measurement include those which dictate the design of the doppler tracking system or affect its performance, as well as those which contribute directly to doppler error.

4.3.1 Doppler Shift and Doppler Rate

The doppler shift and doppler rate for the probe-bus link are functions of the probe-bus trajectory phasing. Examination of various probe-bus

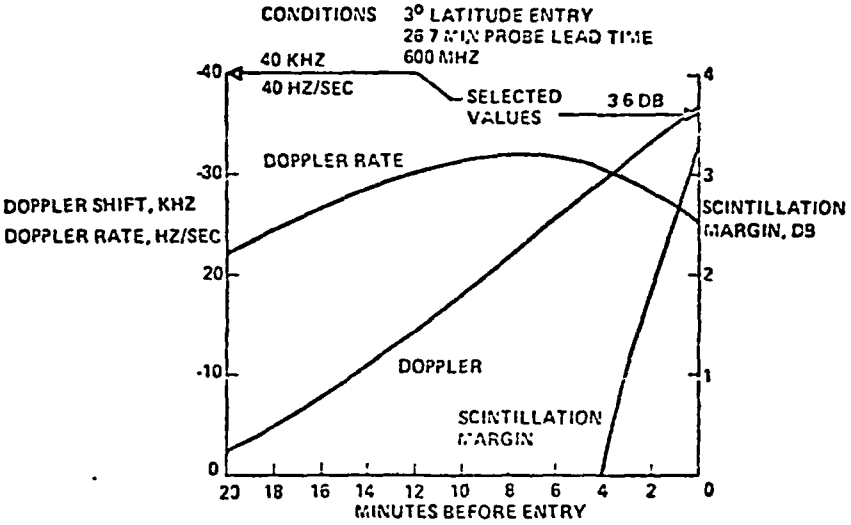


FIGURE 4 2 DOPPLER SHIFT, DOPPLER RATE, AND SCINTILLATION MARGIN VERSUS TIME

phasings acceptable from a communication link budget standpoint indicates that a typical severe situation is represented by Figure 4-2, which depicts doppler shift and doppler rate for the 600 MHz probe-bus link. Figure 4-2 indicates a maximum doppler rate of approximately 32 Hz/sec and a range of doppler shift of 36 kHz. Conservatively, more severe values of 40 Hz/sec doppler rate and 40 kHz doppler shift have been assumed for the receiver tracking simulation.

4.3.2 Scintillation Environment

The exact nature and extent of the Jovian ionospheric scintillation environment are a subject of some conjecture. The scintillation environment for the receiver tracking simulation is based upon the analysis of Pioneer 10 data by Woo and Yang (Reference 4-4). The scintillation model reflects the random fluctuations in amplitude and phase of the received signal resulting from the electron density irregularities in the ionosphere. The received signal amplitude fluctuations are inferred from theoretical considerations (supported by experimental evidence) to have a log-normal distribution. The phase fluctuations have a gaussian distribution. The variance of the log-amplitude fluctuations is given (for $\sigma^2_{lnA} < 1$) by

$$\sigma^2_{lnA} = 0.308\ c_n^2\ k^{7/6}\ L^{11/6}$$

where

c_n = structure constant

k = free space wave number

L = ray path distance through ionospheric irregularities

The upper limit of c_n determined by Woo from Pioneer 10 observations is $c_n = 5 \times 10^{-8}\ km^{-1/3}$. For L = 3547 km, corresponding to a conservative worst case zenith angle of 45° (determined from probe-bus trajectory phasing studies), the log-amplitude variance is determined to be

$$\sigma^2_{lnA} = 3.2 \times 10^{-2}$$

for a frequency of 600 MHz. The corresponding rms power fading given by

$$F_{rms} = 20 \log_{10}(e)\,\sigma_{lnA}$$

is

$$F_{rms} = -1.55\ dB$$

The corresponding power facing which is not exceeded more than one percent of the time is

$$F_{1\%} = -2.327 \cdot F_{rms} = -3.62 \text{ dB}$$

The variance of the phase fluctuations is given by

$$\sigma_\phi^2 = 0.782 K^2 L_o^{5/3} c_r^2 L - \sigma_{lnA}^2 \text{rad}^2$$

where L_o is the outer scale size of the electron density irregularities. From Pioneer 10 observations, L_o has been determined to exceed 6 km. For a postulated value of L_o = 10 km, the phase variance is

$$\sigma_\phi^2 = 10.94 \text{ rad}^2$$

The spectral distribution of the phase scintillation is critical to receiver carrier tracking. Since the estimated phase scintillation variance is large compared to the loop phase error at which loss of lock occurs ($\pi/2$), rapid phase variations would impair or preclude carrier tracking. However, for scintillation spectra bandwidth small compared to tracking loop bandwidth (slow phase variations), the loop tracks the perturbed phase without significant performance degradation. Both amplitude and phase scintillation are, in fact, observed to have relatively narrow spectral bandwidths.

The -3 dB bandwidth of the log-amplitude fluctuations is given by

$$f_{3 \text{ dB}} = 0.294 V_\perp \sqrt{k/L}$$

where $V_\perp$ is the component of ionospheric wind velocity transverse to the line of sight path. Woo postulates a $V_\perp$ = 100 m/sec. The corresponding 3 dB bandwidth at 600 MHz for a 0° line of sight zenith angle is

$$f_{3 \text{ dB}} = 0.065 \text{ Hz}$$

where L (2550 km) is the vertical path length through the ionosphere at entry altitude (450 km). It will be noted that the bandwidth is relatively insensitive to zenith angle because of its $1/\sqrt{L}$ dependence. Woo asserts that the spectrum of the scintillation is similarly narrow.

4.3.3 Scintillation Computer Modeling

The scintillation computer modeling is implemented by means of time domain sample data simulation using the Hughes developed SYSTID program. SYSTID creates and executes a FORTRAN program to simulate the time

TABLE 4 3 SUMMARY OF COMPUTER SCINTILLATION MODELING STATISTICS

Scintillation -3 dB Bandwidth	σ_{lnA}	$\sigma_{\dot{A}}$	$\sigma_{\ddot{A}}$	σ_{ϕ}, rad	$\sigma_{\dot{\phi}}$, Hz/sec	$\sigma_{\ddot{\phi}}$, Hz/sec^2
0 10 Hz	0 1789	0 06929	0 03568	3 3076	0 2070	0 1047
1 0 Hz	0 1789	0 6929	3 568	3 3076	2 070	10 47

response of a system described in terms of its functional block diagram. Normal distributions of log-amplitude and phase samples having a uniform power spectral density are derived by a gaussian random number generator. The resultant phase and amplitude functions are then numerically filtered to obtain the desired spectral distribution. The -8/3 power frequency dependence theoretically determined by Woo (Reference 4-5) for both the phase and log-amplitude power spectral density was closely approximated by a 9th order Butterworth filter. A 0.10 Hz scintillation bandwidth (-3 dB) corresponding to Woo's theoretical estimate and a more adverse 1.0 Hz bandwidth were chosen for the simulation.

The results of the scintillation simulation modeling are illustrated in Figures 4-3 through 4-6. Figures 4-3 and 4-4 are the distributions of the actual simulation generated band-limited log-amplitude and phase data. It may be noted that the standard deviations of phase and log-amplitude correspond to σ_{ϕ}^2 and σ_{lnA} calculated in subsection 4.3.2. The means of the phase and log-amplitude distributions are seen to be negligibly small compared to their respective standard deviations. Figure 4-5, for the 0.10 Hz bandwidth, depicts phase scintillation and power fading (due to amplitude scintillation) as a function of time over a 2000 second observation period.

The power spectral density distributions of the simulation generated phase and log-amplitude scintillation data are presented in Figure 4-6 for the 0.10 Hz bandwidth case. The scintillation phase rate contribution degrades doppler measurement accuracy both by contributing a pseudo-doppler component and through its effect on receiver tracking performance. Table 4-3 summarizes the standard deviations of the distributions of phase and amplitude scintillation rates and accelerations (obtained by numerical differentiation of the simulation results) for the 0.10 and 1.0 Hz bandwidths.

4.4 SPACECRAFT RECEIVER CARRIER TRACKING SIMULATION

4.4.1 System Configuration Assumptions

A double heterodyne carrier tracking phase-locked loop receiver with bandpass limiting has been chosen for the spacecraft terminal. The carrier tracking requirement is indicated by the 36 kHz variation in doppler shifted

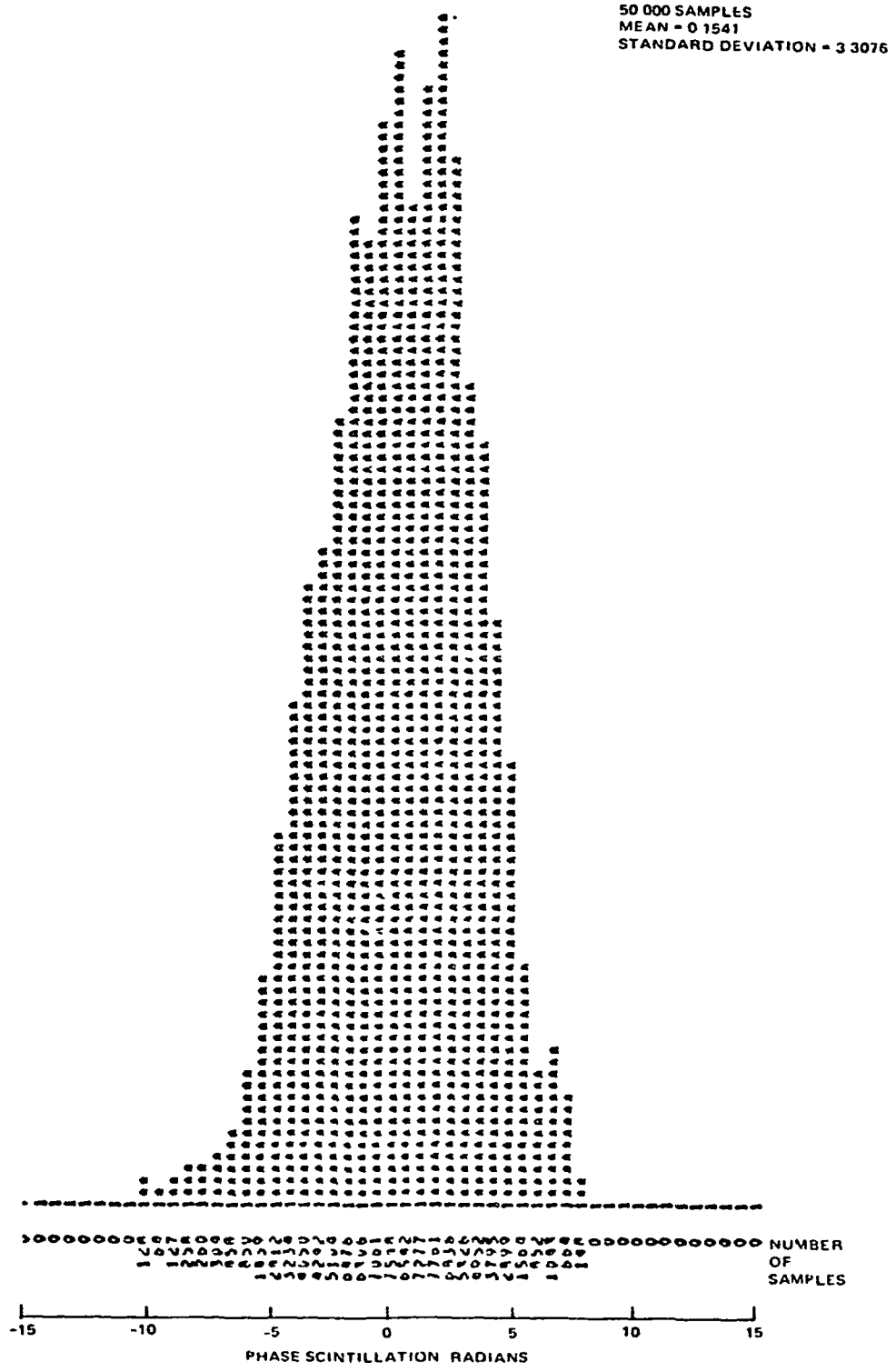


FIGURE 4 3 COMPUTER MODELED PHASE SCINTILLATION SAMPLE DISTRIBUTION–
0 10 HZ SCINTILLATION BANDWIDTH

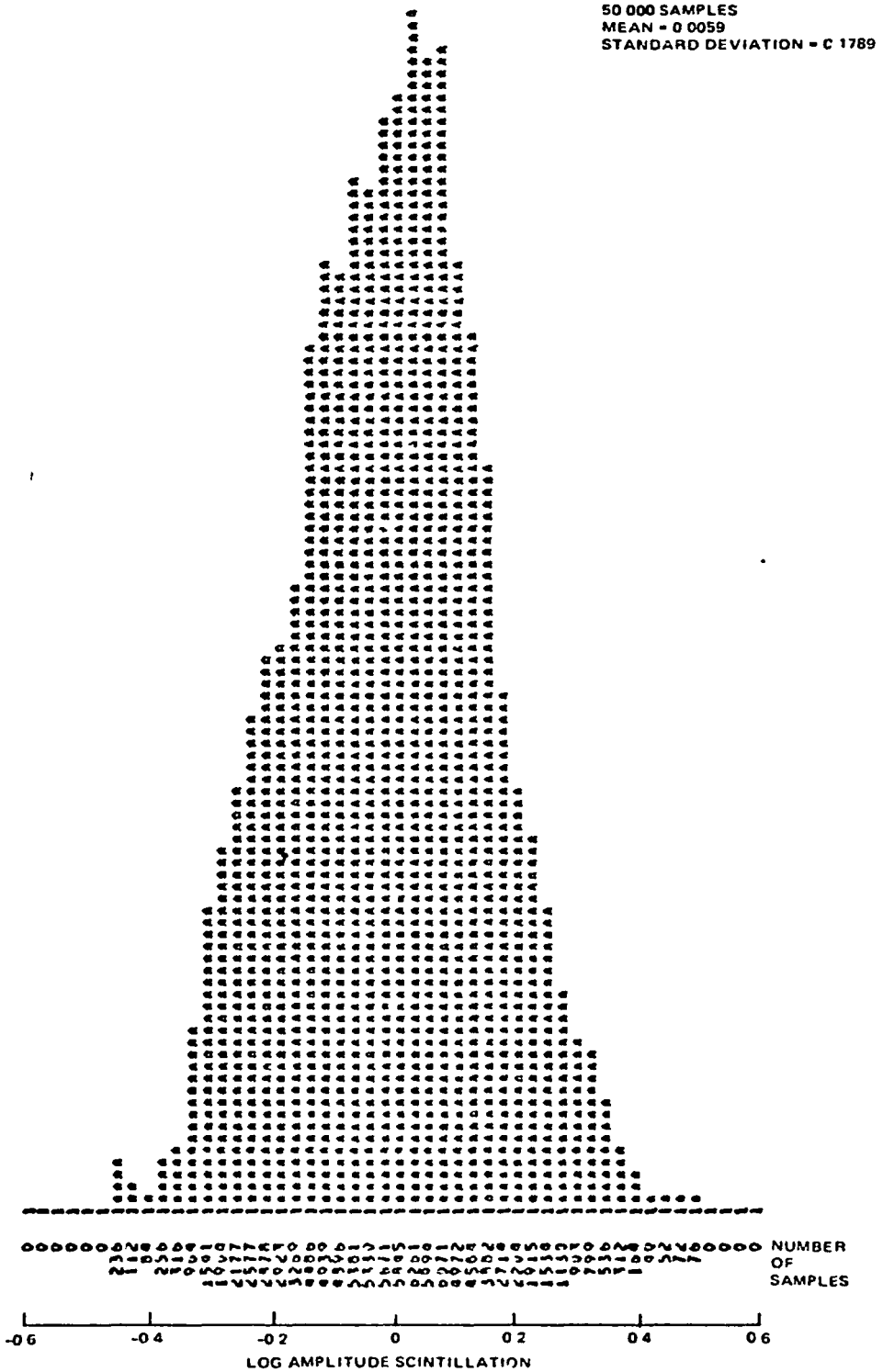


FIGURE 4-4 COMPUTER MODELED LOG AMPLITUDE SCINTILLATION DISTRIBUTION– 0 10 HZ SCINTILLATION BANDWIDTH

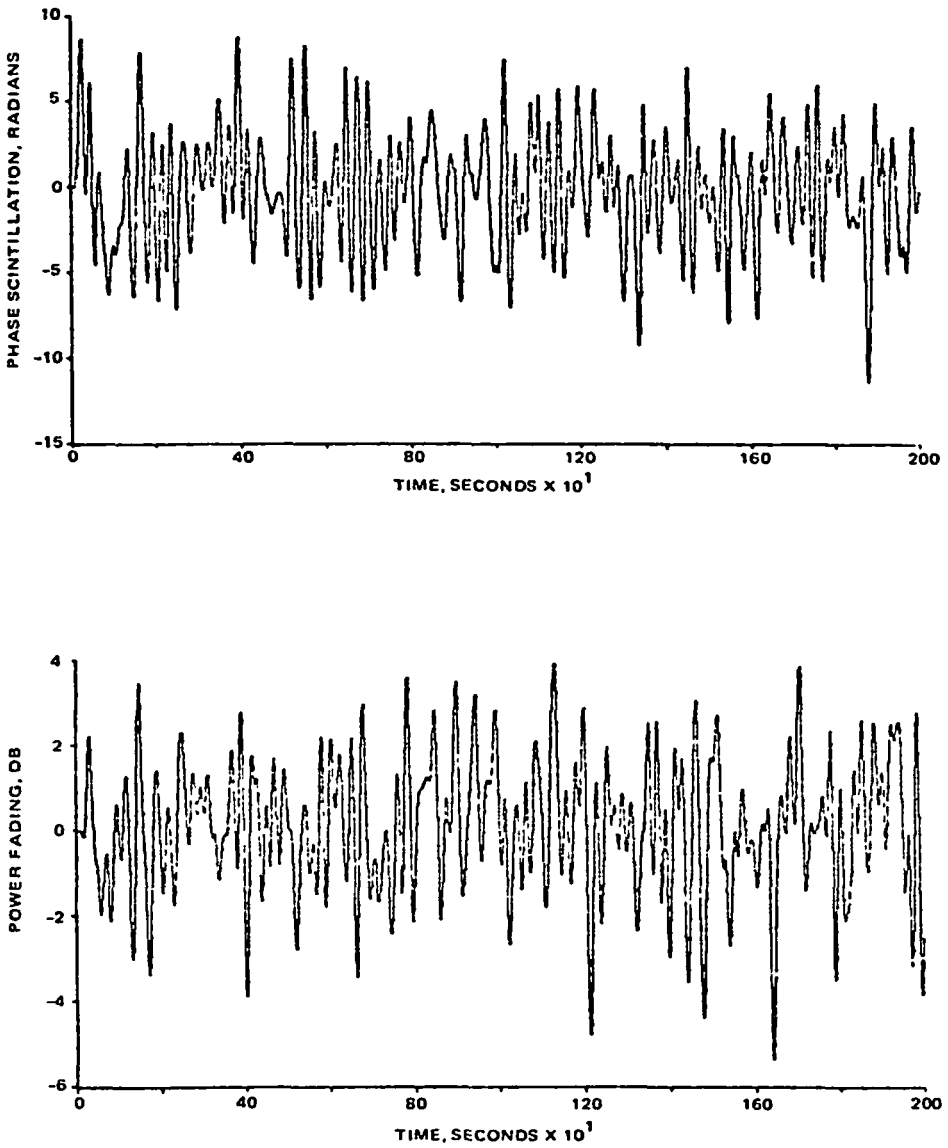
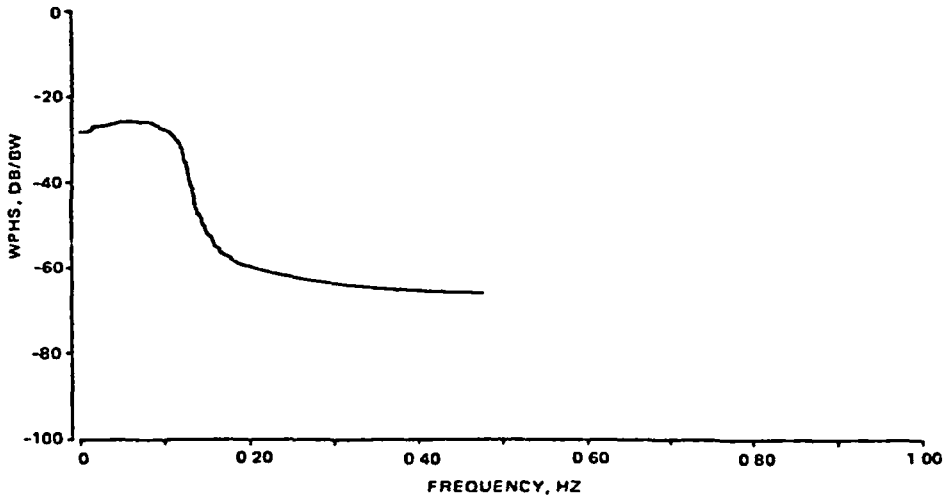


FIGURE 4 5 COMPUTER MODEL OUTPUTS OF PHASE SCINTILLATION (UPPER) AND AMPLITUDE SCINTILLATION (LOWER) VERSUS TIME (0 10 Hz SCINTILLATION BANDWIDTH)



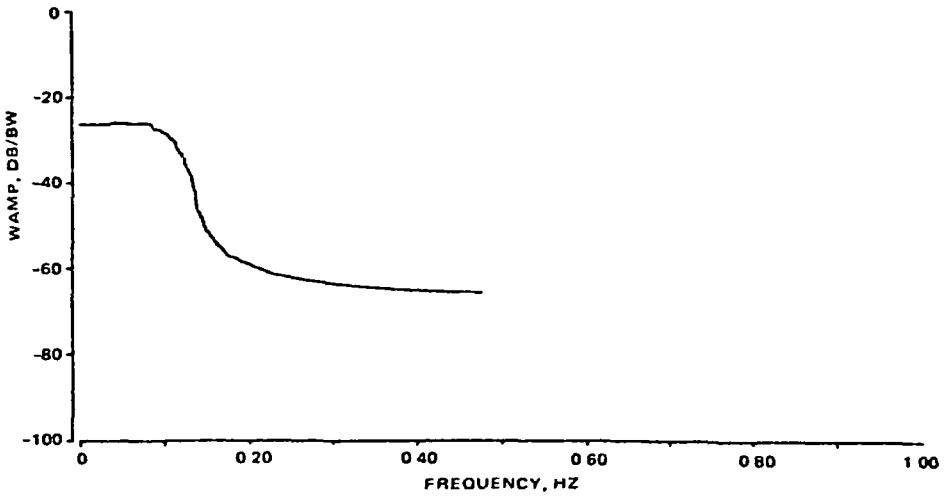


FIGURE 4-6 SPECTRAL DISTRIBUTION OF 0 10 Hz = -3 DB BANDWIDTH PHASE (UPPER) AND AMPLITUDE (LOWER) SCINTILLATION

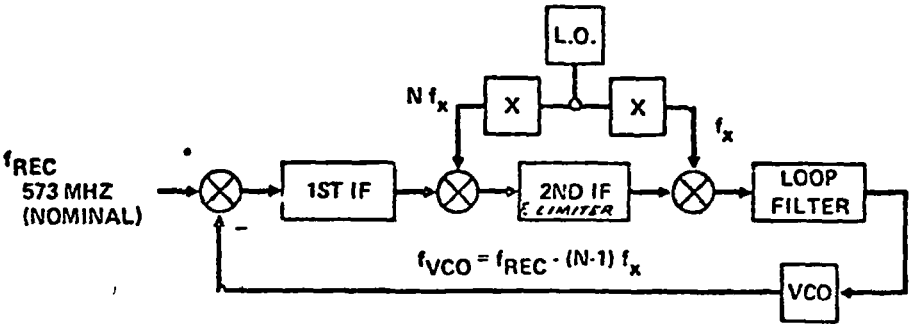


FIGURE 4-7 GENERALIZED CARRIER TRACKING RECEIVER

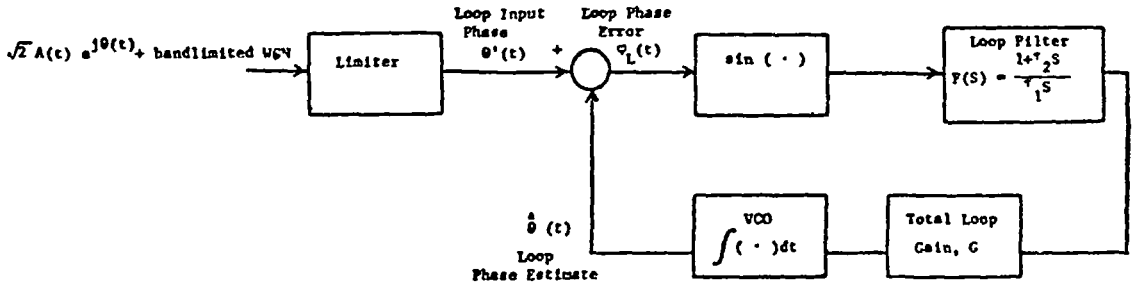


FIGURE 4-8. LOWPASS EQUIVALENT PHASE REPRESENTATION OF THE GENERALIZED CARRIER TRACKING RECEIVER

carrier frequency and the much narrower receiver bandwidth required to achieve acceptable carrier replica signal/noise for doppler measurement. The bandpass limiter provides adaptive loop bandwidth control, resulting in enhanced doppler rate tracking and acquisition performance for loop operation above threshold. The assumed discrete carrier permits a narrower loop bandwidth for given tracking performance and simplifies analysis by leaving open the choice of modulation. While allocation of power to the discrete carrier reduces available data power, the carrier derived phase reference permits coherent demodulation with up to a 3 dB enhancement in data signal/noise. In general, the optimal allocation of total power between the carrier and the data channel is determined by the functional dependence of system losses on the modulation index. This dependence, in turn, depends on the type of modulation used. In the interest of generality, a carrier suppression of 3 dB ($P_C/P_T = 0.5$) is assumed. This choice provides a meaningful comparison between a (generally) nonoptimal discrete carrier system with a coherently demodulated subcarrier and a noncoherent system with data on the carrier. The relative 3 dB data power reduction, due to carrier suppression of the former, is compensated by its 3 dB enhancement from coherent demodulation (assuming that the demodulation loss due to noisy phase reference is relatively small).

The IF and carrier tracking section of a general double heterodyne receiver is shown schematically in Figure 4-7. If the IF filter transfer function along the imaginary axis is locally symmetric about $\pm i\omega_{carrier}$ it may be shown (Reference 4-6) that the carrier tracking loop may be represented by its low-pass equivalent (Figure 4-8). The equivalent input to the low-pass loop is then the received carrier with frequency translated downward by the transmitted carrier frequency. The receiver carrier tracking performance, with a general phase process input, may readily be simulated in the time domain using the Hughes developed SYSTID simulation language. The SYSTID input consists of a topological (block diagram) description of the system in terms of existing (or especially created) SYSTID elements. The SYSTID compiler then generates the required FORTRAN digital simulation program and executes it.

4.4.2 Simulation Parameter Assumptions

The simulated second order carrier tracking loop incorporates an active loop filter of the form

$$F(S) = \frac{1 + \tau_2 S}{\tau_1 S}$$

which permits tracking a constant doppler acceleration. The time constants τ_1 and τ_2 are determined by specifying loop threshold noise bandwidth, gain, and damping. It is convenient to define the Tausworthe damping parameter by

$$r_o = \frac{G \tau_2^2}{\tau_1}$$

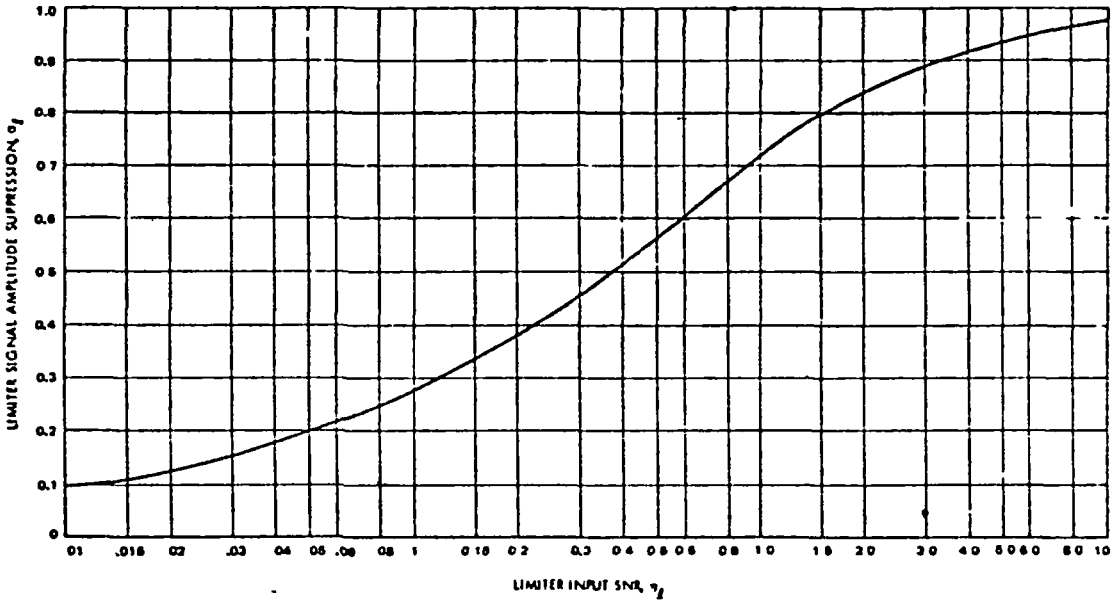


FIGURE 4 9 VARIATION OF α_ℓ WITH LIMITER INPUT SNR, η_ℓ

where G is the total loop gain and the rms input signal is normalized to unity. Loop damping factor is related to r_o by

$$\zeta = 1/2 \sqrt{r_o}$$

It is conventional to define threshold SNR as $\eta_o = 0$ dB in the two-sided threshold loop bandwidth $2 B_{LO}$, where

$$2 B_{LO} = \frac{r_o + 1}{2 r_2}$$

For a loop preceded by a bandpass limiter, effective loop gain (hence, bandwidth) is a function of the limited input SNR. The foregoing expressions, defined at threshold loop SNR, may be generalized if r_o is replaced by

$$r = r_o/\mu$$

where $\mu = \alpha_o/\alpha$ is the ratio of the limited amplitude suppression corresponding to threshold loop SNR ($\eta_o = 0$) to the actual suppression. Limiter amplitude suppression α versus limiter input SNR is plotted in Figure 4-9 (Reference 4-7).

r_o is typically chosen to be two for optimal doppler tracking performance at threshold. This corresponds to critical loop damping ($\zeta = 1/2 \sqrt{2}$) at threshold. Total loop gain is determined by specifying the static phase error (SPE) at the maximum frequency tracking offset

$$G = \frac{\Delta\omega}{SPE}$$

The maximum SPE has been somewhat arbitrarily chosen to be 0.1 radian (5.7°) at the maximum frequency offset of 20 kHz in order that the nominal loop operating point be well within the linear region. The resulting loop gain is 1.25×10^7. The threshold loop bandwidth ($2 B_{LO}$) was chosen to assure prompt initial acquisition. The acquisition SNR (in $2 B_{LO}$) is

$$\eta_{oA} = \eta_{oW} + \Delta_{space} + \Delta_{fade}$$

where

η_{oW} (= 10 dB) is the assumed worst case SNR in $2 B_{LO}$

Δ_{space} (= 1.24 dB) is the differential space loss between the worst case and initial acquisition transmission paths

Δ_{fade} (= 3.62 dB) is the one percent fade margin (Section 3)

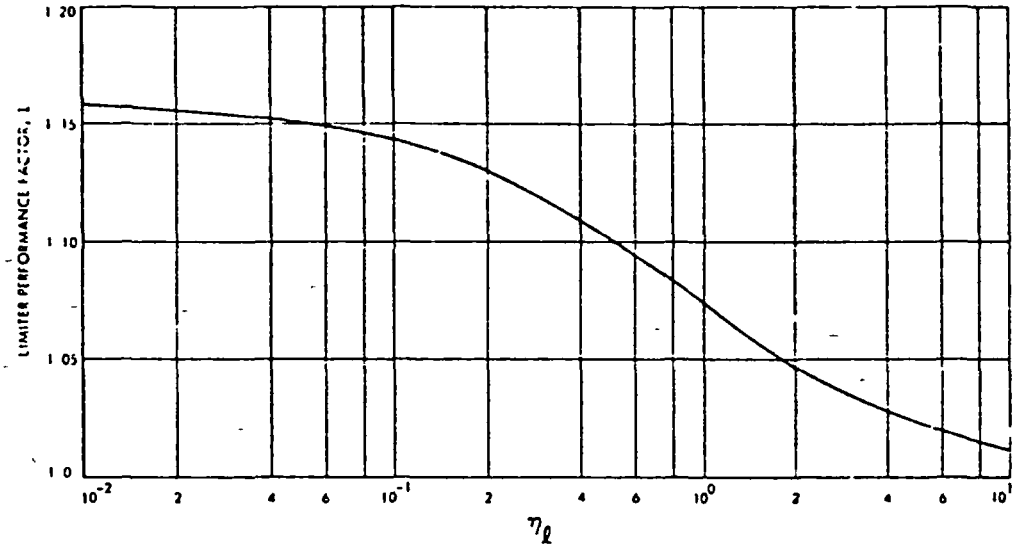


FIGURE 4 10 VARIATION OF THE PARAMETER Γ WITH LIMITER INPUT SNR, η_ℓ

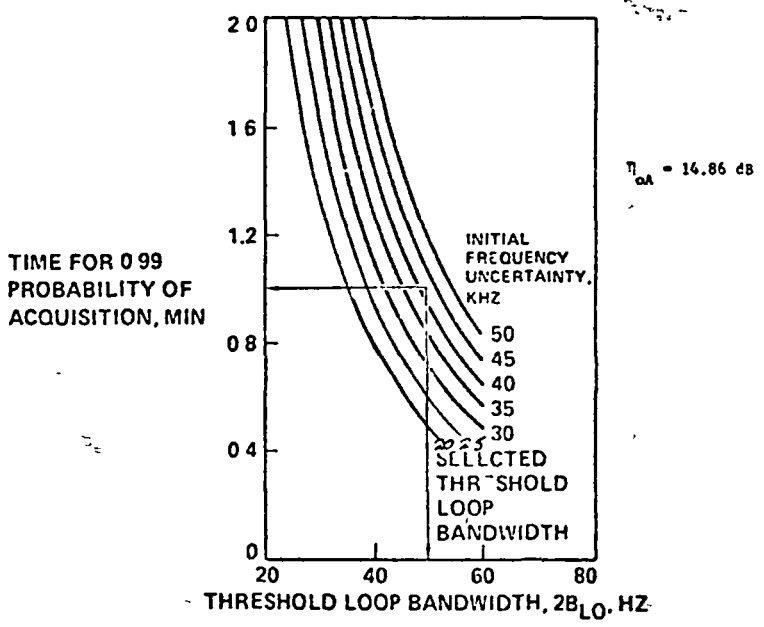


FIGURE 4-11 ACQUISITION TIME

Acquisition time calculations assume an initial frequency uncertainty of 20 kHz (half the 40 kHz doppler range). The frequency sweep rate for 0.90 probability of acquisition of an encountered signal is given by (Reference 4-8)

$$\dot{f} = \frac{(1 - \eta^{-1/2})\,(r_o/\mu)}{2\pi\,\tau_2^2}$$

where η is the SNR in B_L, the actual one-sided loop bandwidth. η is given by

$$\eta = \eta_o \left(\frac{2\,B_{LO}}{B_L}\right) \frac{1}{\Gamma}$$

where

η_o is the loop SNR referred to $2\,B_{LO}$

$$B_L \approx B_{LO} \left(\frac{1 + r_o/\mu}{1 + r_o}\right)$$

$1/\Gamma$ is the limiter suppression

The limiter suppression is approximated (for limiter bandwidth, $B_\ell > 10\,B_L$) by

$$\frac{1}{\Gamma} \approx \frac{0.862 + \eta_\ell}{1 + \eta_\ell}$$

(Figure 4-10) (Reference 4-9) where η is the limiter input SNR, given by $\eta_\ell = (2\,B_{LO}/B_\ell)\,\eta_o$ where B_ℓ, the limiter bandwidth was chosen to be 50 kHz. Figure 4-11 depicts acquisition time (for $P_A \geq 0.99$) versus $2\,B_{LO}$ with frequency uncertainty range as a parameter. For a $\eta_o = 14.86$ dB and $\Delta f = 20$ kHz, Figure 4-11 indicates acquisition in approximately 0.5 minute for $2\,B_{LO} = 50$ Hz. This $2\,B_{LO}$ value was chosen for the simulation as a compromise between acquisition performance and transmitted power requirements. With $\eta_{oA} = 14.86$ dB (30.62) in $2\,B_{LO}$ (= 50 Hz), $\eta = 11.23$ dB (13.26) in an actual loop bandwidth $B_L = 100$ Hz. Similarly, at the assumed minimum operating $\eta_o = 10$ dB, $\eta = 8.50$ dB (7.08) in an actual loop bandwidth $B_L = 61$ Hz

4.4.3 Simulation Input Characterization

The receiver simulation input is the low-pass equivalent of the actual received signal. The low-pass equivalent consists of the doppler and scintillation modulation of the transmitted carrier, corrupted by additive white

gaussian noise Due to the disparity in time scale between the doppler and scintillation phase processes, a key assumption has been made in the representation of scintillation in order to reduce computer run time. The period of the maximum doppler excursion (±20 kHz) is 5×10^{-5} seconds. Within each 360° period of the tracked doppler signal, the simulated instantaneous system time response must be calculated at sufficiently small phase intervals to permit approximation of the continuous system time response function. The period of the assumed maximum doppler frequency is 5×10^{-5} seconds (1/20 kHz). By contrast, the time scale of the scintillation (as characterized by its reciprocal spectral bandwidth) is many orders of magnitude greater. In order to observe a statistically meaningful number of scintillation samples, simulation for many multiples of the scintillation time scale would be required. This would be economically prohibitive. An equivalent alternative is based upon the following considerations. Scintillation affects doppler measurements both by its effect on receiver phase tracking and by introducing a pseudo-doppler component to the input phase process. Since the time scale of the scintillation is long, compared to reasonable doppler measurement (averaging) periods (0.01 to 1.0 second), the phase scintillation rate and acceleration components remain essentially constant over a single measurement period. The worst case (to a specified statistical confidence level) scintillation effect may then be approximated by assuming that the corresponding adverse scintillation induced phase rate and acceleration prevail over a single doppler measurement interval. The input phase process thus perturbed represents a worst case for both tracking performance and pseudo-doppler contribution.

Over a single doppler sample period, the low frequency equivalent input phase process may be represented by

$$\theta = ft + 1/2\, \dot{f}\, t^2$$

In turn

$$f = D + x\sigma_{\dot{\theta}}$$

and

$$\dot{f} = \dot{D} + x\sigma_{\ddot{\theta}}$$

where

D = doppler frequency shift

$\dot{D}$ = doppler rate

$\sigma_{\dot{\theta}}$ = standard deviation of $d\phi/dt$

$\sigma_{\ddot{\theta}}$ = standard deviation of $d^2\phi/dt^2$

x = desired confidence level determined so that the input scintillation components will not be exceeded with a probability of 0.99. (For a gaussian distribution of x = 2.33)

In addition to the doppler and scintillation phase contributions, the simulation input may include step increases in phase, representing possible electronically despun antenna phase transitions.

Similar assumptions were made in the representation of amplitude scintillation contributions. These result in a time dependent input signal increase during the simulation period from the assumed worst case of η_o = 10 dB. This effect accounts for the improved phase tracking noted in the 1 0 Hz bandwidth scintillation simulation results (Figure 4-17). The effect of amplitude fading rate is relatively insignificant however.

4.4.4 Simulation Verification

The carrier tracking loop simulation has been verified by comparison with key theoretical performance predictions (Reference 4-10). Tracking a constant doppler offset ($\Delta\omega$) in the absence of noise results in the theoretically predicted static phase error corresponding to input gain and frequency offset

$$SPE = \frac{\Delta\omega}{G}$$

Tracking a constant doppler rate ($\dot{\omega}$) in the absence of noise results in the theoretically predicted true phase error

$$\theta = \frac{\tau_1 \dot{\omega}}{G}$$

Tracking a zero frequency offset with white gaussian noise input to the bandpass limiter results in a true phase error distribution having the theoretically predicted variance

$$\sigma_\theta^2 \triangleq 1/\eta$$

where η by definition is the SNR in B_L.

4.4.5 Carrier Tracking Simulation Results

The objective of the receiver simulation is to determine the doppler error due to receiver tracking limitations in the PJOP scintillation and doppler environment. The fundamental output of the simulation is the instantaneous true phase error defined by

$$\theta(t) = \theta(t) - \hat{\theta}(t)$$

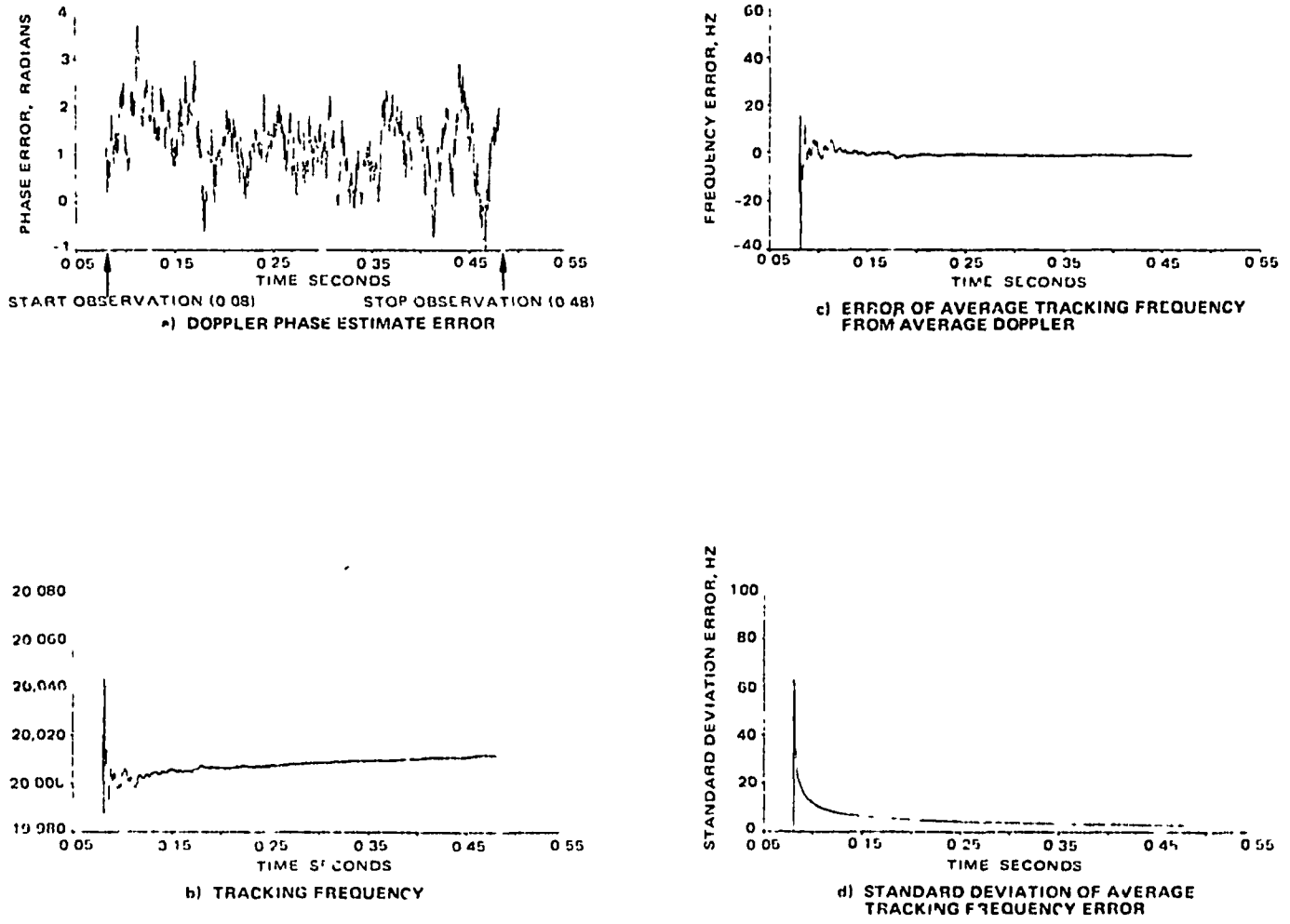


FIGURE 4 12 RECEIVER DOPPLER TRACKING SIMULATION RESULTS WITH NO SCINTILLATION, 40 Hz/SEC DOPPLER RATE, AND 20 KHz FREQUENCY OFFSET SIGNAL/NOISE - 10 DB IN 2 B_{LO} (50 Hz)

where

$\theta(t)$ = doppler phase component of the low pass equivalent receiver input signal.

$\hat{\theta}(t)$ = receiver carrier tracking loop estimate of the total low-pass equivalent input phase (which includes pseudo-doppler due to phase scintillation as well as actual doppler). The instantaneous doppler frequency estimate is

$$\hat{D} = \frac{d\hat{\theta}}{dt}$$

The mean doppler estimate over the measurement period is given by

$$\hat{\overline{D}} = \frac{1}{T}\int_{o}^{T} d\hat{\theta}$$

$$\hat{\overline{D}} = \hat{\theta}/T$$

The mean doppler estimate results from measurement of the received frequency estimate for interval T by an ideal counter/resolver.

Neglecting higher order terms (for $1/2\ \ddot{D}\ t^2 \ldots << D_o$) the instantaneous input doppler is

$$D = D_o + \dot{D}\ t$$

so that the mean input doppler over the measurement period T is

$$\overline{D} = D_o + \dot{D}\ (T/2)$$

The instantaneous error of the receiver doppler estimate is

$$\delta = \hat{D} - D$$

The doppler estimate error includes the pseudo-doppler error introduced by worst case phase scintillation.

The receiver tracking simulation results are summarized in Figures 4-12 through 4-17 for the assumed 50 Hz ($2\ B_{LO}$) loop with a 20 kHz frequency tracking offset and a 40 Hz/sec doppler rate. Figures 4-12 and 4-13 summarize tracking performance with no scintillation input Figure 4-12a illustrates instantaneous loop phase estimate error (from actual doppler phase) versus time over an observation period of 0.40 second. Figure 4-12b

depicts the average loop tracking frequency as a function of time over the same period. Figure 4-12c plots the error of this average tracking frequency from the actual average doppler frequency as a function of time during the 0.4 second observation period. Figure 4-12d shows the standard deviation of the error of the average tracking frequency from the doppler frequency as a function of time during the observation period. Figure 4-13a and 4-13b depict the distributions of doppler phase estimate error and average tracking frequency error, respectively from the simulation. It may be noted from Figure 4-13a that the mean phase error (0.104) is approximately equal to the theoretically predicted value ($\phi = \tau_1\dot{\omega}/G$) for tracking a constant 40 Hz/sec doppler rate in the absence of noise. Similarly, the standard deviation of phase error (0.331) corresponds closely to the theoretical value ($\sigma_\phi = \eta^{-1/2}$) for η_0 = 10 dB in 2 B_{LO} (50 Hz) with the assumed loop parameters. The expressions for ϕ and $\sigma\phi^2$ are strictly valid only for zero frequency offset, in which case agreement with the simulated results is much closer. Similar results are illustrated in Figures 4-14 and 4-15 for 0.10 Hz bandwidth scintillation and in Figures 4-16 and 4-17 for 1.0 Hz bandwidth scintillation. The 1.0 Hz bandwidth scintillation assumed in Figures 4-16 and 4-17 is very conservative based on present expectations and represents an extreme worst case.

Comparison of the true phase error distribution for 1.0 Hz scintillation bandwidth (Figure 4-17a), with that for 0.10 Hz (Figure 4-15a) or no scintillation (Figure 4-13a), shows that the standard deviation is smaller for 1.0 Hz. This results from progressively increased loop SNR and correspondingly improved phase tracking due to amplitude scintillation over the 0.4 second simulation period. Loop SNR increases because the initial SNR corresponds to an assumed worst case 10 dB in 2 B_{LO}. Despite this improved phase tracking performance, the doppler estimate error is significantly greater for the 1.0 Hz scintillation due to the increased pseudo-doppler contribution.

Over a typical measurement period of 0.10 second, the simulation indicates receiver doppler measurement errors of 2.3 Hz for 0.10 Hz scintillation and 8.6 Hz for 1.0 Hz scintillation, compared to a typical 1.8 Hz with no scintillation. The assumed loop SNR on which these results are based represents a practical minimum for acceptable operation. For higher loop SNR, doppler measurement accuracy in the presence of expected scintillation (i.e., bandwidth ≈ 0.10 Hz) would be enhanced due to the improved phase tracking performance.

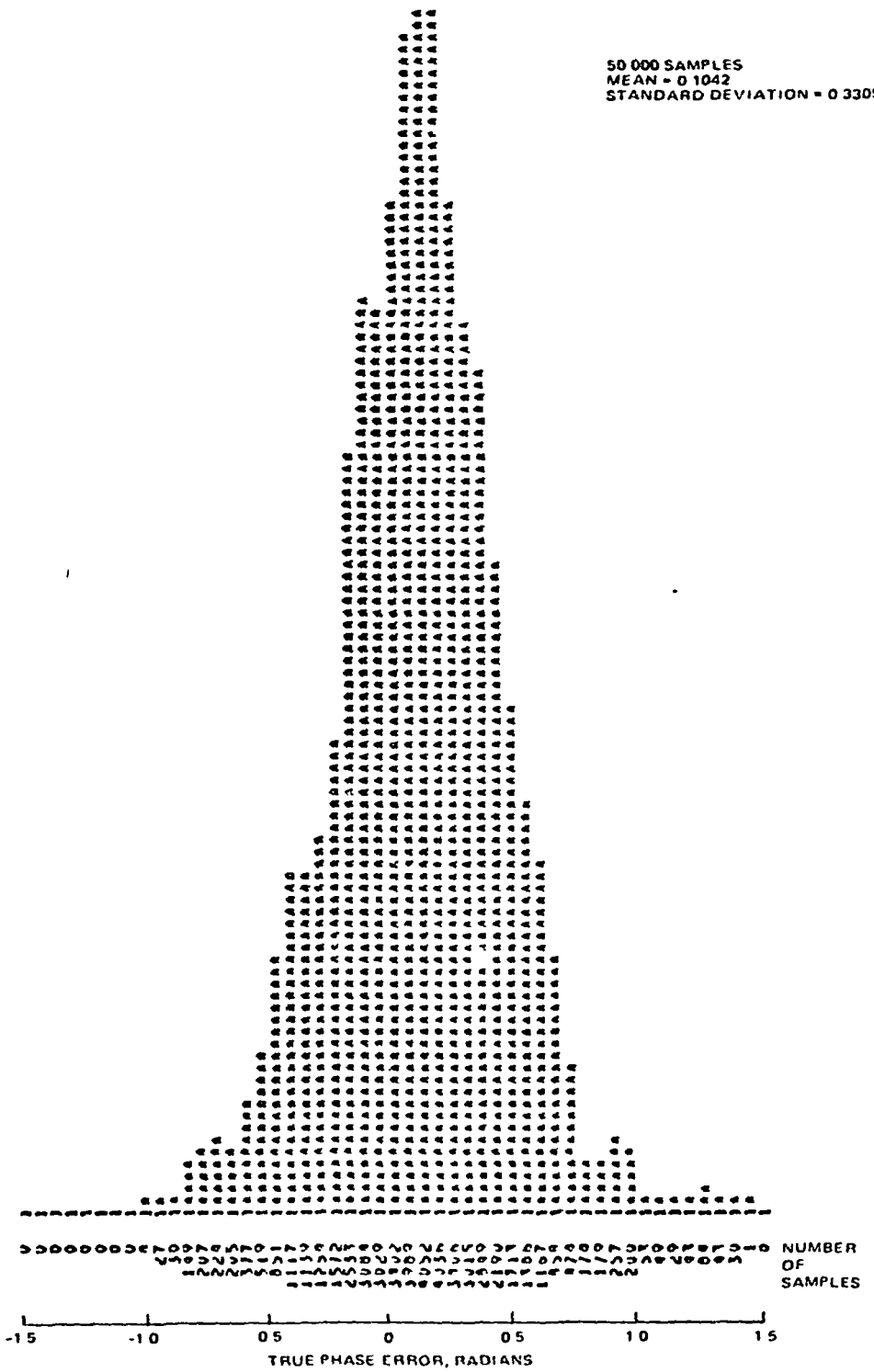


FIGURE 413a DISTRIBUTION OF TRUE PHASE ERROR DURING 0 4 SECOND OBSERVATION WITH NO SCINTILLATION, 40 Hz/SEC DOPPLER RATE, AND 20 kHz FREQUENCY OFFSET SIGNAL/ NOISE = 10 dB IN 2 B_{LO} (50 Hz)

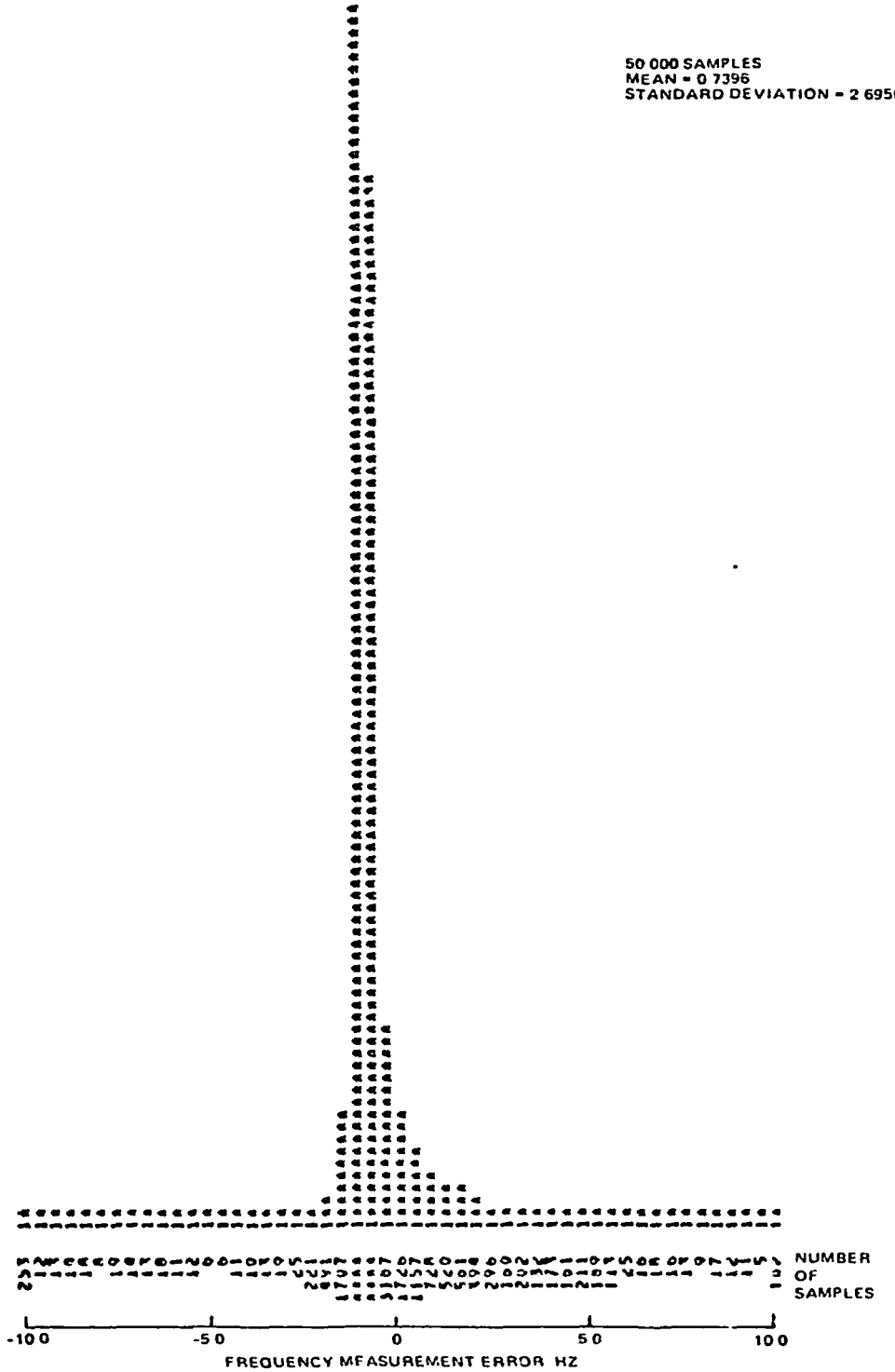
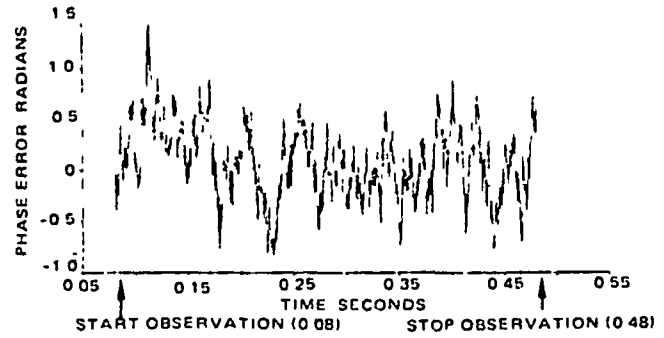
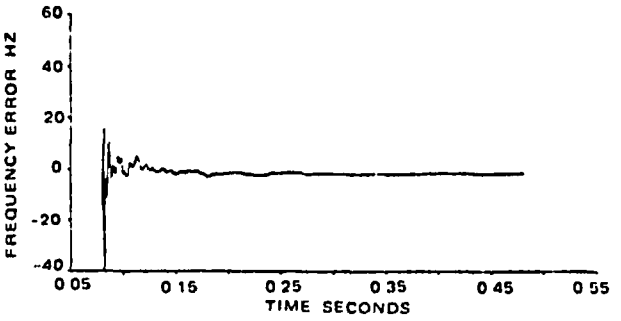


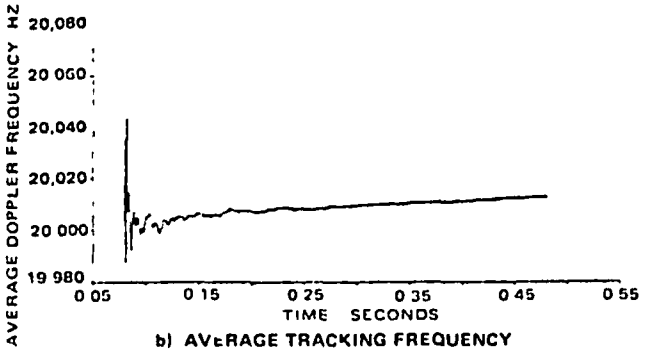
FIGURE 4 13b DISTRIBUTIONS OF DOPPLER MEASUREMENT ERROR DURING 0 4 SECOND OBSERVATION WITH NO SCINTILLATION, 40 Hz/SEC DOPPLER RATE, AND 20 kHz FREQUENCY OFFSET. SIGNAL/NOISE = 10 dB IN 2 B_{LO} (50 Hz)



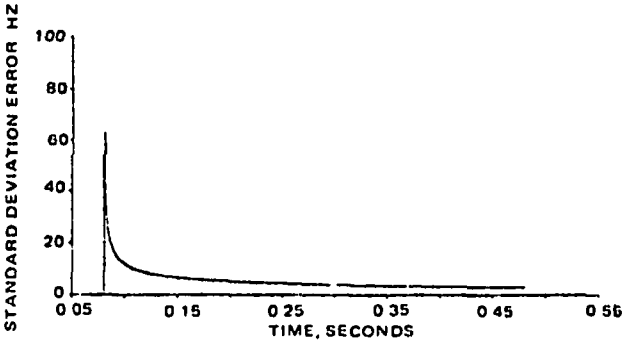
a) DOPPLER PHASE ESTIMATE ERROR



c) ERROR OF AVERAGE TRACKING FREQUENCY FROM AVERAGE DOPPLER



b) AVERAGE TRACKING FREQUENCY



d) STANDARD DEVIATION OF AVERAGE TRACKING FREQUENCY ERROR

FIGURE 4 14 RECEIVER DOPPLER TRACKING SIMULATION RESULTS WITH 0 10 Hz BANDWIDTH SCINTILLATION, 40 Hz/SEC DOPPLER RATE, and 20 KHz FREQUENCY OFFSET SIGNAL/NOISE = 10 DB IN 2 B_{LO} (50 Hz)

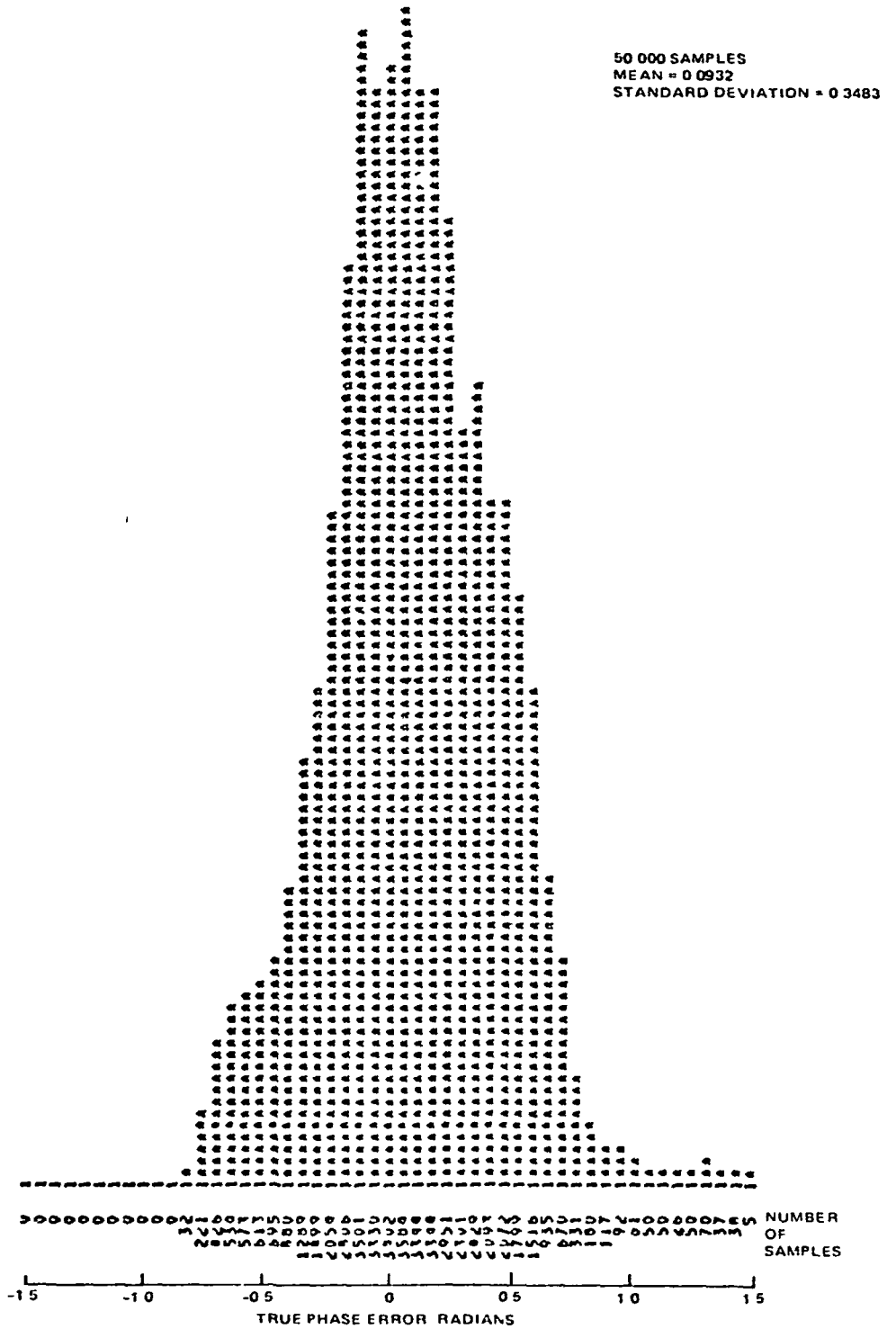


FIGURE 4 15a DISTRIBUTION OF TRUE PHASE ERROR DURING 0 4 SECOND OBSERVATION WITH 0 10 Hz BANDWIDTH SCINTILLATION, 40 Hz/SEC DOPPLER RATE, AND 20 kHz FREQUENCY OFFSET SIGNAL/NOISE = 10 dB IN 2 B_{LO} (50 Hz)

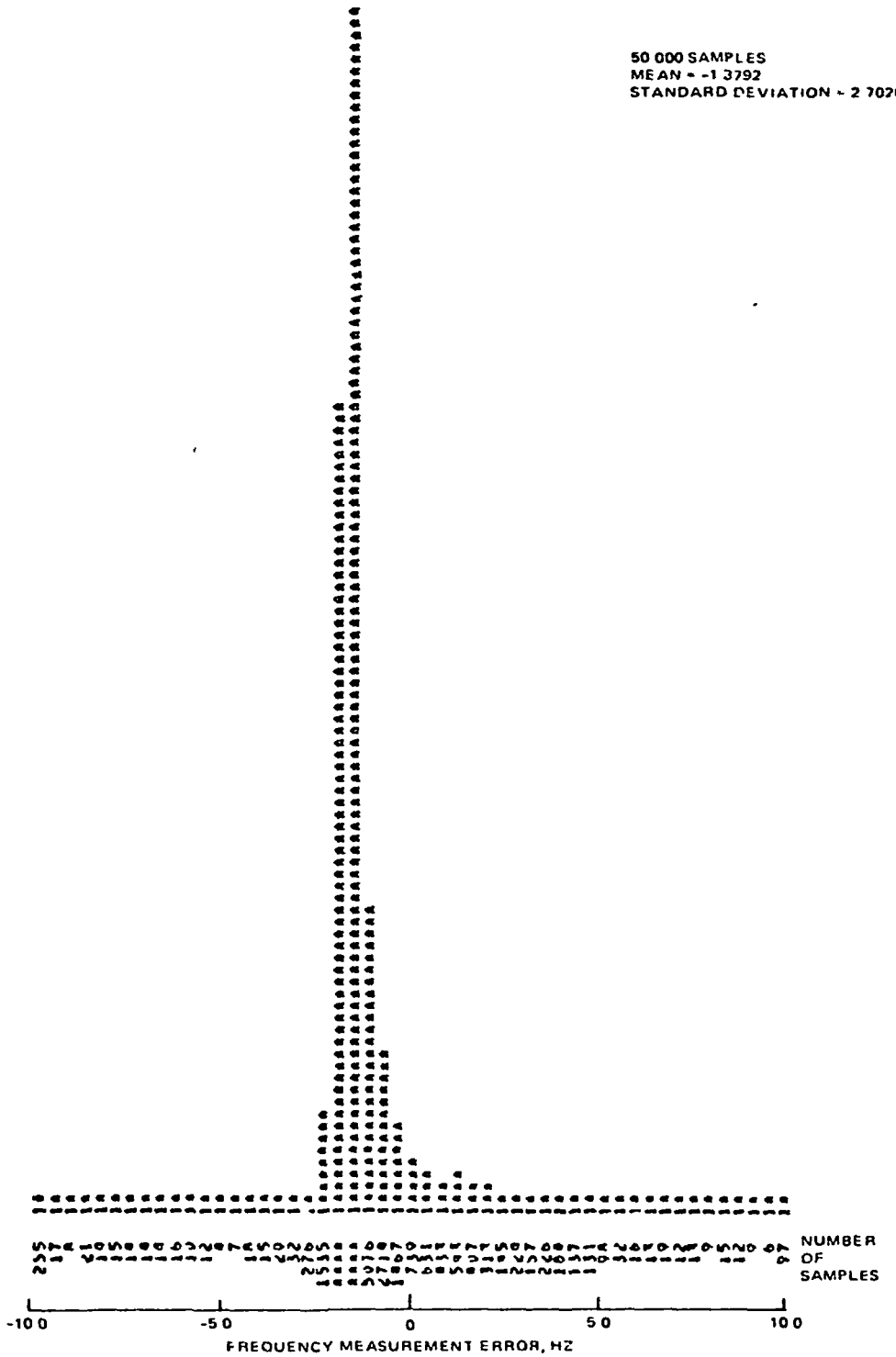
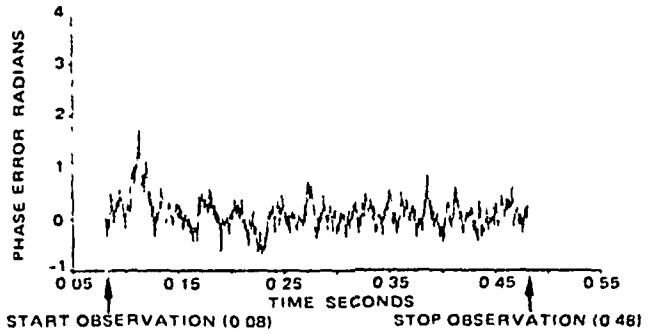
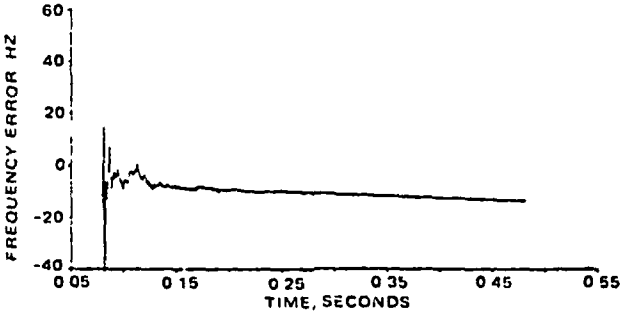


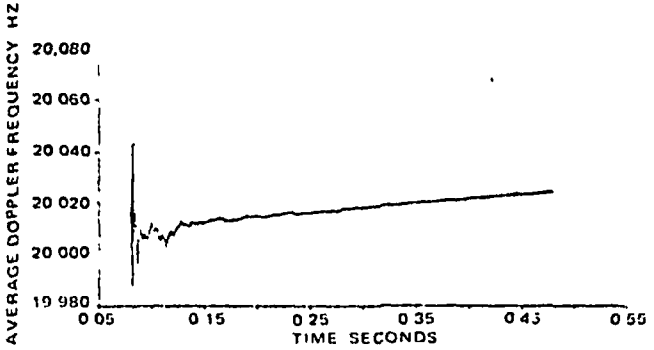
FIGURE 4 15b DISTRIBUTIONS OF DOPPLER MEASUREMENT ERROR DURING 0 4 SECOND OBSERVATION WITH 0 10 Hz BANDWIDTH SCINTILLATION, 40 Hz/SEC DOPPLER RATE, AND 20 kHz FREQUENCY OFFSET SIGNAL/NOISE = 10 dB IN 2 B_{LO} (50 Hz)



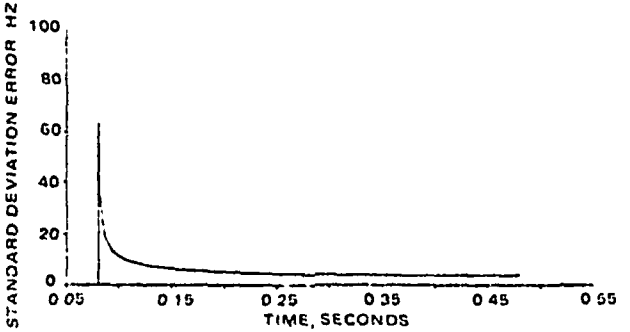
a) DOPPLER PHASE ESTIMATE ERROR



c) ERROR OF AVERAGE TRACKING FREQUENCY FROM AVERAGE DOPPLER



b) AVERAGE TRACKING FREQUENCY



d) STANDARD DEVIATION OF AVERAGE TRACKING FREQUENCY ERROR

FIGURE 4 16 RECEIVER CARRIER TRACKING SIMULATION RESULTS FOR 1 0 Hz BANDWIDTH SCINTILLATION, 40 Hz/SEC DOPPLER RATE, AND 20 KHz FREQUENCY OFFSET SIGNAL/NOISE = 10 DB in 2 B_{LO} (50 Hz)

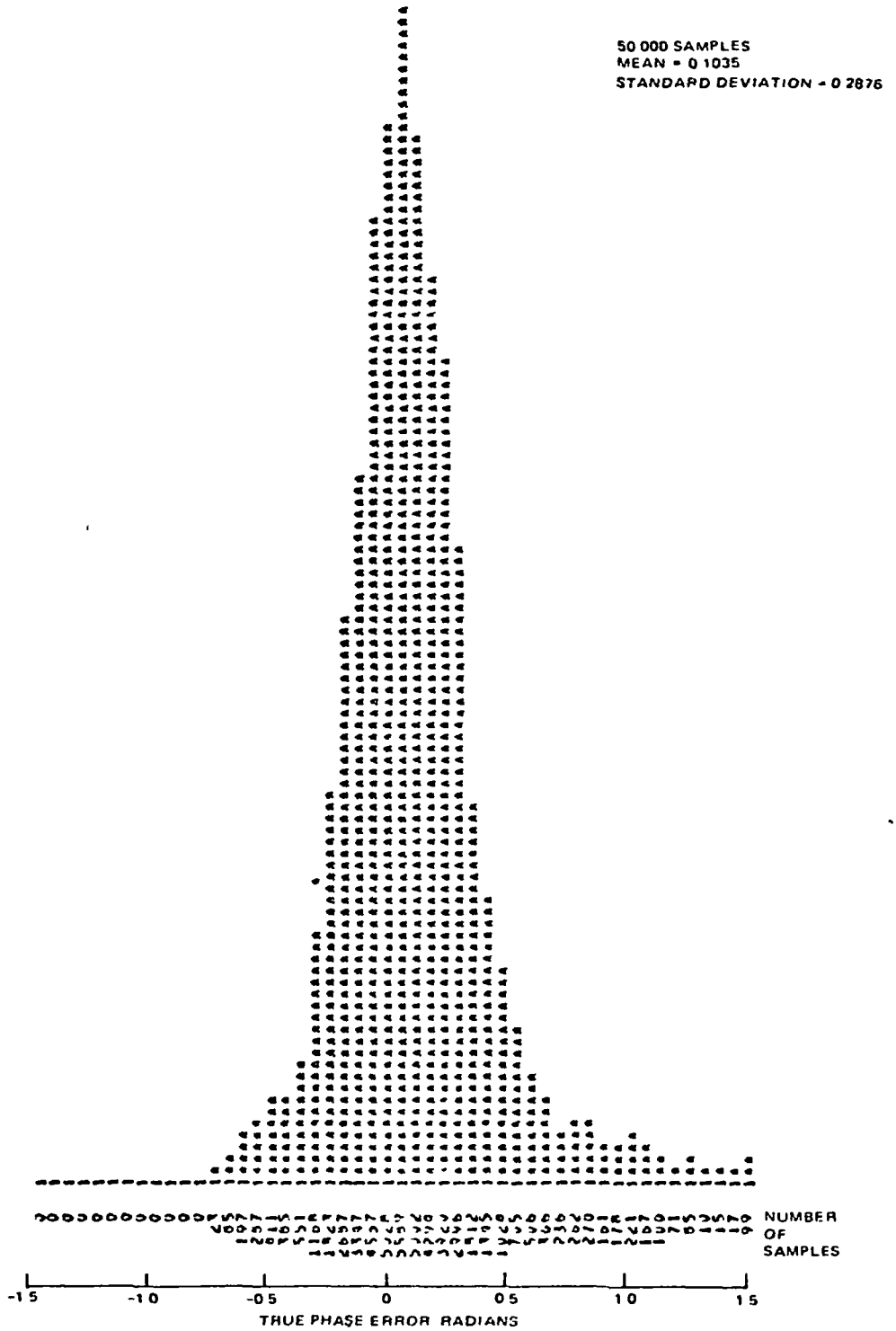


FIGURE 4 17a DISTRIBUTION OF TRUE PHASE ERROR DURING 0 4 SECOND OBSERVATION WITH 1 0 Hz BANDWIDTH SCINTILLATION, 40 Hz/SEC DOPPLER RATE, AND 20 kHz FREQUENCY OFFSET SIGNAL/NOISE = 10 dB IN 2 B_{LO} (50 Hz)

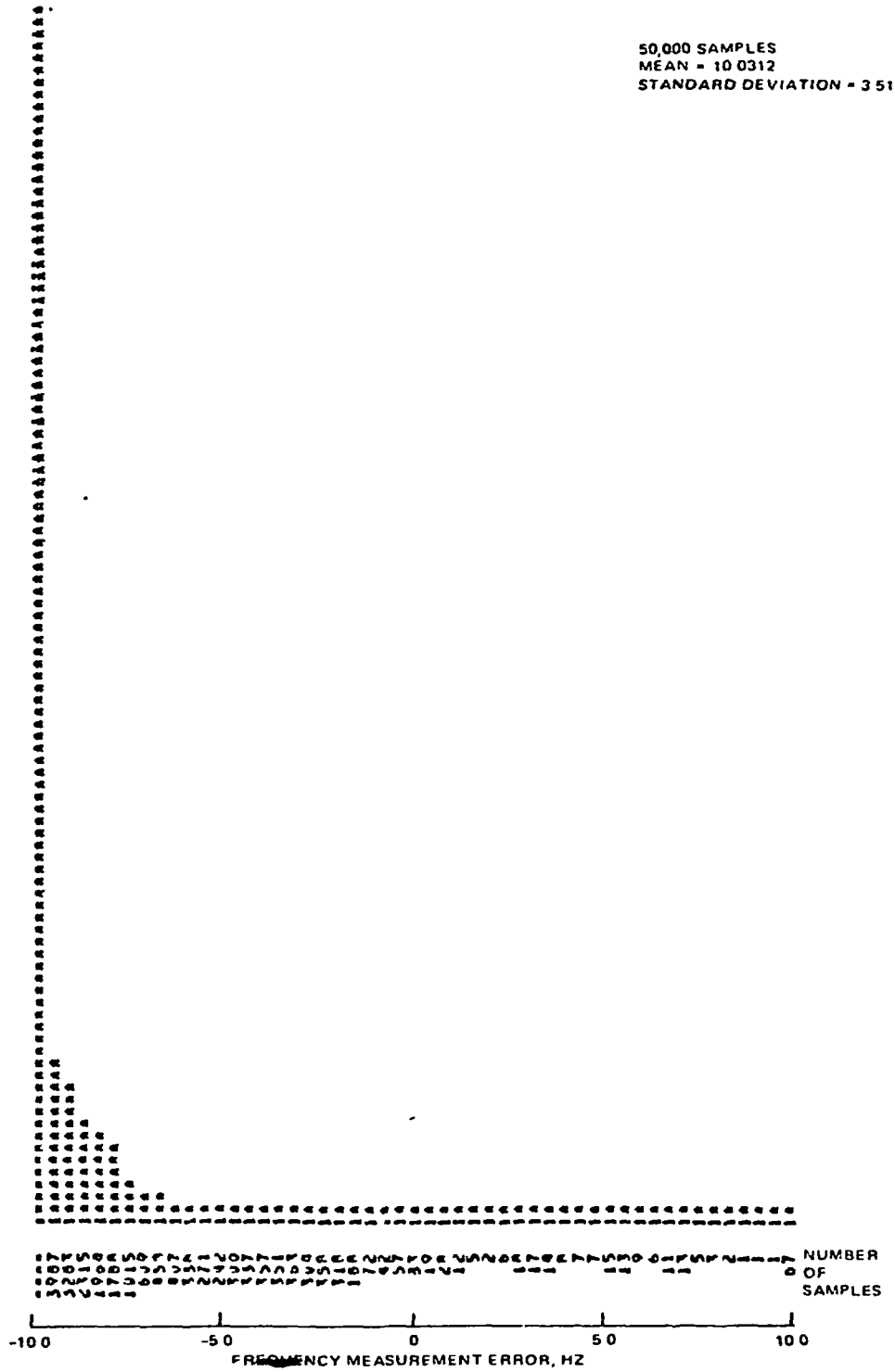


FIGURE 4-17b DISTRIBUTIONS OF DOPPLER MEASUREMENT ERROR DURING 0 4 SECOND OBSERVATION WITH 1 0 Hz BANDWIDTH SCINTILLATION, 40 Hz/SEC DOPPLER RATE, AND 20 kHz FREQUENCY OFFSET SIGNAL/NOISE = 10 dB IN 2 B_{LO} (50 Hz)

4.5 DOPPLER EXTRACTOR CONFIGURATION

The doppler extractor generates the counter/resolver input from the receiver carrier frequency estimate. A postulated doppler extractor for the heterodyne carrier tracking receiver is depicted schematically in Figure 4-18. Assume that receiver frequency tracking is perfect (frequency lock), then (Figure 4-18)

$$f_2 = f_x$$

where f_x is derived from the free running local oscillator and f_2 is the second IF. However, f_2 is determined by

$$f_2 = Nf_x - f_1$$

where f_1 is the first IF. See Figure 4-7. Since

$$f_1 = f_{REC} - f_{VCO}$$

at the first mixer output, the voltage controlled oscillator frequency is given by

$$f_{VCO} = f_{REC} - (N - 1) f_x$$

in terms of the received frequency, f_{REC}. The doppler IF is derived by combining f_{VCO} with the local reference frequency, f_{REF}

$$f_3 = f_{VCO} - f_{REF}$$

so that

$$f_3 = f_{REC} - (N - 1) f_x - f_{REF}$$

By adding f_3 to

$$f_4 = f_{BIAS} + (N - 1) f_x$$

the doppler extractor output frequency

$$f_{XTR} = f_{REC} - f_{REF} + f_{BIAS}$$

is obtained. Thus, by the proper choice of f_4, the doppler extractor output is made independent of the free running local oscillator. The accuracy with which the received frequency may be inferred from measurement of the extractor output frequency is limited by the accuracy with which f_{REF} and f_{BIAS} are known (still assuming frequency lock). These are both derived by multiplication of the transponder auxiliary oscillator frequency (nominally 19.1 MHz) which may be calibrated against DSN ground frequency standards via the spacecraft-earth downlink. The calibration accuracy is expected to be of the order of $\Delta f/f = 10^{-11}$. This approaches the limitation imposed by the auxiliary oscillator short term stability.

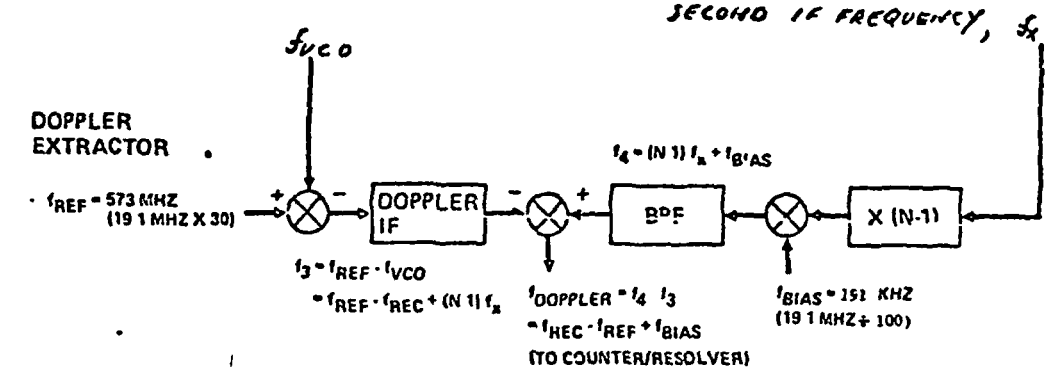
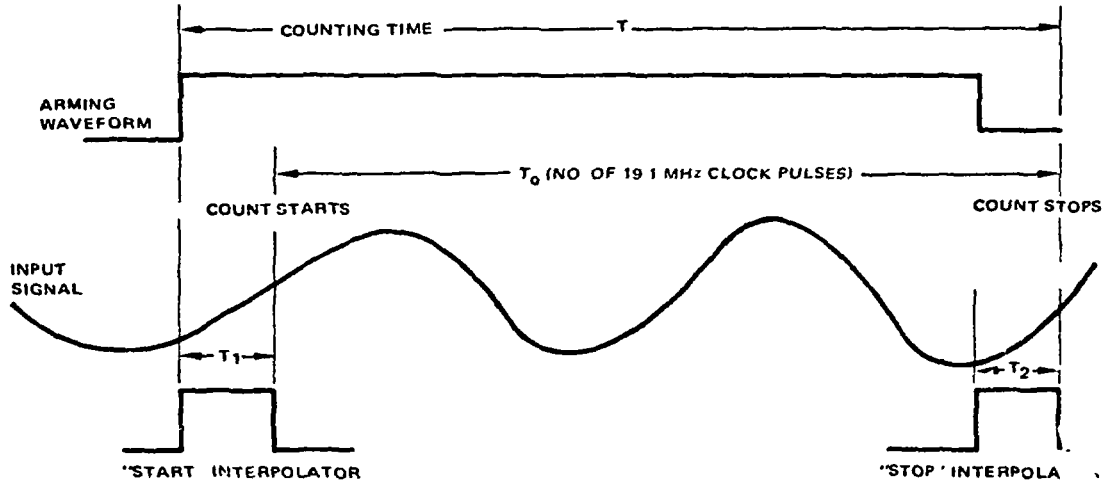


FIGURE 4-18 DOPPLER EXTRACTOR SCHEMATIC DIAGRAM



REAL INTERPOLATION TIME T_1 MAY BE EXPANDED BY A PULSE STRETCHING FACTOR (e g , 10^3) SO THAT $T_1' = S \times T_1$ T_1 MAY BE MEASURED BY THE NUMBER OF 19 1 MHz CLOCK PULSES THAT OCCUR IN T_1'. WITH ACCURACY CORRESPONDING TO A CLOCK FREQUENCY S x 19 1 MHz

FIGURE 4-19. COUNTER/RESOLVER OPERATION

The nominal carrier frequency (f_{REC}) is chosen equal to the local reference frequency. With perfect frequency tracking and no propagation effects (phase scintillation), the doppler frequency is given by

$$f_{doppler} = f_{REC} - f_{REF}$$

The actual extractor output frequency is, in fact, biased by f_{BIAS} for two reasons:

1) It is desirable that the counter/resolver input frequency always be positive to avoid directional ambiguity.

2) There is an optimal value of the input frequency for best counter/resolver measurement accuracy. The ideal resolver performance is improved as the counter frequency is reduced (with respect to the constant clock frequency). However, trigger error in both the counter and resolver functions degrades performance if the counted frequency is too low. Optimization of the counted frequency is beyond the scope of the present effort. It will be shown (subsection 4.6) that a counted frequency of 150 to 200 kHz (corresponding to the chosen 191 kHz bias and the predicted range of PJOP doppler shift) provides an acceptably small trigger error.

4.6 COUNTER/RESOLVER LIMITATIONS

The counter/resolver determines the doppler extractor output frequency by measuring total phase change over a measurement time interval. Operation of the counter/resolver is indicated schematically in Figure 4-19. The counter measures the number of positive zero crossings between the start and stop count signals. The resolver determines the fractional phase between the start and stop count signals and their respective next zero crossings. That is, the measurement time interval consists of

$$T = T_0 + T_1 - T_2$$

where

T_0 = time corresponding to the number of clock pulses occurring in the measurement time interval

T_1 = time interval between the start count signal and the first clock pulse

T_2 = time interval between the stop count signal and the next clock pulse

Times T_1 and T_2 are measured by analog interpolation. T_0 and T_2 may be measured directly by the clock frequency or with increased accuracy by pulse stretching. Using pulse stretching, the actual T_1 and T_2 are expended (stretched) by a precisely known factor. The stretched times,

T_1' and T_2', may then be determined with correspondingly increased resolution (for a given clock frequency), and the actual T_1 and T_2 inferred from them. Pulse stretching may be effectively implemented by charging a capacitor at constant current during T, then discharging it at a reduced constant current over stretched time T'. Pulse stretching reduces the clock count ambiguity (±1 clock count) by the inverse of the stretch factor.

Total counter/resolver error consists of resolver error, trigger error, and time base error.

Resolver error is the relative phase error in measurement of the fractional cycles occurring during T_1 and T_2. The resolver time resolution with pulse stretching is

$$\Delta t = T_C/S$$

where

T_C = period of the time base (clock frequency)

S = pulse stretching factor

For a measured frequency of period T_E, Δt represents a phase error of

$$\Delta\phi = \frac{T_C}{ST_E} \text{ cycle}$$

Using the transponder auxiliary oscillator frequency (19.1 MHz) as a time base and the nominal 191 kHz doppler extractor output, the phase error is

$$\Delta\phi = \frac{191 \times 10^3}{19.1 \times 10^6} = \frac{0.01}{S} \text{cycle}$$

Over a typical measurement period of T = 0.05 second, the resultant relative phase error is

$$\frac{\Delta\phi}{\phi} = \frac{0.01}{S}\,\frac{T_E}{T} = \frac{0.01}{S\,(0.05)\,(191 \times 10^3)} \approx 1.05 \times 10^{-6}/S$$

Assuming a perfect time base, the nominal 191 kHz extractor output could be measured to a frequency uncertainty of

$$\Delta f = (1.05 \times 10^{-6})\,(191 \times 10^3)/S$$

$$\Delta f = 0.20 \text{ Hz}/S$$

Readily achievable pulse stretching of S = 1000 would reduce Δf to 0.20×10^{-3} Hz.

Trigger error is due to 1) trigger input circuit error and 2) noise error. Typical input circuit error may be estimated in terms of input signal slope. Consider an approximately 200 kHz trigger circuit input signal to have an rms value of 100 mV. The maximum slope is then

$$m = \omega E_o = 4\pi\sqrt{2} \times 10^4 = 1.77 \times 10^5 \text{ volts/sec}$$

For triggering at the point of maximum slope the mean input trigger circuit error over a measurement period of T is

$$\bar{e}_1 = \frac{2e_1}{T}$$

where e_1 is the input trigger circuit time error at each end point. From Figure 4-20 (Reference 4-11), $e_1 \approx 4 \times 10^{-9}$ seconds. For T = 0.05 second

$$\bar{e}_1 = 1.6 \times 10^{-7}$$

Noise error for a sinusoidal input may be inferred from Figure 4-21 (Reference 4-11) which depicts worst case single measurement error, e_2, versus counter input voltage SNR. The mean noise error is then

$$\bar{e}_2 = \frac{e_2}{\sqrt{T}}$$

For SNR = 30 dB ($e_2 = 1 \times 10^{-2}$) and a 0.05 second observation time, the mean 191 kHz measurement error is

$$\bar{e}_2 = 1 \times 10^{-6}$$

The total trigger error in this instance is

$$e = \bar{e}_1 + \bar{e}_2 = 1.2 \times 10^{-6}$$

In conclusions, counter/resolver error in measuring the doppler extractor output may be reduced to a relatively negligible contribution using existing methods. Using existing integrated circuit components, it has been estimated (Reference 4-12) that the associated counter/resolver weight would be less than 1 pound with a power consumption of less than 1 watt.

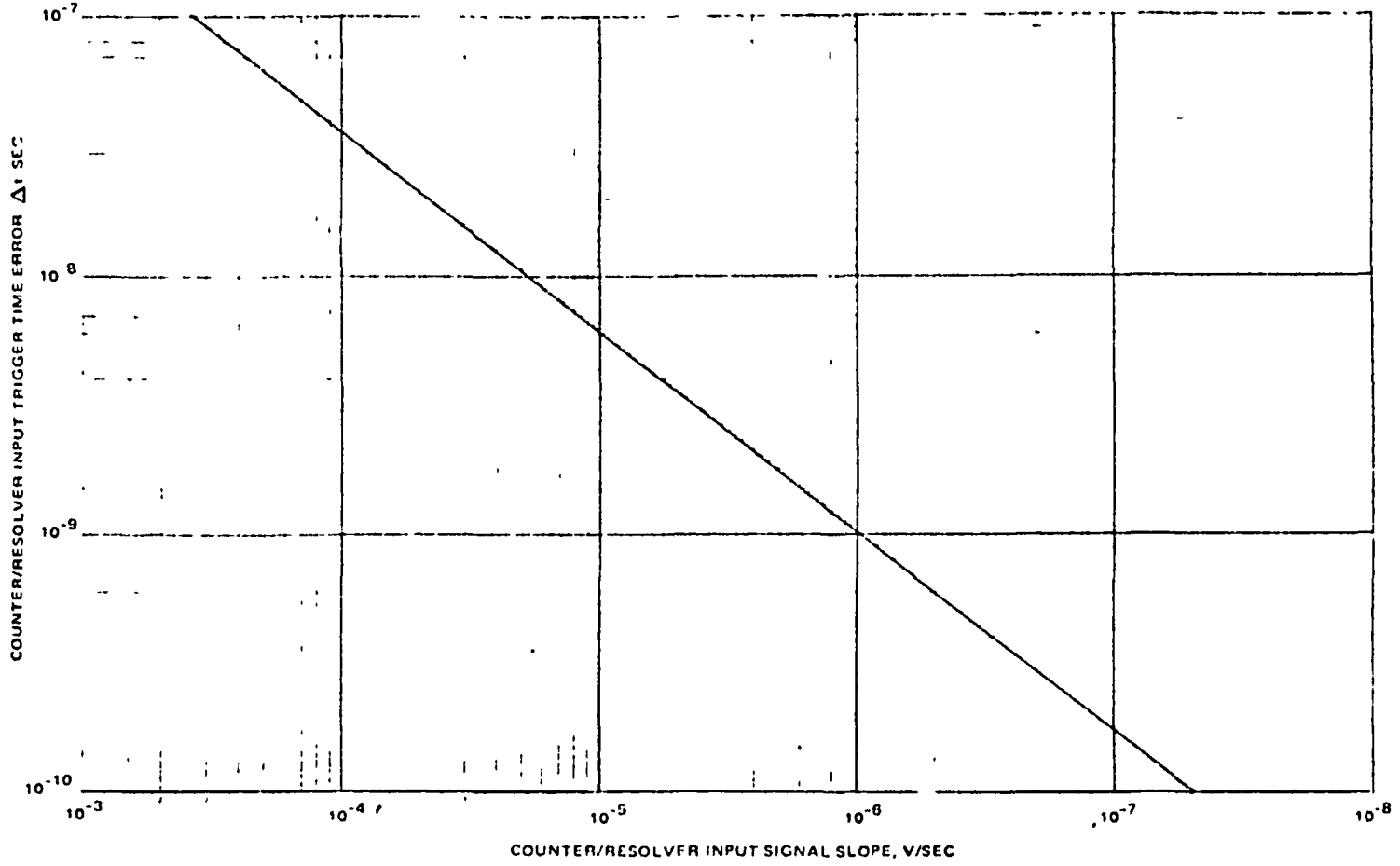


FIGURE 4 20 COUNTER/RESOLVER INPUT TRIGGER TIME ERROR VERSUS INPUT SIGNAL SLOPE

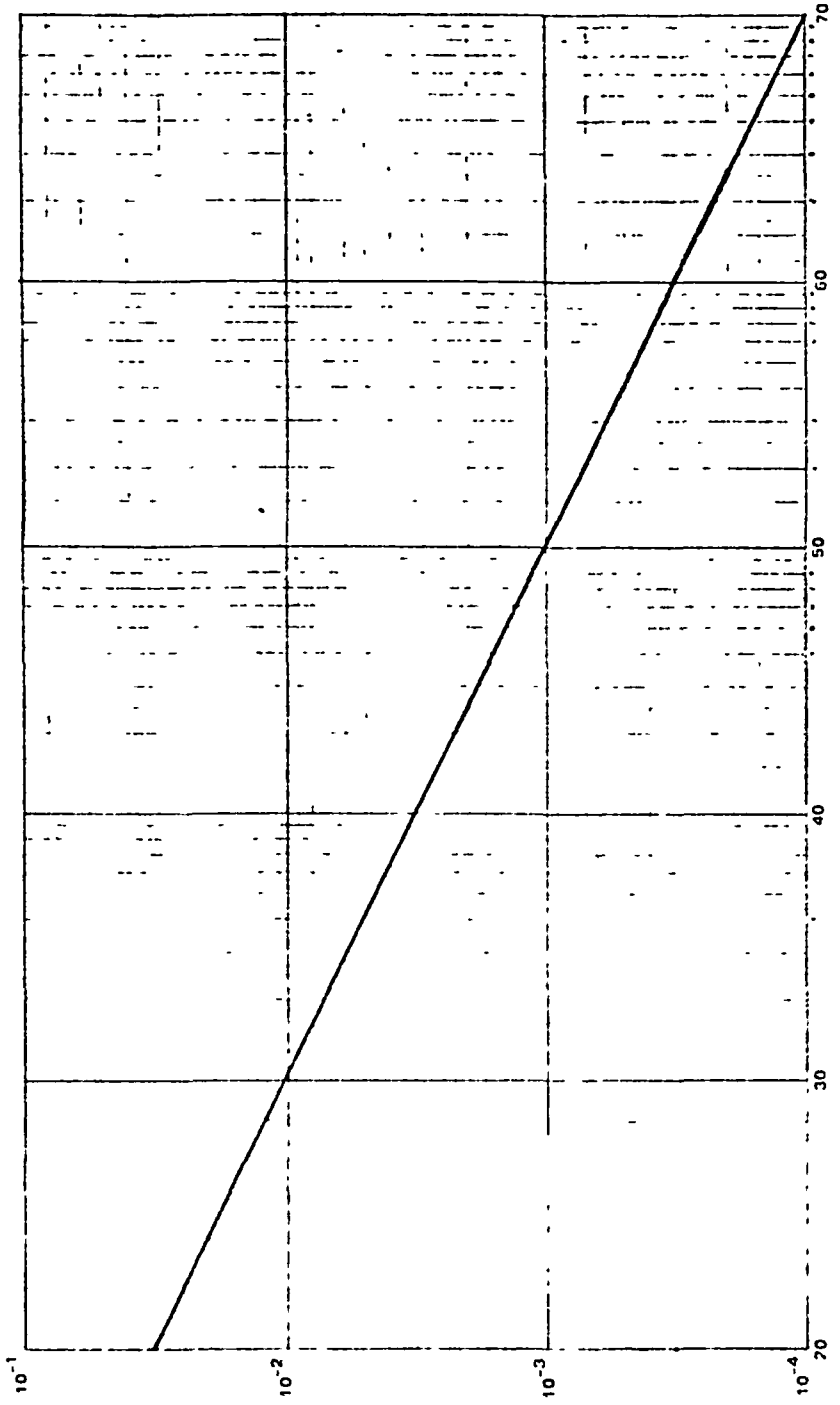


FIGURE 4 21 COUNTER/RESOLVER TIME ERROR VERSUS SINUSOIDAL INPUT SIGNAL SNR

4.7 SUMMARY AND CONCLUSIONS

The major sources of one-way PJOP doppler measurement error during the preentry communication phase are uncertainty in the probe transmitted frequency and the limitations in receiver frequency tracking performance due to noise and scintillation. Doppler extractor and counter/resolver error contributions may be made relatively negligible if the spacecraft transponder auxiliary oscillator, calibrated against the DSN ground reference, is used as an onboard time reference. A suitably designed state of the art quartz probe oscillator can provide transmitted frequency knowledge to within 1.2 to 6 Hz (at 600 MHz) depending on allowable warmup energy. Frequency tracking performance of a postulated phase-lock loop receiver in the anticipated PJOP doppler and scintillation environment has been investigated by means of a computer simulation using the Hughes developed SYSTID time domain simulation language. The results confirm that when the scintillation bandwidth is small compared to the receiver carrier tracking loop bandwidth, the effect of scintillation on received phase tracking is negligible. The direct effect of scintillation on the measurement of probe doppler measurement error by introducing a pseudo-doppler or phase-rate contribution may be significant, depending on magnitude of that contribution and the relative length of the measurement period. For this study, a carrier tracking loop SNR corresponding to 10 dB in 2 B_{LO} = 50 Hz was assumed. A typical measurement interval of 0.10 second was employed for which the simulated receiver doppler estimate error is approximately 2.3 and 8.6 Hz for the 0.10 Hz scintillation bandwidths respectively, compared to 1.8 Hz with no scintillation.

4.8 REFERENCES

4-1) Bartholomew, C.A., "Atomic Oscillators for Space Systems," EASCON 1974.

4-2) Bloch, Martin (Frequency Electronics, Inc.), Telecon, March 1976.

4-3) Dyer, J. and Cowley, J., "Assessment of Capability for Determining Frequency of a Stable Transmitter at Turn-On 15 Minutes Before Entry Into Venus' Atmosphere," NASA Ames Research Center.

4-4) Woo, R. and Yang, F., "Scintillation Estimates for a Jupiter Entry Probe - Phase I," Jet Propulsion Laboratory, 18 July 1975.

4-5) Woo, R., Kendall, W., Ishimaru, A., and Berwin, R., "Effects of Turbulence in the Atmosphere of Venus on Pioneer Venus Radio - Phase I," Jet Propulsion Laboratory Memorandum 33-644, 30 June 1973.

4-6) Viterbi, A. J., Principles of Coherent Communication, McGraw-Hill, New York, 1966, p. 39.

4-7) Edelson, R., Telecommunication Systems Design Techniques Handbook, JPL Technical Memorandum 33-571, Jet Propulsion Laboratory, 15 July 1975.

4-8) Gardner, F.M., Phaselock Techniques, John Wiley & Sons, New York, 1966, p. 49.

4-9) Tausworthe, R.C., "Information Processing: Limiters to Phase-Locked Loops: A Correction to Previous Theory," Jet Propulsion Laboratory, Space Programs Summary 37-54, Volume III, 31 December 1968, pp. 201-204.

4-10) Tausworthe, R.C., Theory and Practical Design of Phase-Locked Receivers, Vol 1, Jet Propulsion Laboratory, Technical Report No. 32-819, 15 February 1966.

4-11) Hewlett-Packard Company, Computing Counter 5360A Operating Manual, Santa Clara, California, October 1969.

4-12) Smith, J.R., Personal Communication, Jet Propulsion Laboratory, January 1976.

5. ELECTRONICALLY DESPUN ANTENNA

Communication performance and/or capacity in the probe-to-orbiter link can be enhanced, beyond that achievable with an axisymmetric antenna, by using an electronically despun antenna (EDA). This spinning antenna electronically phases the component elements such that the field pattern is focused into a receiving beam pointed towards the probe. For this task, the EDA concept was to be developed for the Ames Research Center, Pioneer Jupiter Orbiter baseline spacecraft concept of the fall of 1975.

Specific requirements were: 1) an operating frequency of 400 MHz, 2) a minimum beamwidth of 50°, and 3) a minimum gain over the beamwidth of 7 dB. General design goals were to minimize the impact on the orbiter, minimize weight, and provide high reliability.

The EDA configuration selected consists of 12 quadrifilar helical elements evenly spaced angularly around a 137 cm diameter mounting ring. The desired field pattern is achieved by activating and properly phasing five of these elements at a time, turning all elements on and off once per orbiter revolution. The estimated mass for the entire EDA including electronics is 7.5 kg. Field pattern analysis indicates that a peak gain of 13 dB is possible and that a gain greater than 10 dB for the majority of the probe mission can be accomplished.

This section discusses the array element characteristics, the array factor computations, and the electronics implementation. Results of gain pattern computations are presented and discussed and the effect of the number of active elements is shown. Computation of the phase change at element switchings are also given.

In conjunction with this study, a methodology and computational capability was developed for generating conceptual EDA designs and optimizing them with respect to given constraints and requirements. Thus, although the concept briefly summarized above operates at 400 MHz and is configured for a particular spinning spacecraft, the approach to EDA design developed for this task can be readily applied to a different set of conditions and constraints to develop an optimum design.

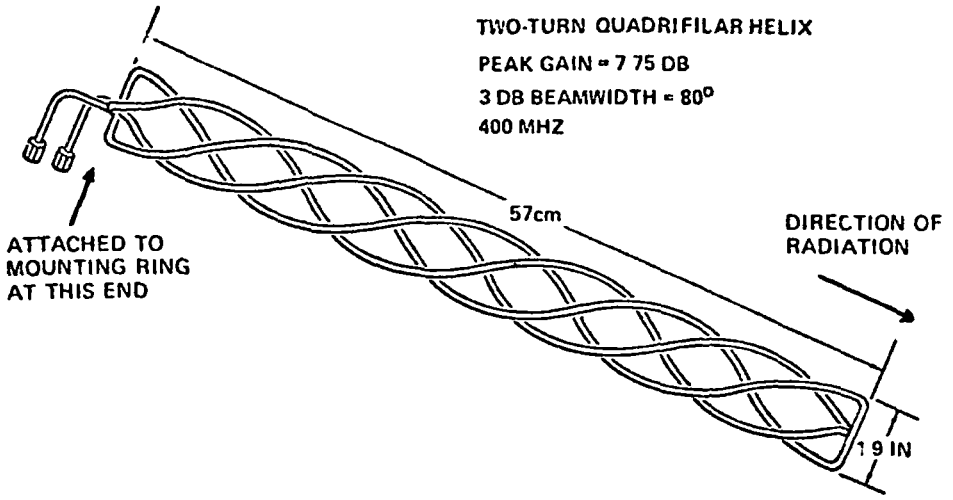


FIGURE 5 1. EDA ELEMENT

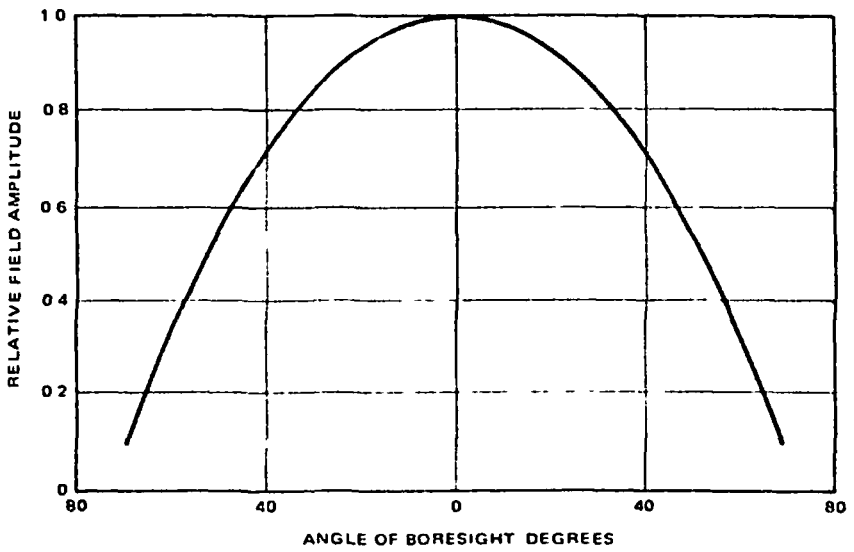


FIGURE 5 2 RELATIVE FIELD PATTERN OF TWO TURN QUADRIFILAR HELIX SHOWN IN FIGURE 5 1

5.1 ARRAY ELEMENT

5.1.1 Design

Analysis of the trajectory geometry and its effect on the probe communication link indicates that the 3 dB beamwidth of the orbiter antenna should lie in the range 50° to 70°. This beamwidth requirement applies to the plane containing the spin axis and the probe. For this study, an element beamwidth of 80° was chosen to include the above range with additional coverage to compensate for any asymmetry in the EDA radiation pattern caused by the array factor and multiple scattering from the structure. This beamwidth requirement can be realized by a quadrifilar helix which is known to be capable of providing conical beams with a beamwidth that can be controlled over a wide range. Thus a two-turn quadrifilar helix appears to be a reasonable choice for the EDA elements. Figure 5-1 illustrates the element design.

A quadrifilar helix is in essence a four-element helical antenna. It can also be described as two orthogonal bifilars fed in phase quadrature where a bifilar is a two-element helical antenna. Electrically, this type of radiator provides efficient endfire radiation with high front-to-back ratio, and excellent circular polarization over a broad angular region. Mechanically, it is simple and lends itself to a lightweight design that can withstand launch and space environment. In this particular design, the feeding of the antenna is achieved by the infinite balun method which employs a semirigid cable as one of the elements of the bifilar element. At the feed point the center conductor of the coax is soldered to the opposite helical element. The required phase quadrature between the two bifilars is provided by the use of a 3 dB hybrid. To simplify the construction of the antenna, impedance matching will be implemented and integrated with the hybrid.

5.1.2 Radiation Characteristics

The design of the two-turn quadrifilar helix (Figure 5-1) is based on available design curves. However, measured radiation patterns and gain characteristics of this design are not yet attainable. Based on the measured radiation charcateristics of a different design and the assumption that the gain-beamwidth product is constant, the EDA element is estimated to have a 7.75 dB peak gain and a main beam pattern as shown in Figure 5-2.

5.1.3 Construction and Weight

The EDA quadrifilar helix can be constructed with various types of semirigid cable wound on a thin fiberglass tube. The choice of coaxial cable will be made on the basis of rigidity and thermal stability of the antenna element such that it will withstand vibrations during launch and thermal environment in space. Table 5-1 shows an estimated weight of each array element for various choices of cables.

C. C. Kilgus, "Shaped-Conical Radiation Pattern Performance of the Backfire Quadrifilar Helix," IEEE Trans. Antennas and Propagation, Volume AP-23, May 1975, pp. 392-397.

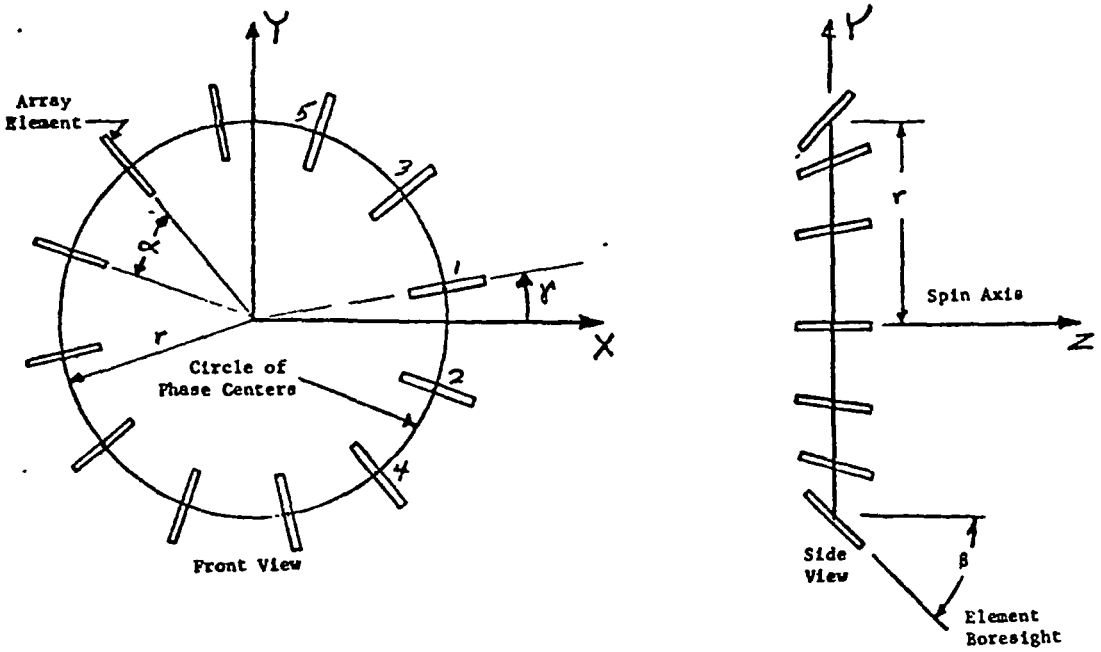


FIGURE 5 3 EDA COORDINATES IN PLANE OF PHASE CENTERS ROTATION ANGLE AND ACTIVE ELEMENTS NUMBERING ARE SHOWN

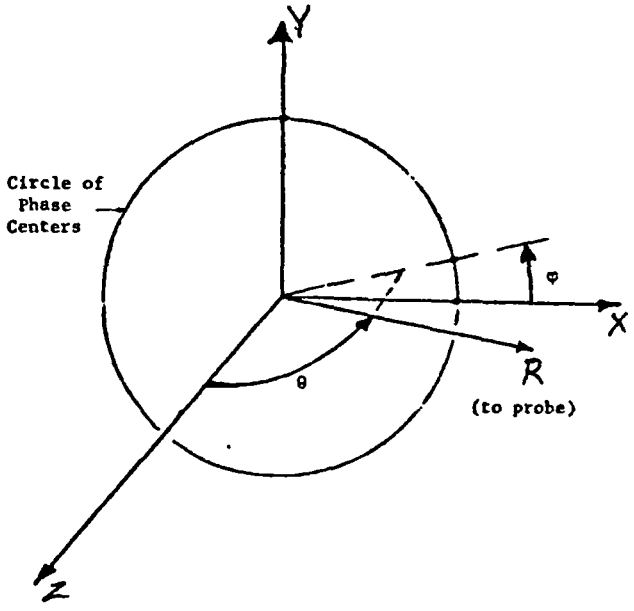


FIGURE 5-4 DEFINITION OF VECTOR TO PROBE IN EDA SPHERICAL COORDINATES

TABLE 5 1 ESTIMATED MASS PER ARRAY ELEMENT OF EDA

Type of Coaxial Cable	Mass of Helical Elements, kg	Weight of Support Tube, kg	Total Mass, kg
0 141 in semirigid (copper,	0 118	0 18	0 298
0 141 in spline (copper)	0 095	0 18	0 275
0 250 in spline (aluminum)	0 095	0 18	0 275

5.2 GENERAL ARRAY ANALYSIS

The EDA consists of m two-turn quadrifilar helices equally spaced and mounted on a circular structure of radius a. In determining the array factor, the distances from the phase centers of each activated element must be computed. A good approximation for the element chosen here is that the phase center is at the midpoint. Now define a coordinate system such that the x-y plane coincides with the plane containing the phase centers and the origin is at the center of the circle containing the phase centers. The array will be assumed to spin in a standard right-hand rule direction about the +z axis. This coordinate system is illustrated in Figure 5-3.

Each element is of length L and the angle between the boresight and the z axis is β (see Figure 5-3). The angular spacing, α, between any two adjacent elements is given simply by

$$\alpha = \frac{360}{m} \text{ degrees} \tag{5-1}$$

The radius, r, of the circle containing the phase centers is given by

$$r = a + \frac{L}{2} \sin \beta \tag{5-2}$$

The activated elements are phased such that the radiated electromagnetic waves have the same phase along a line in the x-z plane which makes an angle of μ with the z-axis. The angle μ is called the squint angle.

One element will always be within an angle of $\pm\alpha/2$ of the x-axis, and the angle between this element and the x-axis is defined as the rotation angle, γ (see Figure 5-3).

A representative observation point, P, is defined in spherical coordinates as shown in Figure 5-4. And it is assumed that the distance, R, to the

observation point is very large compared to the array radius, r. The vector, $\overline{R}$, to the point P is given by

$$\overline{R} = (\overline{x} \sin\theta \cos\varphi + \overline{y} \sin\theta \sin\varphi + \overline{z} \cos\theta) R \qquad (5-3)$$

where

$$R = |\overline{R}|$$

The vector to the phase center of an element is given by

$$\overline{r}_i = r (x \cos \gamma_i + y \sin \gamma_i) \qquad (5-4)$$

where

$$\gamma_i = \gamma + \alpha (-1)^{i+1} \qquad (5-5)$$

Thus, the elements are numbered as shown in Figure 5-3 at any instant of time. The unit vector, $\overline{u}_i$, in the direction of the boresight of an element is given by

$$\overline{u}_i = \overline{x} \cos \gamma_i \sin\beta + \overline{y} \sin\gamma_i \sin\beta + \overline{z} \cos\beta \qquad (5-6)$$

The field intensity, F, at $P(\theta, \varphi)$ is given by

$$F(\theta, \varphi, \gamma) = \sum_{i=1}^{n} A_i \exp[j (k s_i + v_i)] \qquad (5-7)$$

where

$$s_i = |\overline{R} - \overline{r}_i| = \text{distance from element } i \text{ to P} \qquad (5-8)$$

A_i = amplitude of field pattern in the direction of P by element i

v_i = phase of signal at element i

$$k = 2\pi/\lambda = 2\pi f/c \qquad (5-9)$$

n = number of active elements

The components of the field intensity can be referenced to element 1.

$$F = \exp[j (k s_1 + v_1)] \sum_{i=1}^{n} A_i \exp [jk (s_i - s_1) + j(v_i - v_1)] \qquad (5-10)$$

Because $R \gg |\overline{r}_i|$ an approximation with negligible error is

$$s_i \approx (\overline{R} - \overline{r}_i) \cdot \frac{\overline{R}}{R}$$

and so

$$s_1 - s_i \approx (\overline{r}_1 - \overline{r}_i) \cdot \frac{\overline{R}}{R} \tag{5-11}$$

Now

$$\overline{r}_1 - \overline{r}_i = r\left[\overline{x}\,(\cos\gamma_1 - \cos\gamma_i) + \overline{y}\,(\sin\gamma_1 - \sin\gamma_i)\right] \tag{5-12}$$

Thus

$$\begin{aligned} s_i - s_1 &= r\left[\sin\theta\cos\varphi\,(\cos\gamma_1 - \cos\gamma_i) + \sin\theta\sin\varphi\,(\sin\gamma_1 - \sin\gamma_i)\right] \\ &= r\sin\theta\left[\cos(\gamma_1 - \varphi) - \cos(\gamma_i - \varphi)\right] \end{aligned} \tag{5-13}$$

Each element is phased such that along the line in the x-z plane at an angle, μ (squint angle), with respect to the z-axis, the waves radiated from each element are in phase. To produce this phasing set $K(s_1 - s_1) + (v_1 - v_1) = 0$ and substitute $\theta = \mu$ and $\varphi = 0$ in Equation 5-13 for $s_i - s_1$. The result is

$$v_i - v_1 = -kr\sin\mu\,(\cos\gamma_1 - \cos\gamma_i) \tag{5-14}$$

The radiated amplitude intensity A_i is a function of the angle, ψ_i, between the the boresight and $\overline{R}$. From Equations 5-3 and 5-6

$$\cos\psi_i = \overline{u}_i \cdot \frac{\overline{R}}{R} = \sin\beta\sin\theta\cos(\gamma_i - \varphi) + \cos\beta\cos\theta \tag{5-15}$$

The relationship between A_i and ψ_i is shown in Figure 5-2 which can be closely approximated by

$$A_i = \sqrt{G_e}\left[1 - (1.846 \times 10^{-5})\,\psi_i^2\right] = G(\psi_i)\sqrt{G_e} \tag{5-16}$$

where G_e = peak gain of an element.

From Equation 5-10

$$|F| = \left|\sum_{i=1}^{n} A_i \exp\left[jk(s_i - s_1) + j(v_i - v_1)\right]\right| \tag{5-17}$$

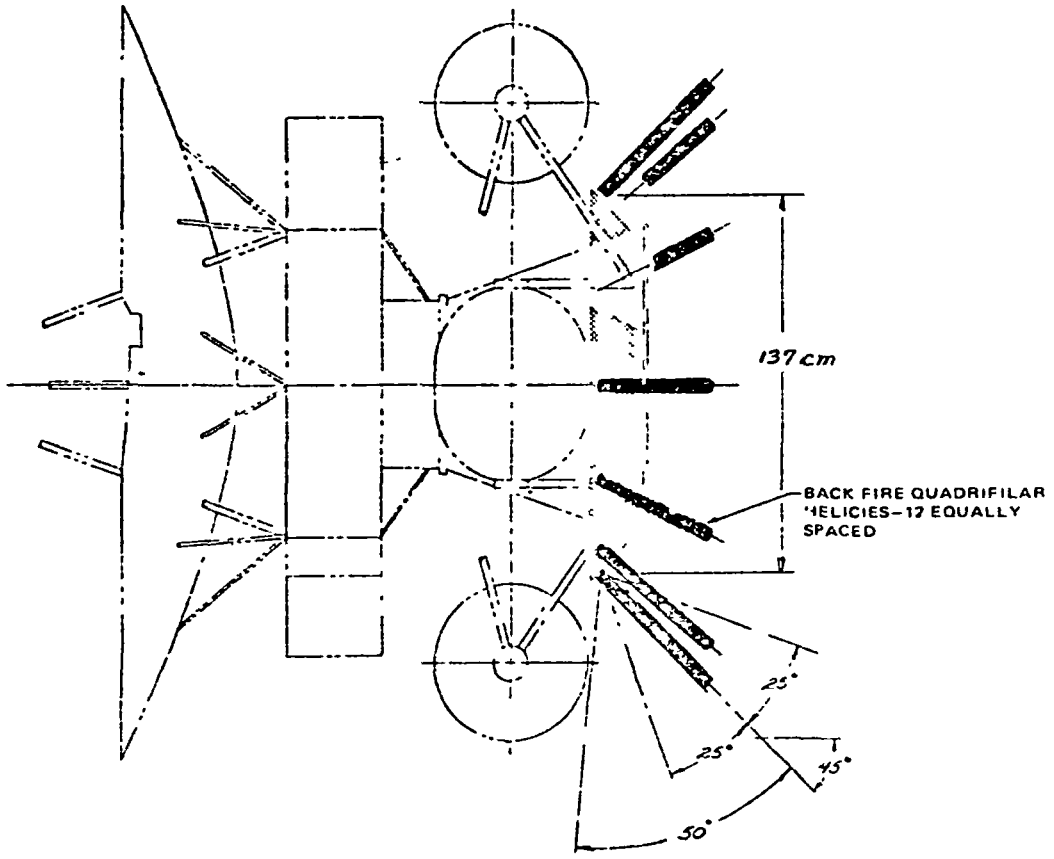


FIGURE 5 5 ELECTRICALLY DESPUN ANTENNA MOUNTED ON PIONEER JUPITER ORBITER

Then

$$|F|^2 = G_e \left| \sum_{i=1}^{n} G(\psi_i) \exp\left[jK (s_i - s_1) + j (\nu_i - \nu_1)\right] \right|^2 \qquad (5\text{-}18)$$

and the array gain is given by

$$G_A = \frac{|F|^2}{n} \qquad (5\text{-}19)$$

5.3 DISCUSSION OF ARRAY PATTERN RESULTS

The previous general analysis leaves all parameters unassigned, and the only constraining assumptions are that the array elements are equally spaced around a circle, with each element boresight lying in a plane containing the perpendicular to the circle through the center (spin axis) and the element phase center. As described previously, in order to obtain numerical results indicating the potential of an EDA, the number of elements chosen was 12. The choice of this number was based on previous experience concerning element spacing and array configuration together with the desire for an even number of elements due to electronics considerations.

The array location and configuration on the spacecraft is shown in Figure 5-5. The diameter of the circle corresponding to the mounting positions is approximately 1.372 meter (54 inches). The length of the elements as shown in Figure 5-1 is 57.15 cm (22.5 inches), thus the radius of the phase center circle as given by Equation 5-2 is

$$r = 0.6858 + 0.2858 \sin\beta \text{ meter}$$

And, for $\beta = 45^\circ$ corresponding to the squint angle selection of Section 2, $r = 0.8879$ meter. With 12 elements, $\alpha = 30^\circ$. The radiation is phased so that in the direction $\theta = 45$, $\varphi = 0$ all signals are in-phase, i.e., $\mu = 45^\circ$. For these parameters, the antenna pattern was computed as a function of the angles, θ, φ, and γ as defined previously and illustrated in Figures 5-3 and 5-4.

For given values of θ, φ, i.e., a fixed probe position, change in γ corresponds to spin motion of the orbiter. Referring to Figure 5-3, it can be seen that the orbiter position of maximum gain depends on the number of active elements, n. If the number is odd, the position of maximum gain corresponds to $\gamma = 0$ and if the number of active elements is even, maximum gain occurs when $\gamma = \alpha/2$. Figures 5-6, 5-7, and 5-8 show the maximum gain as a function of θ and φ for n = 3, 4, and 5, respectively. From these curves the half power beamwidth for $\varphi = 0$ was determined and plotted in Figure 5-9 as a function of the number of active elements. In Section 2, the results of trajectory studies are discussed, and it is shown that for an orbiter periapsis distance of 1.8 R_J, the orbiter antenna beamwidth should be between 55° and 60° in order to maximize overall communication link capability. Thus, from Figure 5-9 it appears that five active elements will give the best performance.

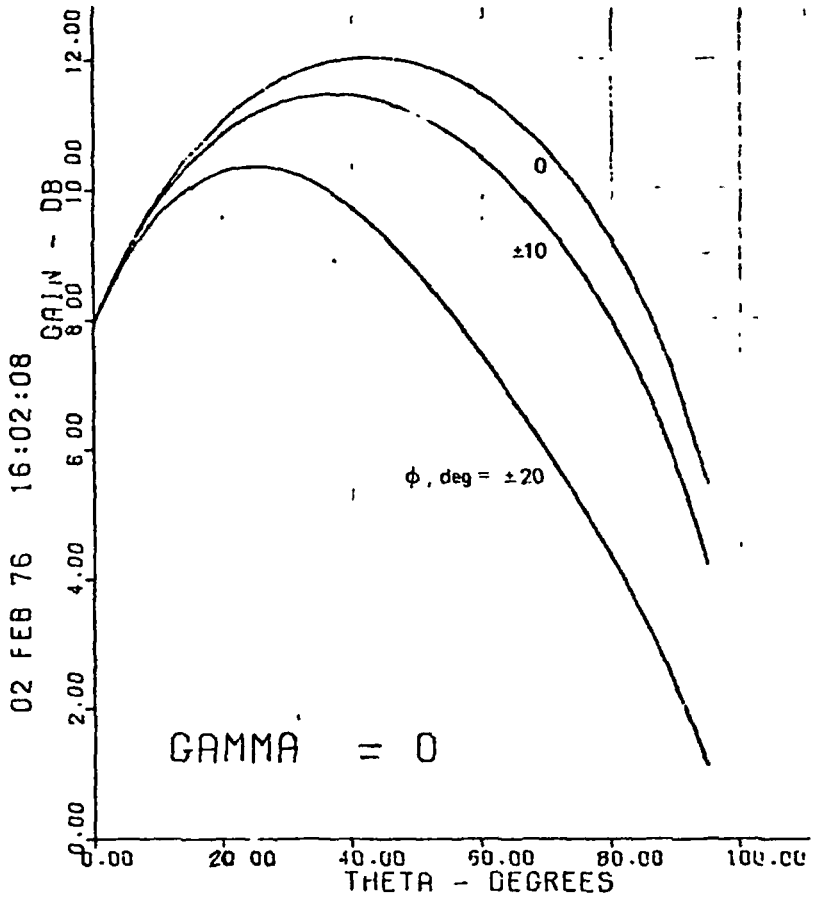


FIGURE 5-6 EDA GAIN VERSUS ASPECT ANGLE FOR THREE ACTIVE ELEMENTS AND γ = 0 DEGREES

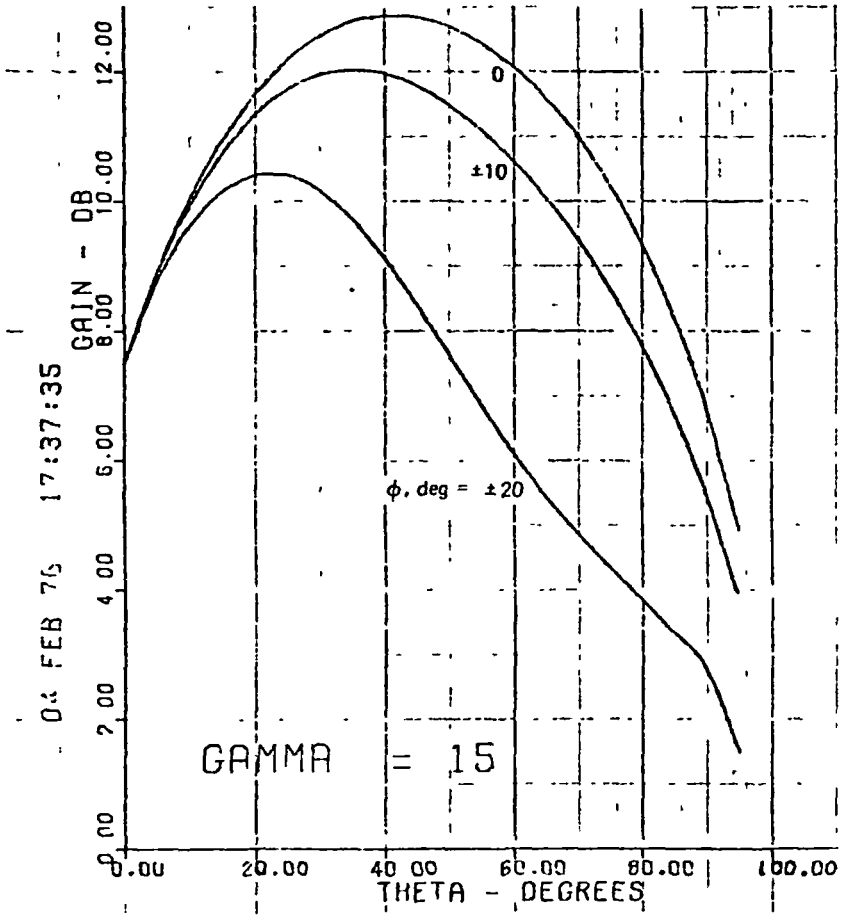


FIGURE 5 7 EDA GAIN VERSUS ASPECT ANGLE FOR FOUR ACTIVE ELEMENTS AND Y = 15 DEGREES

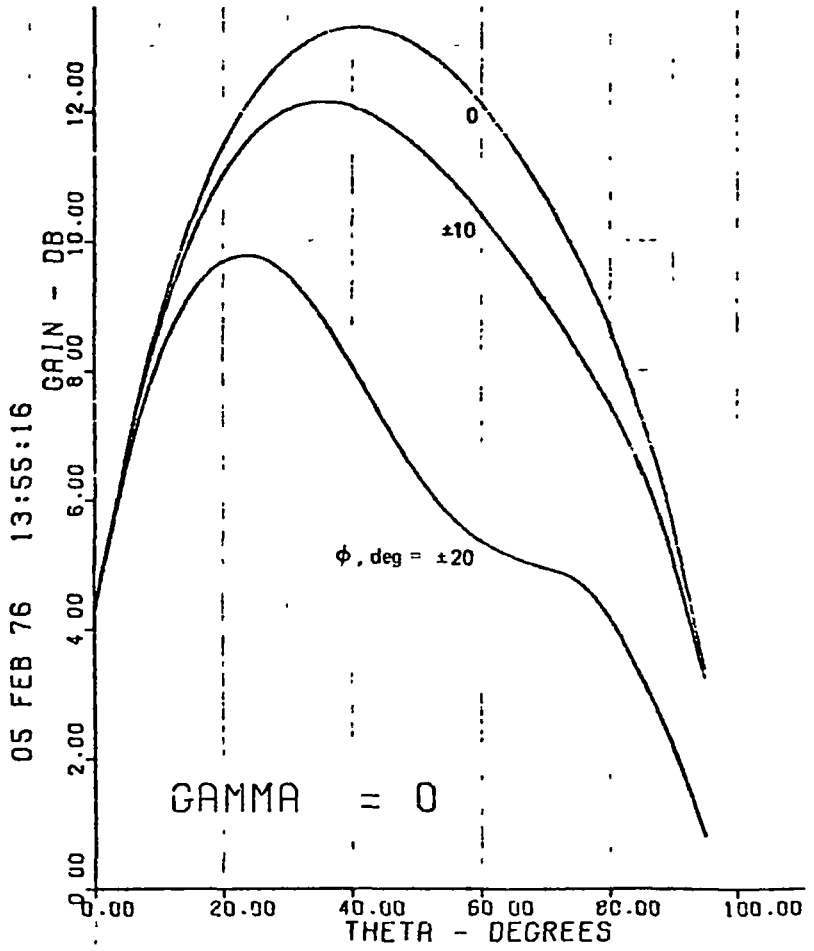


FIGURE 5-8 EDA GAIN VERSUS ASPECT ANGLE FOR FIVE ACTIVE ELEMENTS AND Y= 0 DEGREES

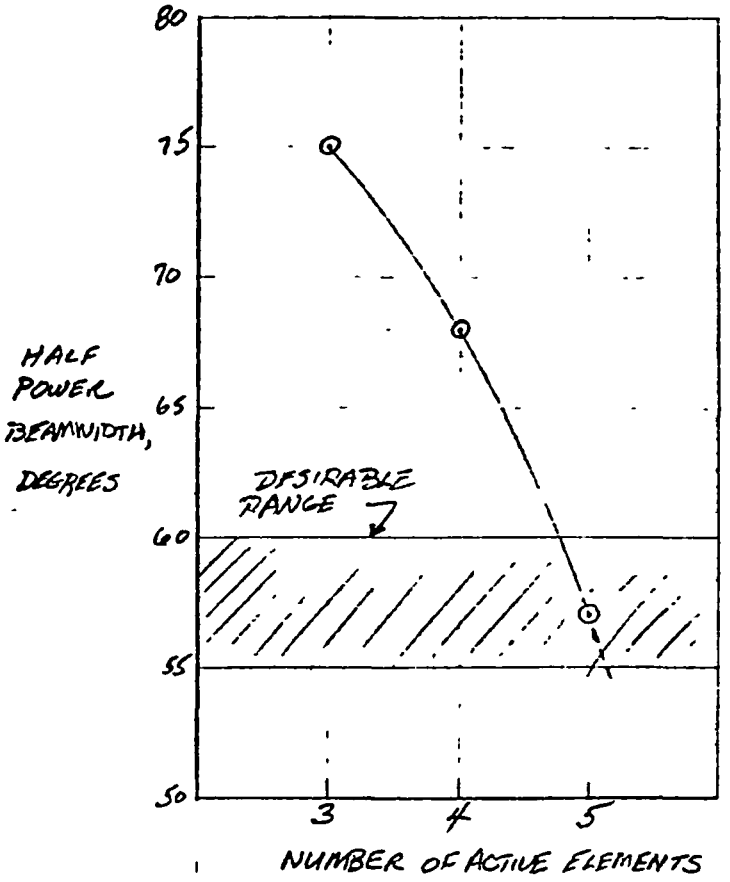


FIGURE 5-9 EDA BEAMWIDTH AS FUNCTION OF THE NUMBER OF ACTIVE ELEMENTS

Figures 5-10, 5-11, and 5-12 give the worst position performance for three, four, and five active elements. Figures 5-13 and 5-14 show the change in gain as a function of the orbiter rotational position, γ, over a range of aspect angles, θ, for n = 5 and $\varphi = 0^{\circ}$ and 10°, respectively. For various combinations of θ and φ, the lowest gains on these curves will be experienced 12 times during one spin of the orbiter and hence are the link design values.

Comparing Figures 5-13 and 5-14 and from Figures 5-8 and 5-12, it can be seen that variation of the angle φ results in significant gain degradation. If the beam center is fixed in inertial coordinates, which could be achieved by providing a star reference, then probe motion relative to the plane containing the orbiter spin axis and beam center will cause variation of φ. To this variation must be added the estimated error in beam pointing. From Figure 5-12 it can be seen that for $\theta = 70^{\circ}$ which occurs late (≈30 minutes) in the descent, the difference between $\varphi = 0$ and $\varphi = -10^{\circ}$ is approximately 2 dB. The variation of the angle φ for a fixed beam position can be determined from trajectory analysis to evaluate the effect on antenna gain. For trajectories where the orbiter and probe have the same approach orbit planes, the variation of the angle, φ, is less than 2°. Thus the $\varphi = 0$ curve in the figures is a close approximation to expected available gain.

It may be noted that in Figures 5-8 and 5-12, the peak gain for $\varphi = 0$ occurs <u>not</u> at the expected angle of 45°, but at approximately 41°. The reason for this is, that although the element boresights are mounted at an angle of 45° with respect to the spin axis, the combination of amplitude values is greater along the direction corresponding to $\theta = 41^{\circ}$, $\varphi = 0^{\circ}$, than $\theta = 45^{\circ}$. This occurs because of the circular geometry and the shape of the field intensity curve shown in Figure 5-2. If the elements are mounted so that their boresights make an angle of $\beta = 55^{\circ}$ with the spin axis, while their signals are phased for $\theta = 45^{\circ}$, $\varphi = 0^{\circ}$, the peak gain occurs at $\theta = 46^{\circ}$. This is shown in Figure 5-15.

The effect of the element pattern on the array pattern is of interest. For an element pattern with a 3 dB beamwidth of 60° and 10 dB peak gain, the array pattern is shown in Figures 5-16 and 5-17 for three and five active elements, respectively. These may be compared with Figures 5-10 and 5-12, but note that the ordinate scales are different. The results are as expected, the peak gains are larger, and the 3 dB beamwidths of the array are approximately 61° and 55°, respectively. It can be seen by comparing Figures 5-16 and 5-17 that the difference between employing three active elements and five is small for this case. The purpose of presenting Figures 5-16 and 5-17 corresponding to a smaller element beamwidth (higher gain), is to show that the element gain has an impact on how the array is operated as well as to its size.

REPRODUCIBILITY OF THE
ORIGINAL PAGE IS POOR

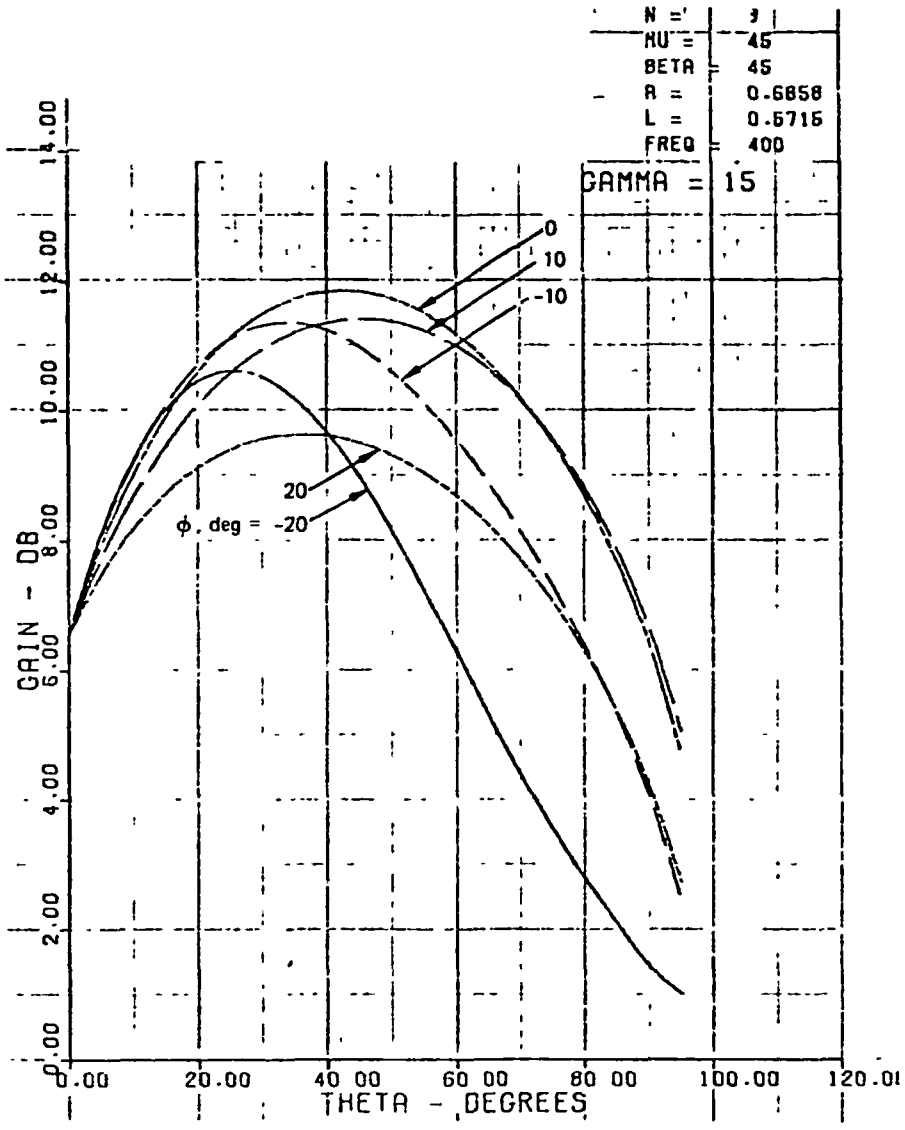


FIGURE 5-10 EDA GAIN VERSUS ASPECT ANGLE FOR THREE ACTIVE ELEMENTS AND γ = 15 DEGREES

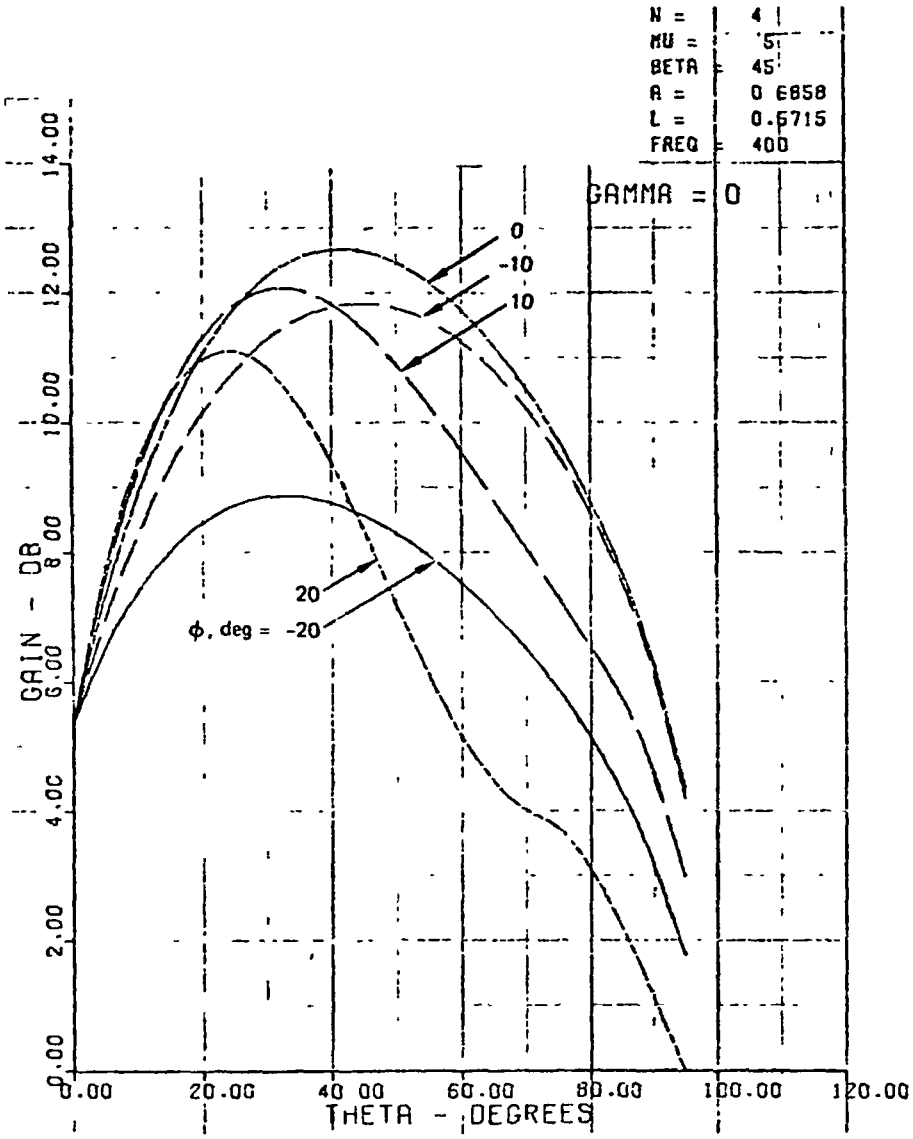


FIGURE 5.11 EDA GAIN VERSUS ASPECT ANGLE FOR FOUR ACTIVE ELEMENTS AND γ= 0 DEGREES

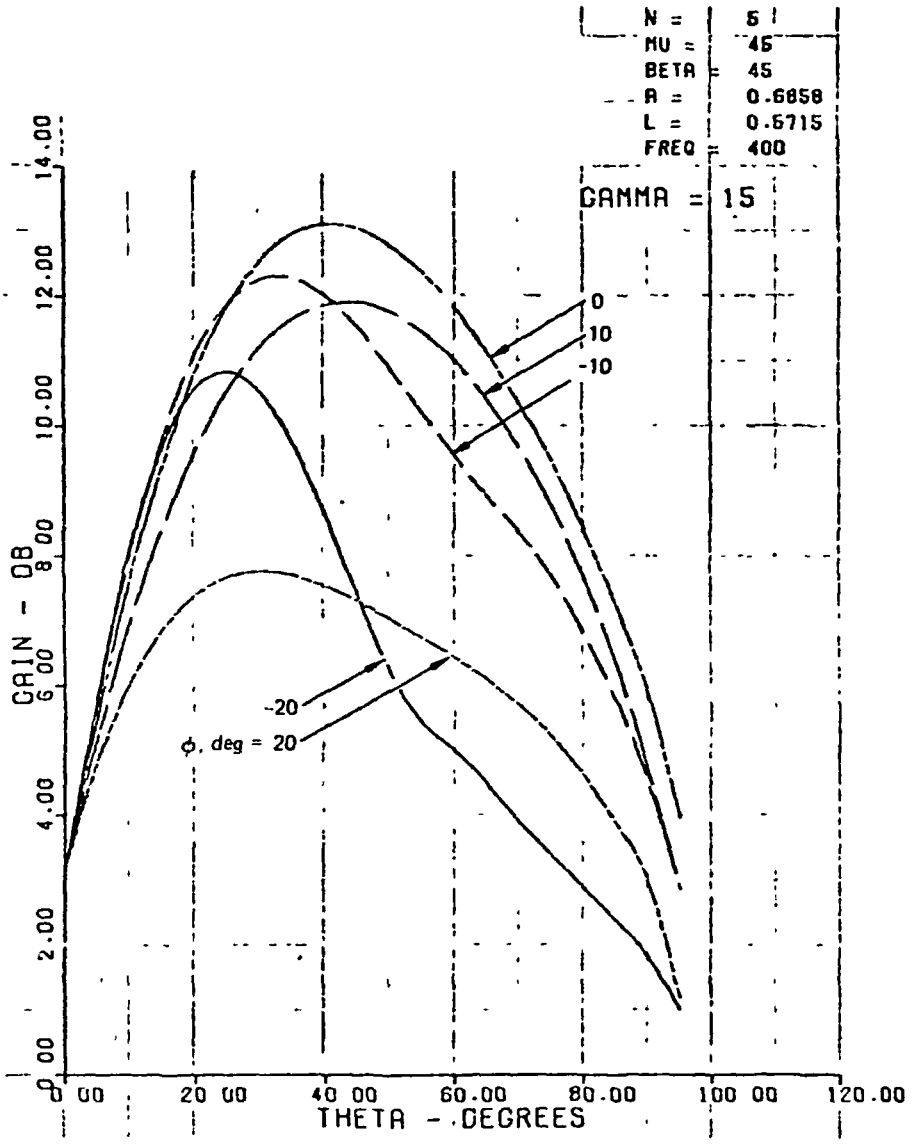


FIGURE 5 12 EDA GAIN VERSUS ASPECT ANGLE FOR FIVE ACTIVE ELEMENTS AND Y = 15 DEGREES

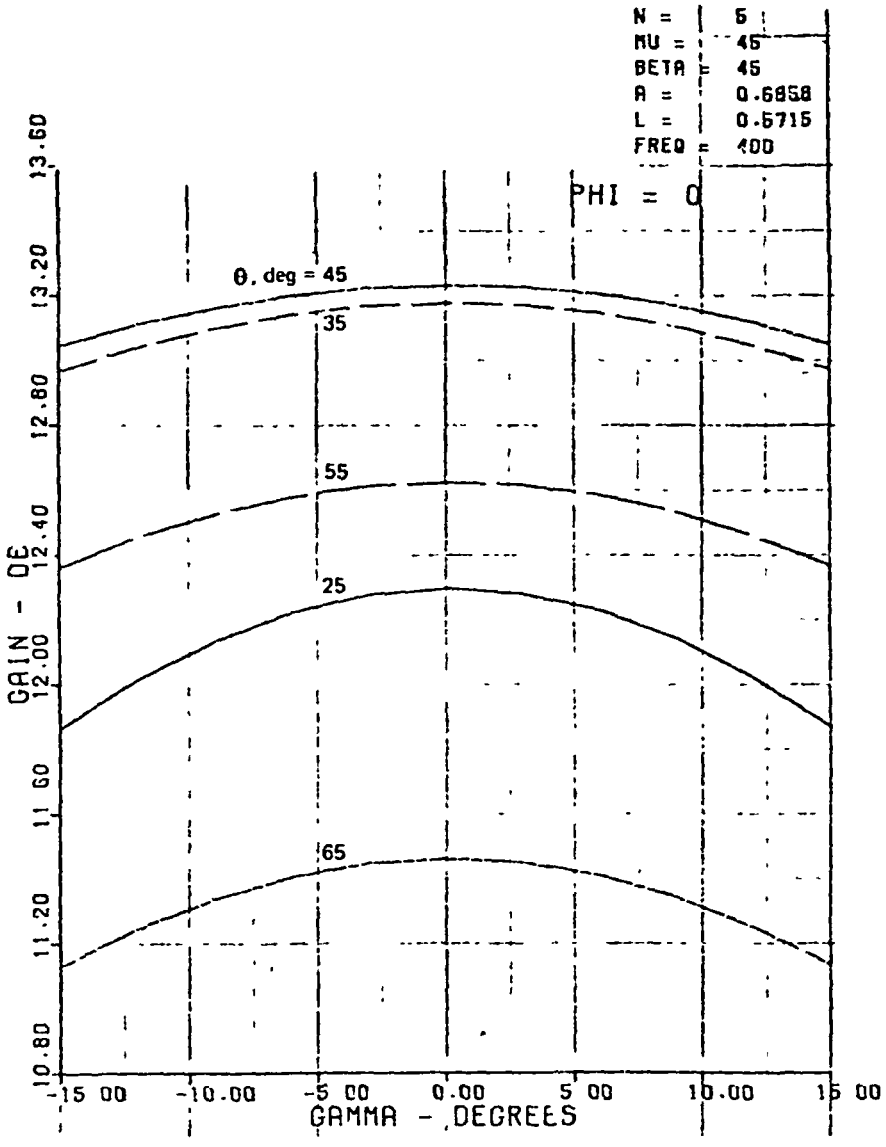


FIGURE 5 13 GAIN AS A FUNCTION OF ROTATION ANGLE FOR ϕ = 0 DEGREES

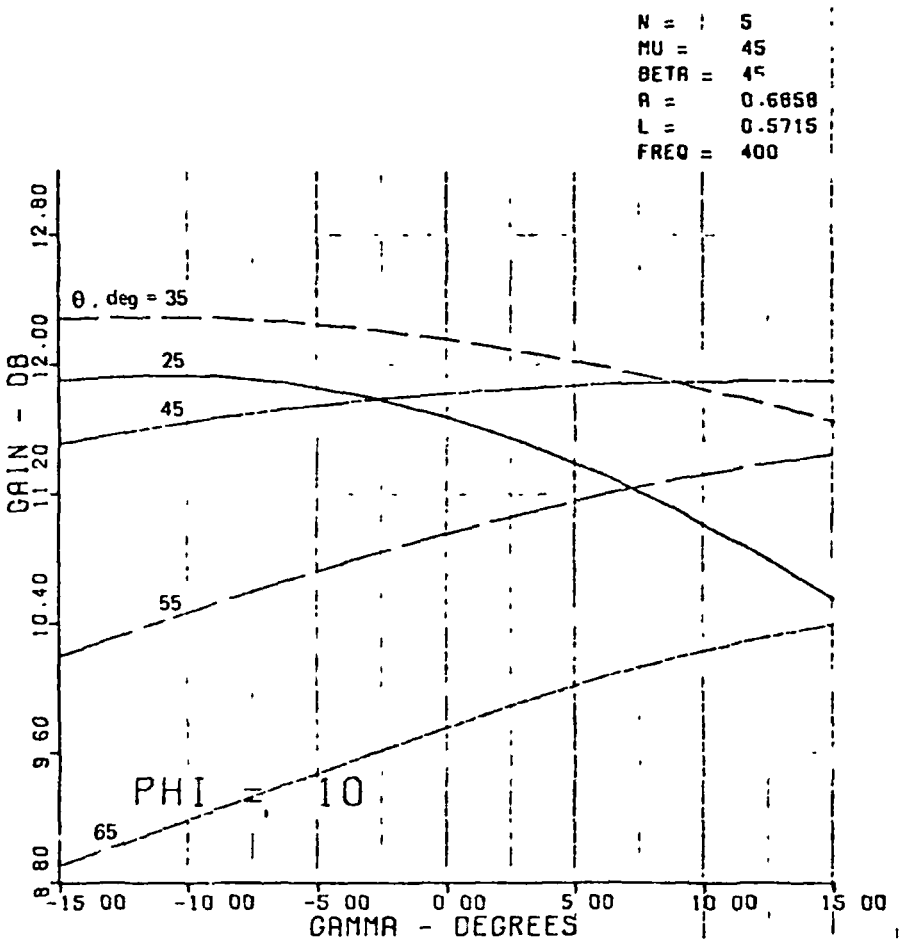


FIGURE 5-14 GAIN AS A FUNCTION OF ROTATION ANGLE FOR ϕ = 10 DEGREES

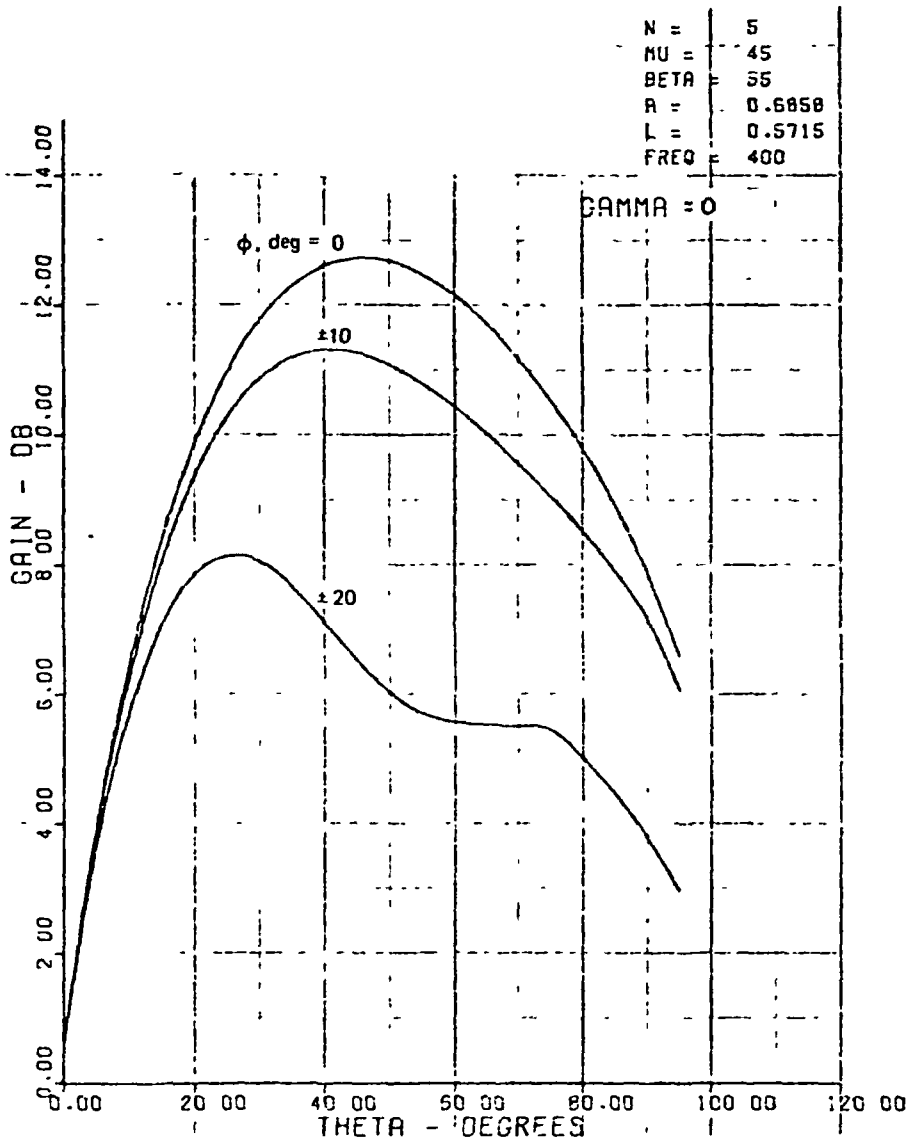


FIGURE 5-15 GAIN VERSUS ASPECT ANGLE FOR ELEMENT BORESIGHTS AT AN ANGLE OF 55 DEGREES

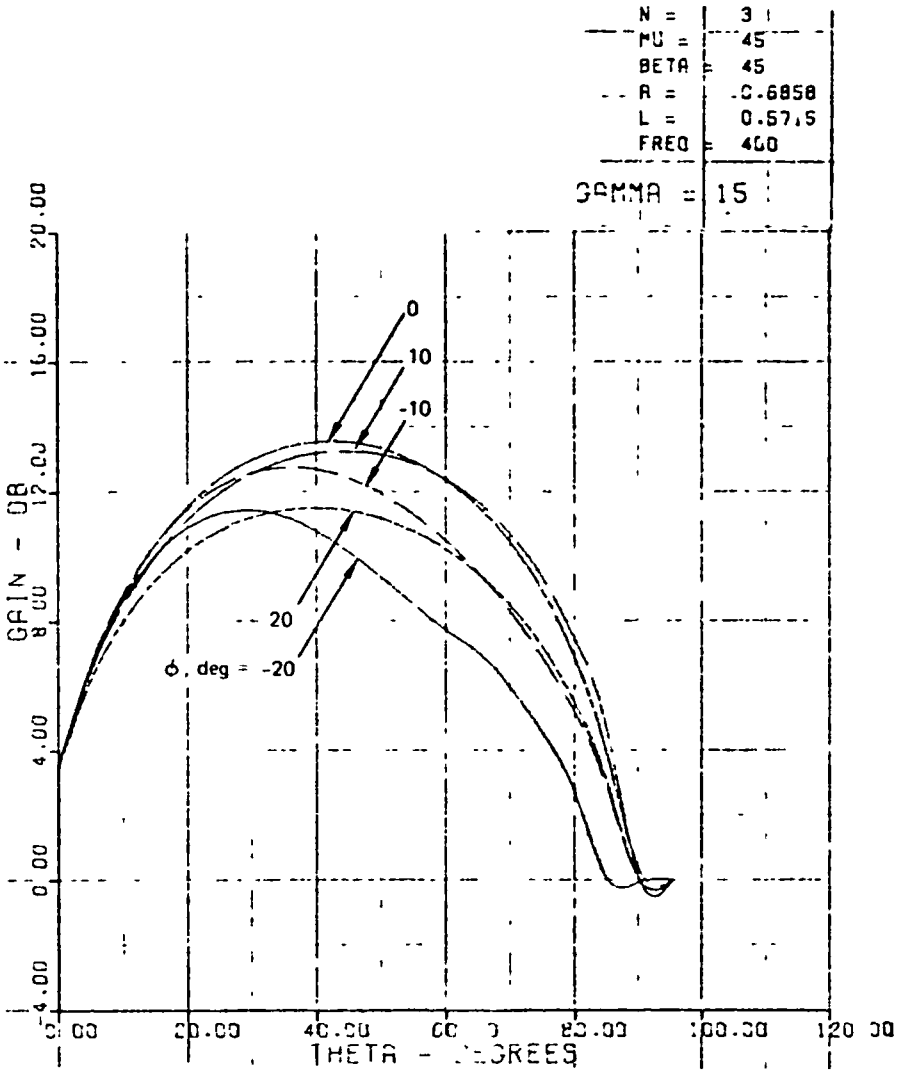


FIGURE 5 16 GAIN VERSUS ASPECT ANGLE FOR THREE ACTIVE ELEMENTS EACH ELEMENT WITH A 60 DEGREE BEAMWIDTH AND 10 DB PEAK GAIN

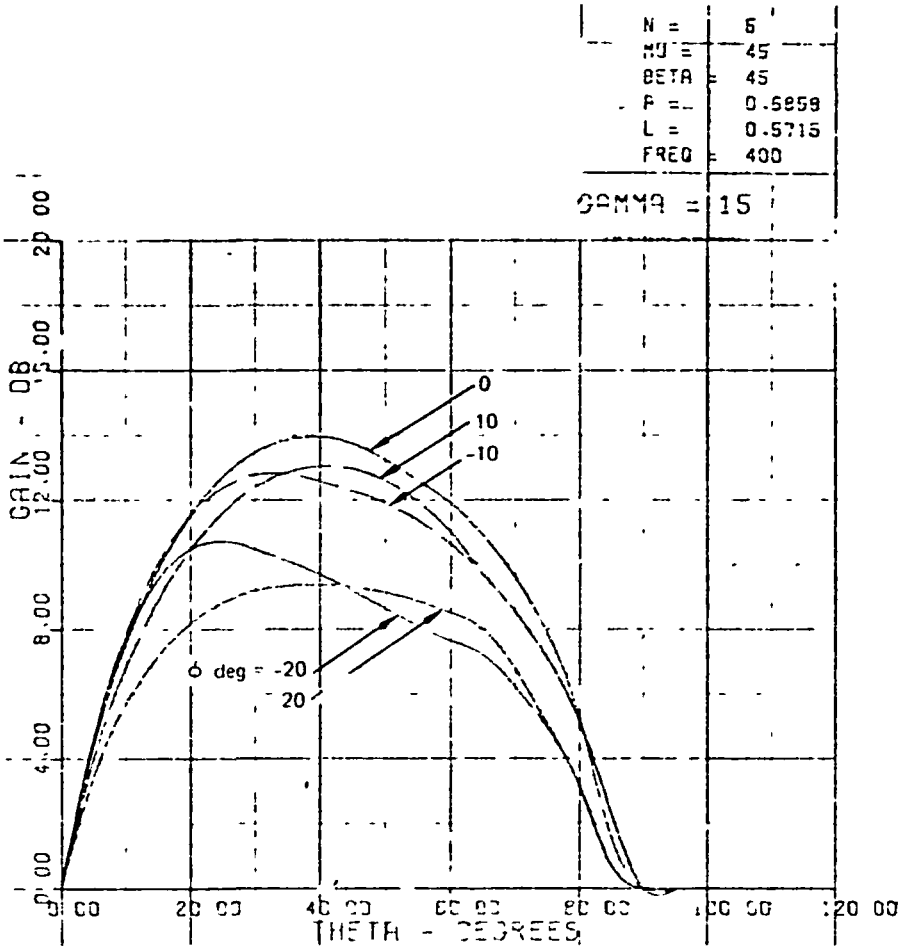


FIGURE 5.17 GAIN VERSUS ASPECT ANGLE FOR FIVE ACTIVE ELEMENTS EACH ELEMENT WITH A 60 DEGREE BEAMWIDTH AND 10 DB PEAK GAIN

Further study is required in this area to determine an optimum combination of: 1) the total number of elements, 2) the gain and field pattern of the elements, and 3) the number of active elements.

More complete antenna pattern data corresponding to Figures 5-6, 5-7, 5-8, 5-10, 5-11, 5-12, 5-13, and 5-14 is given in the Appendix.

5.4 ELECTRONICS

5.4.1 Description

The electronic components of an EDA system are shown in Figure 5-18. The individual antenna elements have separate preamp/phase-shifter modules located nearby. The separate outputs from the preamp/phase-shifter modules, of which only five are on at one time, are summed and carried to the UHF receiver. The phase-shift waveforms and the on/off switching for the desired active elements are generated by a waveform generator module.

The preamps are low noise transistor amplifiers with approximately 3 dB noise figure. Hybrid or printed circuit construction would reduce the gain and phase differences between units to the same order as the antenna element differences, and minimize the phasing adjustment of system. The amplifiers are switched on and off upon command from the waveform generator, but are brought to and from normal operating voltage with a 50 ms time-constant to prevent an instantaneous jump in the phase of the received signal. The phase tracking requirement is discussed in the section on phase-jump and loop stability.

The phase-shifters are varactor phase modulators, configured as shown in Figure 5-19. The technique of using multiple high-pass sections has been used in applications requiring wide ($\pm 180^{\circ}$) deviation and has yielded low (less than 3 percent nonlinearity). In this application the phase-shift required is $\pm 200^{\circ}$. As in the case of the preamp, hybridized construction is preferred.

Following the phase shifters, the signals are amplified to overcome the loss of the summing network. These amplifiers need only be on when the corresponding preamps are on. The summing network is made with cascaded 4 port hybrids and a three-way summer built with quarterwave matching sections as illustrated in Figure 5-20.

The function generator block diagram is shown in Figure 5-21. The spacecraft angle reference is integrated to produce sine and cosine outputs. These outputs are summed in the phase-shift driver amplifiers with a gain determined by the equation:

$$(\cos\emptyset_n) \sin\omega t + (\sin\emptyset_n) \cos \omega t$$

$$\theta_n = 0^{\circ}, 30^{\circ}, 60^{\circ} \ldots\ldots 330^{\circ}$$

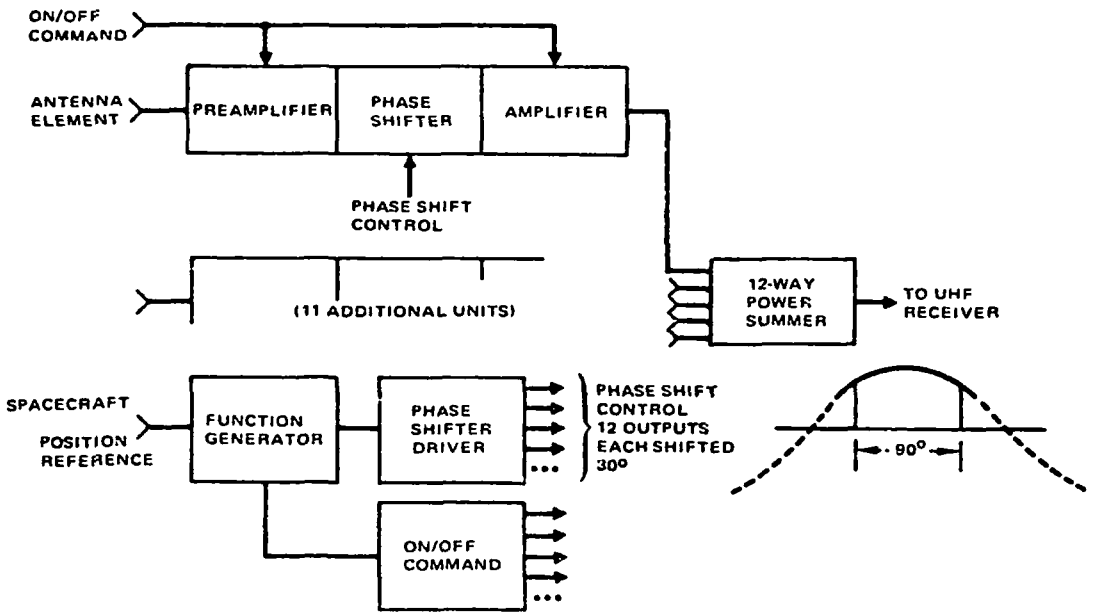


FIGURE 5 18 EDA ELECTRONICS

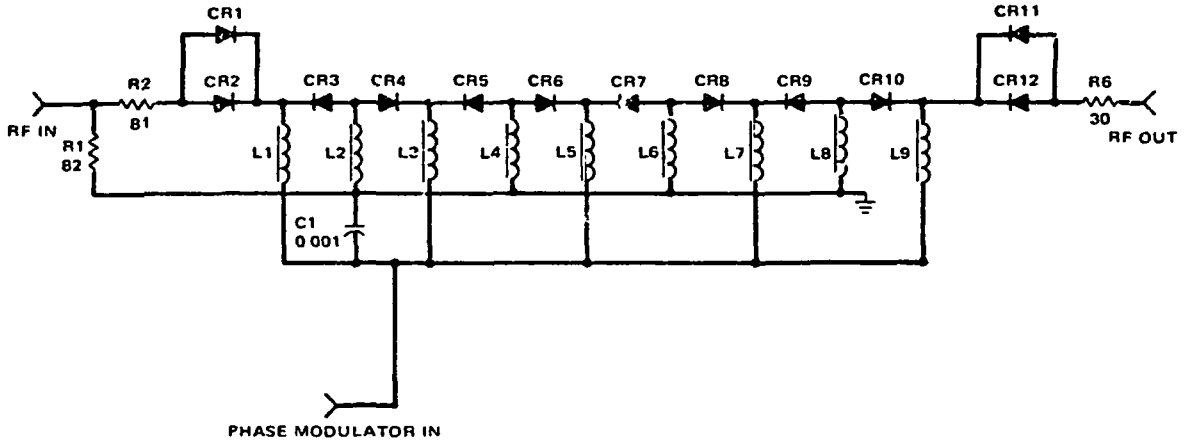


FIGURE 5 19 LINEAR PHASE SHIFTER

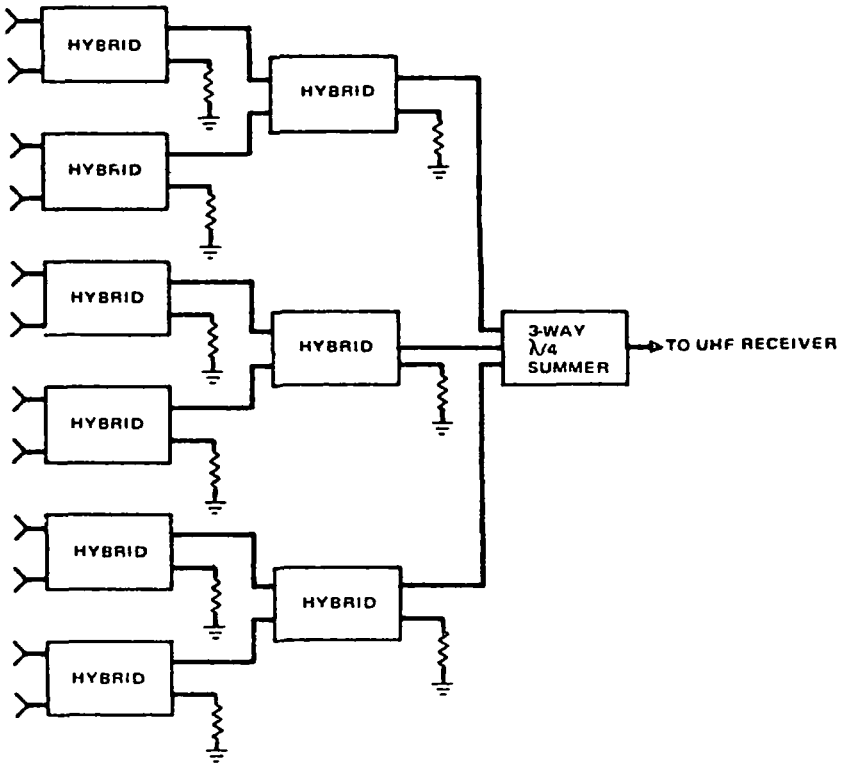


FIGURE 5-20 12-WAY POWER SUMMER

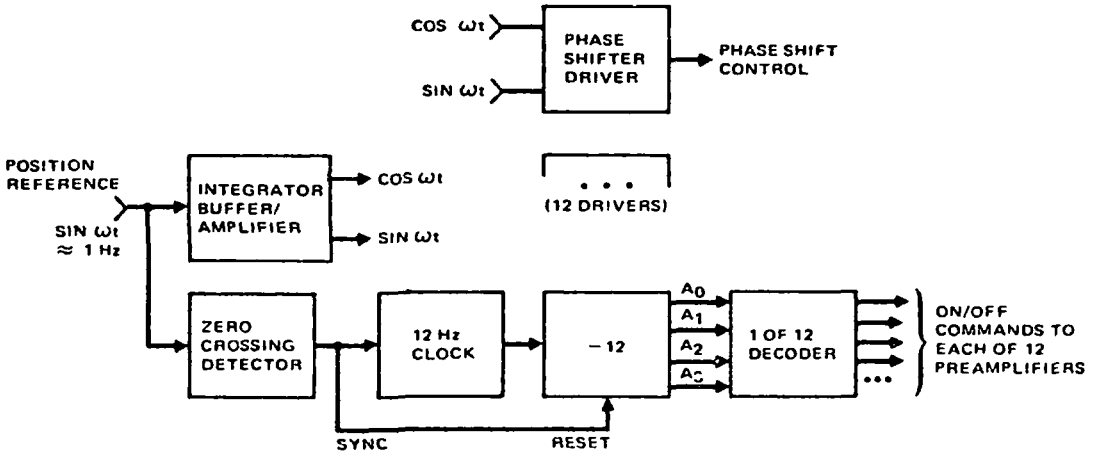


FIGURE 5 21. PHASE SHIFTER CONTROL ELECTRONICS

Single operational amplifiers are sufficient to produce each of the 12 output signals. Each phase shift signal is used only during the 150° of the cycle, while the element is on.

The on/off commands are generated by a clock which operates at 12 times the spin rate. A zero crossing detector provides a sync signal to lock the clock to the spin reference and reset a divide-by-12 counter. The counter produces a BCD 4-bit output which counts from 0 to 11 over and over. The phase-shifter decoder has 12 outputs which each go to a low state while their respective code is occurring.

5.4.2 Phase-Jump and Loop Stability

A change in the received signal phase occurs when the active elements are switched. Examining Figures 5-3 and 5-4, it can be seen that the outer elements (4 and 5) which are being switched off and on, respectively, will be receiving the incoming signal at different phases when the transmitter is off axis. The phase change as a function of the probe location angles is given in Table 5-2 for the selected five active elements. Note that when the transmitter is at the center of the beam, the symmetry between the entering and leaving preamps gives no phase change in the signal. However, when the probe transmitter is off axis ($\phi \neq 0$), the jump in the received signal phase must be tracked by the receiver's phase locked loop. To prevent a step change in the phase, the entering and leaving amplifiers are slowly turned off and on with a controlled time-constant. This would give a ramp-like change in the phase of the signal, as opposed to a step.

Table 5-3 shows the phase change for three active elements and, as expected, the phase change is greater with five active elements than with three. This phase change occurs 12 times every spacecraft revolution and the receiver phase lock loop must reduce the phase error without significantly degrading the data detection.

5.4.3 Physical Description

It is proposed that individual RF modules be placed close to each antenna element and that these modules contain hybrid integrated circuits: preamp, phase-shifter, and post amplifier. The major factor in the weight and size of these modules is the outer housing.

The summing network will be housed within the UHF receiver as will the function generator. The function generator contains approximately 11 ICs and may be fabricated on a two-layer circuit board.

TABLE 5 2 PHASE CHANGE AT SWITCHINGS WITH 5 ACTIVE ELEMENTS

Aspect Angle θ Deg	Off-Axis Angle, φ - Degrees														
	-35.00	-30.00	-25.00	-20.00	-15.00	-10.00	-5.00	.00	5.00	10.00	15.00	20.00	25.00	30.00	35.00
0.	.00	.00	.00	.00	.00	.00	.00	.00	.00	.00	.00	.00	.00	.00	.00
5.	23.26	19.91	16.55	13.21	9.85	6.58	3.28	.00	-3.28	-6.58	-9.88	-13.21	-16.55	-19.91	-23.26
10.	36.91	30.60	24.70	19.21	14.08	9.23	4.57	-.00	-4.57	-9.23	-14.08	-19.21	-24.70	-30.60	-36.91
15.	45.97	36.41	28.24	21.28	15.23	9.83	4.82	.00	-4.82	-9.83	-15.23	-21.28	-28.24	-36.41	-45.97
20.	53.26	39.59	29.30	21.44	15.09	9.65	4.72	-.00	-4.72	-9.65	-15.09	-21.44	-29.30	-39.59	-53.26
25.	60.55	40.99	28.95	20.66	14.67	9.42	4.62	.00	-4.62	-9.42	-14.67	-20.86	-28.95	-40.99	-60.55
30.	69.92	40.53	27.83	20.33	14.60	9.53	4.72	.00	-4.72	-9.53	-14.60	-20.33	-27.83	-40.53	-69.92
35.	87.73	36.90	26.66	20.61	15.36	10.26	5.14	.00	-5.14	-10.26	-15.36	-20.61	-26.66	-36.90	-87.73
40.	-102.32	27.77	24.65	22.44	17.33	11.77	5.95	.00	-5.95	-11.77	-17.33	-22.44	-24.65	-27.77	102.32
45.	-45.25	18.35	29.47	26.50	20.80	14.18	7.17	.00	-7.17	-14.18	-20.80	-26.50	-29.47	-18.35	45.25
50.	-3.73	21.23	35.60	32.83	25.77	17.50	8.82	.00	-8.82	-17.50	-25.77	-32.83	-35.60	-21.23	3.73
55.	28.57	31.11	42.09	40.31	31.85	21.59	10.85	.00	-10.85	-21.59	-31.85	-40.31	-42.09	-31.11	-28.57
60.	48.53	44.83	48.96	47.05	38.19	26.13	13.16	.00	-13.16	-26.13	-38.19	-47.05	-48.66	-44.83	-48.53
65.	60.56	56.85	55.80	52.15	43.83	30.69	15.61	.00	-15.61	-30.69	-43.83	-52.15	-55.80	-56.85	-60.56
70.	67.78	65.96	62.66	56.87	47.65	34.83	18.03	.00	-18.03	-34.83	-47.65	-56.87	-62.66	-65.96	-67.78
75.	71.59	72.58	68.57	61.13	50.61	37.14	20.28	.00	-20.28	-37.14	-50.61	-61.13	-68.57	-72.58	-71.59
80.	77.11	77.45	73.38	64.75	53.00	38.31	20.76	.00	-20.76	-38.31	-53.00	-64.75	-73.38	-77.45	-77.11
85.	83.51	81.71	77.30	67.72	54.79	38.80	19.76	.00	-19.76	-38.80	-54.79	-67.72	-77.30	-81.71	-83.51
90.	89.17	85.83	80.24	70.16	56.03	38.54	19.24	.00	-19.24	-38.54	-56.03	-70.16	-80.24	-85.83	-89.17
95.	94.85	90.10	83.02	72.04	56.79	38.19	19.17	.00	-19.17	-38.19	-56.79	-72.04	-83.02	-90.10	-94.85
100.	101.59	95.35	86.90	74.36	56.27	37.75	18.95	.00	-18.95	-37.75	-56.27	-74.36	-86.90	-95.35	-101.59
105.	109.26	103.25	90.12	72.93	55.19	37.03	18.58	.00	-18.58	-37.03	-55.19	-72.93	-90.12	-103.25	-109.26

TABLE 5 3 PHASE CHANGE AT SWITCHINGS WITH 3 ACTIVE ELEMENTS

Aspect Angle θ Deg.	Off-Axis Angle, φ - Degrees														
	-35.00	-30.00	-25.00	-20.00	-15.00	-10.00	-5.00	.00	5.00	10.00	15.00	20.00	25.00	30.00	35.00
0.	.00	.00	.00	.00	.00	.00	.00	.00	.00	.00	.00	.00	.00	.00	.00
5.	1.64	1.43	1.20	.97	.73	.49	.25	.00	-.25	-.49	-.73	-.97	-1.20	-1.43	-1.64
10.	3.23	2.79	2.35	1.89	1.42	.95	.48	.00	-.48	-.95	-1.42	-1.89	-2.35	-2.79	-3.23
15.	4.75	4.10	3.43	2.76	2.08	1.39	.70	.00	-.70	-1.39	-2.08	-2.76	-3.43	-4.10	-4.75
20.	6.23	5.37	4.50	3.63	2.74	1.83	.92	.00	-.92	-1.83	-2.74	-3.63	-4.50	-5.37	-6.23
25.	7.69	6.68	5.64	4.56	3.45	2.32	1.16	.00	-1.16	-2.32	-3.45	-4.56	-5.64	-6.68	-7.69
30.	9.23	8.13	6.92	5.63	4.28	2.88	1.45	.00	-1.45	-2.88	-4.28	-5.63	-6.92	-8.13	-9.23
35.	10.99	9.64	8.47	6.92	5.27	3.55	1.78	.00	-1.78	-3.55	-5.27	-6.92	-8.47	-9.66	-10.99
40.	13.22	12.11	10.45	8.53	6.48	4.35	2.18	.00	-2.18	-4.35	-6.48	-8.53	-10.45	-12.11	-13.22
45.	16.32	15.15	13.01	10.54	7.95	5.31	2.66	.00	-2.66	-5.31	-7.95	-10.54	-13.01	-15.15	-16.32
50.	20.71	19.30	16.34	13.05	9.72	6.44	3.21	.00	-3.21	-6.44	-9.72	-13.05	-16.34	-19.30	-20.71
55.	28.48	24.77	20.59	16.12	11.83	7.75	3.84	.00	-3.84	-7.75	-11.83	-16.12	-20.59	-24.77	-28.48
60.	32.67	31.35	25.74	19.77	14.27	9.24	4.54	.00	-4.54	-9.24	-14.27	-19.77	-25.74	-31.35	-32.67
65.	37.53	36.21	31.58	23.97	17.04	10.91	5.32	.00	-5.32	-10.91	-17.04	-23.97	-31.58	-38.21	-37.53
70.	39.92	44.18	37.64	28.58	20.12	12.75	6.18	.00	-6.18	-12.75	-20.12	-28.58	-37.64	-44.18	-39.92
75.	40.00	48.37	43.32	33.42	23.48	14.74	7.11	.00	-7.11	-14.74	-23.48	-33.42	-43.32	-48.37	-40.00
80.	41.04	50.61	48.17	38.33	27.12	16.99	8.15	.00	-8.15	-16.99	-27.12	-38.33	-48.17	-50.61	-41.04
85.	44.32	51.71	52.03	43.22	31.13	19.54	9.34	.00	-9.34	-19.54	-31.13	-43.22	-52.03	-51.71	-44.32
90.	49.02	53.03	53.55	48.23	35.77	22.63	10.80	.00	-10.80	-22.63	-35.77	-48.23	-53.55	-53.03	-49.02
95.	55.31	54.68	54.05	49.64	41.61	26.79	12.81	.00	-12.81	-26.79	-41.61	-49.64	-54.05	-54.68	-55.31
100.	63.75	57.96	54.69	50.02	42.60	32.56	16.03	.00	-16.03	-32.56	-42.60	-50.02	-54.69	-57.96	-63.75
105.	69.06	64.34	56.59	50.57	42.97	32.63	19.06	.00	-19.06	-32.63	-42.97	-50.57	-56.59	-64.34	-69.06

REPRODUCIBILITY OF THE ORIGINAL PAGE IS POOR

	Size, cm	g	Power Requirement
RF module	2.5 x 5 x 1.3	142 (x12)	15 V at 32 mA (x5)
Summer	10 x 7.6 x 2	227	-
Function generator	10 x 13 x 1.3	114	±5 V at 50 mA
Miscellaneous cabling	-	227	-
		2272	2.75 W

5.4.4 Development Considerations

The design of the electronics is straightforward and applies existing techniques. The construction of hybrid IC preamps and phase-shifters places the burden of weight on the enclosure and the package weights more than the circuitry.

The function generator is quite simple in its present form. As presently defined, it provides the logic to despin the antenna. With a 50 percent increase in complexity, the antenna could be electronically scanned in the plane of the antenna by varying the phase of the position reference signal. The pattern of the antenna would then shift around the spacecraft in correspondence with the angular delay of the reference.

5.5 SUMMARY

An EDA has been described, suitable for the probe-orbiter link on an outer planet mission. The system chosen as a model for this investigation uses a two-turn quadrifilar helix antenna element. Twelve elements are mounted on a 137 cm diameter base ring, concentric with the spacecraft axis. Each element is tilted at 45° to provide the proper angle bias. The 12 elements drive 12 preamp/phase-shifter units, the outputs of which are summed to a common output.

The system characteristics are summarized as follows:

Antenna element	Two-turn quadrifilar helix
Element beamwidth (3 dB)	80°
Polarization	Circular
Matching/phasing	3 dB hybrid
Element gain	7.75 dB
Element length	57 cm
Number of elements	12

Angular offset	45° (Figure 5-4)
Number of active elements	5
Mount ring diameter	137 cm
Peak array gain	13 dB
Array beamwidth (3 dB)	54°, $\varphi = 0°$
	<40°, $\varphi = 0°$
Electronics	12 preamp/phase-shifters
	Summer
	Waveform generator

The weight breakdown is as follows:

	No.	Mass, kg	
		Mass/Unit	Total Across
Antenna elements	12	0.28	3.36
RF module	12	0.14	1.68
Summer	1	0.23	0.23
Function generator	1	0.15	0.15
Miscellaneous	1	0.23	0.23
Mounting ring	1	1.85	1.85
			7.5 kg

APPENDIX

The following tables provide a more detailed description of the antenna pattern. Tables A-1 to A-6 show gain as a function of the field position angles θ and φ (see Figure 5-4) for values of rotation angle γ (see Figure 5-3) corresponding to maximum and minimum performance during a spin revolution. Tables A-7 and A-8 show gain as a function of the rotation angle, γ, and aspect angle, θ, for $\varphi = 0$ and 10°, respectively.

TABLE A 1 ANTENNA GAIN IN DB FOR 3 ACTIVE ELEMENTS AND Y = 0 DEGREES

Rotation Angle Y	Aspect Angle θ	Off Axis Angle, φ														
		-35.00	-30.00	-25.00	-20.00	-15.00	-10.00	-5.00	.00	5.00	10.00	15.00	20.00	25.00	30.00	35.00
0.	0.	7.97	7.97	7.97	7.97	7.97	7.97	7.97	7.97	7.97	7.97	7.97	7.97	7.97	7.97	7.97
0.	5.	8.72	8.79	8.86	8.91	8.96	8.99	9.01	9.02	9.01	8.99	8.96	8.91	8.86	8.79	8.72
0.	10.	9.08	9.28	9.45	9.59	9.71	9.79	9.84	9.86	9.84	9.79	9.71	9.59	9.45	9.28	9.08
0.	15.	9.10	9.46	9.78	10.04	10.25	10.40	10.50	10.53	10.50	10.40	10.25	10.04	9.78	9.46	9.10
0.	20.	8.79	9.37	9.87	10.29	10.62	10.86	11.01	11.05	11.01	10.86	10.62	10.29	9.87	9.37	8.79
0.	25.	8.18	9.03	9.76	10.37	10.84	11.18	11.39	11.46	11.39	11.18	10.84	10.37	9.76	9.03	8.18
0.	30.	7.28	8.46	9.46	10.28	10.92	11.38	11.66	11.75	11.66	11.38	10.92	10.28	9.46	8.46	7.28
0.	35.	6.10	7.68	9.00	10.06	10.89	11.47	11.82	11.94	11.82	11.47	10.89	10.06	9.00	7.68	6.10
0.	40.	4.69	6.73	8.39	9.72	10.74	11.46	11.89	12.03	11.89	11.46	10.74	9.72	8.39	6.73	4.69
0.	45.	3.09	5.63	7.67	9.28	10.50	11.35	11.86	12.03	11.86	11.35	10.50	9.28	7.67	5.63	3.09
0.	50.	1.43	4.44	6.85	8.74	10.17	11.16	11.75	11.94	11.75	11.16	10.17	8.74	6.85	4.44	1.43
0.	55.	-.11	3.23	5.98	8.13	9.75	10.88	11.54	11.76	11.54	10.88	9.75	8.13	5.98	3.23	-.11
0.	60.	-1.28	2.10	5.08	7.47	9.26	10.51	11.24	11.49	11.24	10.51	9.26	7.47	5.08	2.10	-1.28
0.	65.	-1.96	1.14	4.20	6.75	8.69	10.05	10.85	11.11	10.85	10.05	8.69	6.75	4.20	1.14	-1.96
0.	70.	-2.22	.39	3.37	6.00	8.05	9.49	10.35	10.63	10.35	9.49	8.05	6.00	3.37	.39	-2.22
0.	75.	-2.24	-.14	2.59	5.20	7.31	8.82	9.72	10.01	9.72	8.82	7.31	5.20	2.59	-.14	-2.24
0.	80.	-2.18	-.50	1.86	4.35	6.47	8.01	8.94	9.25	8.94	8.01	6.47	4.35	1.86	-.50	-2.18
0.	85.	-2.10	-.76	1.16	3.42	5.48	7.03	7.97	8.29	7.97	7.03	5.48	3.42	1.16	-.76	-2.10
0.	90.	-2.02	-.98	.46	2.37	4.29	5.81	6.75	7.07	6.75	5.81	4.29	2.37	.46	-.98	-2.02
0.	95.	-3.07	-1.20	-.30	1.12	2.80	4.24	5.18	5.50	5.18	4.24	2.80	1.12	-.30	-1.20	-3.07
0.	100.	-4.88	-2.91	-1.28	-.43	.84	2.14	3.04	3.36	3.04	2.14	.84	-.43	-1.28	-2.91	-4.88
0.	105.	-7.33	-5.59	-3.96	-2.73	-1.94	-.96	-.11	.20	-.11	-.96	-1.94	-2.73	-3.96	-5.59	-7.33

*FIN

TABLE A 2 ANTENNA GAIN IN DB FOR 4 ACTIVE ELEMENTS AND γ = 15 DEGREES

Rotation Angle γ	Aspect Angle θ	Off Axis Angle, Φ													
		-35.00	-30.00	-25.00	-20.00	-15.00	-10.00	-5.00	.00	5.00	10.00	15.00	20.00	25.00	30.00	35.00
15.	0.	7.51	7.51	7.51	7.51	7.51	7.51	7.51	7.51	7.51	7.51	7.51	7.51	7.51	7.51	7.51
15.	5.	8.46	8.58	8.68	8.76	8.83	8.88	8.90	8.91	8.90	8.88	8.83	8.76	8.68	8.58	8.46
15.	10.	8.82	9.13	9.40	9.63	9.81	9.94	10.02	10.05	10.02	9.94	9.81	9.63	9.40	9.13	8.82
15.	15.	8.62	9.22	9.73	10.17	10.51	10.75	10.90	10.95	10.90	10.75	10.51	10.17	9.73	9.22	8.62
15.	20.	7.89	8.88	9.72	10.41	10.95	11.34	11.57	11.65	11.57	11.34	10.95	10.41	9.72	8.88	7.89
15.	25.	6.62	8.13	9.38	10.40	11.18	11.74	12.07	12.18	12.07	11.74	11.18	10.40	9.38	8.13	6.62
15.	30.	4.78	6.98	8.76	10.15	11.22	11.96	12.40	12.55	12.40	11.96	11.22	10.15	8.76	6.98	4.78
15.	35.	2.32	5.48	7.88	9.72	11.08	12.03	12.59	12.78	12.59	12.03	11.08	9.72	7.88	5.48	2.32
15.	40.	-.72	3.68	6.80	9.12	10.81	11.97	12.65	12.87	12.65	11.97	10.81	9.12	6.80	3.68	-.72
15.	45.	-3.77	1.77	5.62	8.40	10.41	11.78	12.58	12.84	12.58	11.78	10.41	8.40	5.62	1.77	-3.77
15.	50.	-5.17	.13	4.44	7.62	9.92	11.49	12.40	12.70	12.40	11.49	9.92	7.62	4.44	.13	-5.17
15.	55.	-4.49	-.80	3.43	6.84	9.37	11.10	12.11	12.44	12.11	11.10	9.37	6.84	3.43	-.80	-4.49
15.	60.	-3.46	-.99	2.68	6.10	8.76	10.62	11.71	12.07	11.71	10.62	8.76	6.10	2.68	-.99	-3.46
15.	65.	-2.86	-.81	2.22	5.43	8.12	10.05	11.21	11.59	11.21	10.05	8.12	5.43	2.22	-.81	-2.86
15.	70.	-2.78	-.62	1.97	4.84	7.44	9.40	10.59	10.49	10.59	9.40	7.44	4.84	1.97	-.62	-2.78
15.	75.	-3.13	-.55	1.81	4.32	6.73	8.65	9.84	10.25	9.84	8.65	6.73	4.32	1.81	-.55	-3.13
15.	80.	-3.51	-.63	1.66	3.83	5.97	7.77	8.94	9.34	.94	7.77	5.97	3.83	1.66	-.64	-3.51
15.	85.	-3.78	-1.15	1.49	3.32	5.12	6.73	7.83	8.21	7.83	6.73	5.12	3.32	1.49	-1.15	-3.78
15.	90.	-4.08	-1.93	.70	2.76	4.13	5.45	6.43	6.79	6.43	5.45	4.13	2.76	.70	-1.93	-4.08
15.	95.	-4.43	-2.83	-.61	1.47	2.92	3.83	4.61	4.91	4.61	3.83	2.92	1.47	-.61	-2.83	-4.43
15.	100.	-4.86	-3.92	-2.31	-.51	.88	1.64	2.06	2.26	2.06	1.64	.88	-.51	-2.31	-3.92	-4.86
15.	105.	-6.30	-5.31	-4.62	-3.35	-2.18	-1.56	-1.63	-1.97	-1.63	-1.56	-2.18	-3.35	-4.62	-5.31	-6.30

*FIN

TABLE A 3 ANTENNA GAIN IN DB FOR 5 ACTIVE ELEMENTS AND Y = 0 DEGREES

Rotation Angle, Y	Aspect Angle θ	Off-Axis Angle, Φ													
		-35.00	-30.00	-25.00	-20.00	-15.00	-10.00	-5.00	.00	5.00	10.00	15.00	20.00	25.00	30.00	35.00
0.	0.	4.31	4.31	4.31	4.31	4.31	4.31	4.31	4.31	4.31	4.31	4.31	4.31	4.31	4.31	4.31
0.	5.	6.16	6.50	6.50	6.63	6.74	6.81	6.86	6.87	6.86	6.81	6.74	6.63	6.50	6.34	6.16
0.	10.	7.02	7.49	7.88	8.22	8.49	8.68	8.80	8.84	8.80	8.68	8.49	8.22	7.86	7.48	7.02
0.	15.	6.99	7.65	8.59	9.21	9.70	10.05	10.27	10.34	10.27	10.05	9.70	9.21	8.59	7.85	6.99
0.	20.	6.11	7.50	8.71	9.70	10.48	11.03	11.36	11.47	11.36	11.03	10.48	9.70	8.71	7.50	6.11
0.	25.	4.27	6.46	8.30	9.77	10.89	11.67	12.14	12.30	12.14	11.67	10.89	9.77	8.30	6.46	4.27
0.	30.	1.24	4.70	7.41	9.47	10.99	12.03	12.65	12.85	12.65	12.03	10.99	9.47	7.41	4.70	1.24
0.	35.	-3.68	2.19	6.11	8.87	10.83	12.15	12.92	13.18	12.92	12.15	10.83	8.87	6.11	2.19	-3.66
0.	40.	-12.52	-.89	4.55	8.07	10.48	12.07	12.99	13.30	12.99	12.07	10.48	8.07	4.55	-.89	-12.52
0.	45.	-11.52	-3.39	3.06	7.19	9.98	11.83	12.89	13.23	12.89	11.83	9.98	7.19	3.06	-3.39	-11.52
0.	50.	-6.05	-3.45	2.07	6.38	9.42	11.45	12.62	13.00	12.62	11.45	9.42	6.38	2.07	-3.45	-6.05
0.	55.	-3.85	-2.19	1.76	5.75	8.83	10.96	12.21	12.62	12.21	10.96	8.83	5.75	1.78	-2.19	-3.85
0.	60.	-3.21	-1.22	1.94	5.34	8.20	10.40	11.68	12.11	11.68	10.40	8.20	5.34	1.94	-1.22	-3.21
0.	65.	-2.69	-.84	2.17	5.10	7.73	9.76	11.03	11.46	11.03	9.76	7.73	5.10	2.17	-.84	-2.69
0.	70.	-2.28	-.76	2.27	4.93	7.22	9.07	10.27	10.68	10.27	9.07	7.22	4.93	2.27	-.76	-2.28
0.	75.	-2.26	-.76	1.97	4.75	6.72	8.31	9.38	9.75	9.38	8.31	6.72	4.75	1.97	-.76	-2.26
0.	80.	-2.54	-.69	1.49	4.16	6.19	7.45	8.33	8.65	8.33	7.45	6.19	4.16	1.49	-.69	-2.54
0.	85.	-3.08	-1.17	.92	3.28	5.28	6.47	7.08	7.31	7.08	6.47	5.28	3.28	.92	-1.17	-3.08
0.	90.	-3.76	-1.58	.23	2.19	3.96	5.11	5.53	5.63	5.53	5.11	3.96	2.19	.23	-1.58	-3.76
0.	95.	-4.81	-2.09	-.63	.61	2.24	3.22	3.55	3.59	3.55	3.22	2.24	.61	-.63	-2.09	-4.81
0.	100.	-6.28	-3.65	-1.83	-1.00	-.14	.54	.82	1.14	.82	.54	-.14	-1.00	-1.83	-3.65	-6.28

TABLE A4 ANTENNA GAIN IN DB FOR 3 ACTIVE ELEMENTS AND Y = 15 DEGREES

Rotation Angle γ	Aspect Angle θ	Off-Axis Angle, Φ													
		-35.00	-30.00	-25.00	-20.00	-15.00	-10.00	-5.00	.00	5.00	10.00	15.00	20.00	25.00	30.00	35.00
15.	0.	6.57	6.57	6.57	6.57	6.57	6.57	6.57	6.57	6.57	6.57	6.57	6.57	6.57	6.57	6.57
15.	5.	8.14	8.19	8.16	8.14	8.12	8.06	8.02	7.99	7.85	7.75	7.63	7.49	7.35	7.18	7.01
15.	10.	9.11	9.19	9.25	9.28	9.27	9.24	9.16	9.05	8.90	8.71	8.48	8.21	7.90	7.56	7.18
15.	15.	9.57	9.77	9.93	10.04	10.10	10.11	10.05	9.93	9.74	9.49	9.16	8.75	8.27	7.72	7.10
15.	20.	9.58	9.90	10.24	10.48	10.64	10.73	10.72	10.62	10.42	10.11	9.69	9.15	8.49	7.71	6.79
15.	25.	9.18	9.74	10.23	10.63	10.93	11.13	11.20	11.14	10.94	10.60	10.10	9.43	8.58	7.54	6.29
15.	30.	8.38	9.20	9.92	10.53	11.00	11.33	11.51	11.51	11.34	10.97	10.39	9.59	8.54	7.23	5.59
15.	35.	7.23	8.34	9.35	10.20	10.87	11.37	11.66	11.75	11.61	11.22	10.58	9.65	8.41	6.80	4.74
15.	40.	5.76	7.29	8.55	9.67	10.57	11.24	11.68	11.84	11.76	11.38	10.67	9.63	8.18	6.26	3.75
15.	45.	4.07	5.92	7.57	8.97	10.12	10.99	11.57	11.85	11.81	11.43	10.68	9.51	7.87	5.65	2.67
15.	50.	2.31	4.48	6.45	8.14	9.54	10.61	11.35	11.73	11.75	11.38	10.59	9.32	7.50	4.99	1.56
15.	55.	.73	3.04	5.26	7.22	8.86	10.13	11.02	11.51	11.59	11.24	10.41	9.04	7.05	4.29	.52
15.	60.	-.37	1.80	4.11	6.28	8.10	9.55	10.59	11.19	11.33	11.00	10.14	8.69	6.55	3.57	-.39
15.	65.	-.90	.88	3.07	5.30	7.28	8.89	10.05	10.75	10.96	10.65	9.77	8.25	6.00	2.86	-1.11
15.	70.	-1.02	.35	2.24	4.38	6.43	8.14	9.42	10.21	10.47	10.18	9.28	7.72	5.38	2.17	-1.62
15.	75.	-.94	.13	1.63	3.54	5.54	7.31	8.67	9.53	9.85	9.58	8.68	7.07	4.69	1.49	-1.98
15.	80.	-1.57	.10	1.21	2.78	4.62	6.38	7.79	8.71	9.06	8.82	7.92	6.30	3.91	.81	-2.27
15.	85.	-2.63	-.62	.94	2.08	3.65	5.31	6.72	7.68	8.08	7.86	6.97	5.34	3.01	.10	-2.53
15.	90.	-3.74	-1.89	-.00	1.42	2.57	4.04	5.4	6.39	6.83	6.64	5.78	4.20	1.95	-.68	-2.83
15.	95.	-4.92	-3.40	-1.58	.07	1.34	2.46	3.7.	4.72	5.20	5.05	4.23	2.72	.64	-1.58	-3.18
15.	100.	-6.21	-5.28	-3.66	-1.98	-.59	.41	1.43	2.42	2.96	2.89	2.13	.74	-1.06	-2.68	-3.61
15.	105.	-8.25	-7.65	-6.57	-4.94	-3.44	-2.32	-1.65	-1.07	-.38	-.31	-.93	-2.10	-3.37	-4.06	-5.05

OFIN

TABLE A 5 ANTENNA GAIN IN DB FOR 4 ACTIVE ELEMENTS AND Y = 0 DEGREES

Rotation Angle Y	Aspect Angle θ	Off-Axis Angle, Φ														
		-35.00	-30.00	-25.00	-20.00	-15.00	-10.00	-5.00	.00	5.00	10.00	15.00	20.00	25.00	30.00	35.00
0.	0.	5.38	5.38	5.38	5.38	5.38	5.38	5.38	5.38	5.38	5.38	5.38	5.38	5.38	5.38	5.38
0.	5.	5.73	6.01	6.28	6.53	6.75	6.96	7.14	7.30	7.44	7.55	7.64	7.71	7.75	7.77	7.77
0.	10.	5.68	6.29	6.87	7.40	7.86	8.26	8.59	8.86	9.07	9.22	9.31	9.35	9.34	9.24	9.19
0.	15.	5.17	6.25	7.21	8.04	8.74	9.31	9.76	10.10	10.33	10.45	10.48	10.42	10.28	10.07	9.79
0.	20.	4.24	5.91	7.32	8.48	9.42	10.15	10.69	11.06	11.26	11.31	11.21	10.99	10.65	10.20	9.66
0.	25.	2.86	5.30	7.23	8.75	9.93	10.81	11.41	11.77	11.91	11.83	11.57	11.12	10.51	9.74	8.85
0.	30.	.97	4.44	6.98	8.88	10.29	11.29	11.94	12.27	12.31	12.07	11.59	10.87	9.92	8.75	7.38
0.	35.	-1.42	3.39	6.60	8.88	10.51	11.62	12.29	12.57	12.49	12.07	11.33	10.28	8.93	7.26	5.29
0.	40.	-4.05	2.27	6.14	8.78	10.61	11.81	12.48	12.69	12.47	11.85	10.83	9.42	7.61	5.37	2.66
0.	45.	-5.74	1.22	5.63	8.59	10.58	11.86	12.53	12.66	12.29	11.45	10.14	8.36	6.09	3.28	-.11
0.	50.	-5.32	.45	5.11	8.30	10.45	11.78	12.44	12.48	11.97	10.91	9.33	7.21	4.55	1.39	-2.12
0.	55.	-3.86	.06	4.62	7.96	10.21	11.58	12.21	12.18	11.52	10.27	8.46	6.10	3.28	.19	-2.78
0.	60.	-2.56	-.00	4.17	7.54	9.86	11.27	11.87	11.75	10.97	9.57	7.60	5.16	2.44	-.26	-2.79
0.	65.	-1.72	.10	3.76	7.07	9.41	10.82	11.40	11.21	10.33	8.83	6.81	4.47	2.04	-.34	-3.21
0.	70.	-1.31	.21	3.36	6.61	8.84	10.25	10.79	10.55	9.61	8.08	6.13	4.02	1.89	-.66	-3.47
0.	75.	-1.29	.21	2.94	6.08	8.15	9.53	10.04	9.76	8.80	7.32	5.56	3.74	1.34	-1.39	-3.49
0.	80.	-1.58	.08	2.40	5.13	7.30	8.63	9.11	8.81	7.88	6.53	5.05	3.10	.61	-1.75	-3.43
0.	85.	-2.11	-.20	1.89	4.24	6.25	7.51	7.95	7.66	6.81	5.70	4.23	2.17	-.09	-2.01	-3.35
0.	90.	-2.79	-.61	1.20	3.16	4.93	6.08	6.48	6.21	5.52	4.56	3.04	1.12	-.79	-2.23	-3.27
0.	95.	-3.84	-1.12	.34	1.78	3.21	4.19	4.52	4.30	3.93	2.99	1.55	-.13	-1.55	-2.45	-4.32
0.	100.	-5.31	-2.88	-.86	-.03	.83	1.51	1.74	2.11	1.79	.89	-.41	-1.68	-2.53	-4.16	-6.13
0.	105.	-7.29	-5.58	-3.91	-2.93	-2.80	-2.21	-1.36	-1.05	-1.36	-2.21	-3.19	-3.98	-5.21	-6.84	-8.58

REPRODUCIBILITY OF THE
ORIGINAL PAGE IS POOR

TABLE A 6. ANTENNA GAIN IN DB FOR 5 ACTIVE ELEMENTS AND γ = 15 DEGREES

Rotation Angle γ	Aspect Angle θ	Off-Axis Angle, Φ														
		-35.00	-30.00	-25.00	-20.00	-15.00	-10.00	-5.00	.00	5.00	10.00	15.00	20.00	25.00	30.00	35.00
15.	0.	3.20	3.20	3.20	3.20	3.20	3.20	3.20	3.20	3.20	3.20	3.20	3.20	3.20	3.20	3.20
15.	5.	5.79	5.84	5.87	5.86	5.83	5.76	5.67	5.55	5.41	5.24	5.05	4.85	4.64	4.42	4.20
15.	10.	7.75	7.95	8.08	8.15	8.14	8.06	7.91	7.68	7.37	6.99	6.55	6.05	5.51	4.96	4.43
15.	15.	8.67	9.19	9.46	9.72	9.85	9.86	9.75	9.45	9.03	8.46	7.74	6.88	5.91	4.89	3.91
15.	20.	8.53	9.38	10.07	10.60	10.95	11.12	11.09	10.84	10.36	9.64	8.66	7.41	5.91	4.23	2.58
15.	25.	7.38	8.77	9.93	10.84	11.51	11.91	12.03	11.87	11.38	10.55	9.34	7.69	5.56	2.95	.23
15.	30.	5.16	7.35	9.13	10.54	11.58	12.28	12.61	12.56	12.11	11.22	9.81	7.78	4.94	1.01	-3.72
15.	35.	1.78	5.15	7.75	9.76	11.26	12.29	12.86	12.97	12.58	11.65	10.09	7.71	4.16	-1.55	-11.61
15.	40.	-2.66	2.38	5.96	8.84	10.63	12.01	12.84	13.12	12.81	11.88	10.19	7.54	3.40	-4.04	-18.39
15.	45.	-6.05	-.21	4.12	7.37	9.79	11.52	12.60	13.05	12.84	11.91	10.14	7.31	2.85	-4.51	-7.26
15.	50.	-6.13	-1.39	2.76	6.20	8.90	10.89	12.18	12.79	12.67	11.76	9.96	7.04	2.43	-2.90	-3.30
15.	55.	-5.46	-1.77	2.19	5.39	8.10	10.20	11.64	12.36	12.33	11.46	9.65	6.74	2.69	-1.14	-1.33
15.	60.	-4.43	-1.96	1.71	4.98	7.47	9.53	11.01	11.81	11.83	11.00	9.22	6.43	2.88	.09	-.38
15.	65.	-3.83	-1.78	1.25	4.46	7.05	8.91	10.33	11.13	11.19	10.40	8.69	6.09	3.04	.78	-.12
15.	70.	-3.75	-1.59	1.00	3.88	6.47	8.37	9.61	10.55	10.41	9.66	8.04	5.68	3.09	1.01	-.39
15.	75.	-4.10	-1.52	.84	3.35	5.76	7.68	8.85	9.45	9.47	8.76	7.27	5.20	2.96	.86	-1.14
15.	80.	-4.48	-1.60	.70	2.66	5.00	6.80	7.97	8.41	8.34	7.67	6.35	4.60	2.66	.49	-1.71
15.	85.	-4.75	-2.12	.52	2.35	4.15	5.76	6.86	7.24	6.97	6.33	5.24	3.86	2.19	-.33	-2.22
15.	90.	-5.04	-2.90	-.27	1.79	3.16	4.49	5.46	5.82	5.46	4.63	3.86	2.93	1.12	-1.26	-2.97
15.	95.	-5.40	-3.80	-1.58	.50	1.95	2.86	3.64	3.94	3.64	2.86	2.05	1.17	-.52	-2.47	-3.92
15.	100.	-5.83	-4.89	-3.27	-1.48	-.08	.67	1.09	1.29	1.09	.67	-.08	-1.48	-2.76	-4.03	-5.02
15.	105.	-7.26	-6.28	-5.59	-4.32	-3.15	-2.53	-2.60	-2.94	-2.60	-2.53	-3.15	-4.32	-5.59	-6.07	-6.98

*FIN

TABLE A 7. GAIN AS A FUNCTION OF ROTATION ANGLE FOR 5 ACTIVE ELEMENTS AND ψ = 0 DEGREES

φ	θ \ γ	Rotation Angle, γ - Degrees										
		-15.00	-12.00	-9.00	-6.00	-3.00	.00	3.00	6.00	9.00	12.00	15.00
0.	0.	3.20	3.43	3.74	4.03	4.23	4.31	4.23	4.03	3.74	3.43	3.20
0.	5.	5.55	5.97	6.34	6.63	6.81	6.87	6.81	6.63	6.34	5.97	5.55
0.	10.	7.68	8.08	8.40	8.64	8.79	8.84	8.79	8.64	8.40	8.08	7.68
0.	15.	9.45	9.76	10.01	10.19	10.30	10.34	10.30	10.19	10.01	9.76	9.45
0.	20.	10.84	11.06	11.24	11.37	11.45	11.47	11.45	11.37	11.24	11.06	10.84
0.	25.	11.87	12.02	12.14	12.23	12.28	12.30	12	12.23	12.14	12.02	11.87
0.	30.	12.56	12.67	12.75	12.81	12.84	12.85	12.84	12.81	12.75	12.67	12.56
0.	35.	12.97	13.04	13.10	13.14	13.17	13.18	13.17	13.14	13.10	13.04	12.97
0.	40.	13.12	13.18	13.23	13.27	13.29	13.30	13.29	13.27	13.23	13.18	13.12
0.	45.	13.05	13.11	13.16	13.20	13.22	13.23	13.22	13.20	13.16	13.11	13.05
0.	50.	12.79	1 86	12.92	12.97	12.99	13.00	12.99	12.97	12.92	12.86	12.79
0.	55.	12.36	12.46	12.53	12.58	12.61	12.62	12.61	12.58	12.53	12.46	12.36
0.	60.	11.81	11.91	12.00	12.06	12.10	12.11	12.10	12.06	12.00	11.91	11.81
0.	65.	11.13	11.25	11.34	11.41	11.45	11.46	11.45	11.41	11.34	11.25	11.13
0.	70.	10.35	10.46	10.56	10.62	10.67	10.68	10.67	10.62	10.56	10.46	10.35
0.	75.	9.45	9.55	9.64	9.70	9.74	9.75	9.74	9.70	9.64	9.55	9.45
0.	80.	8.41	8.49	8.55	8.60	8.64	8.65	8.64	8.60	8.55	8.49	8.41
0.	85.	7.24	7.22	7.25	7.28	7.30	7.31	7.30	7.28	7.25	7.22	7.24
0.	90.	5.82	5.79	5.72	5.62	5.62	5.63	5.62	5.62	5.72	5.79	5.82
0.	95.	3.94	3.91	3.83	3.71	3.54	3.39	3.54	3.7:	3.83	3.91	3.94
0.	100.	1.29	1.26	1.17	1.03	1.10	1.14	1.10	1.03	1.17	1.26	1.29
0.	10[illegible].	-2.94	-2.83	-2.47	-2.22	-2.06	-2.01	-2.06	-2.22	-2.47	-2.83	-2.94

$FIN

TABLE A 8 GAIN AS A FUNCTION OF ROTATION ANGLE FOR 5 ACTIVE ELEMENTS AND ψ = 10 DEGREES

φ	θ \ Υ	Rotation Angle, Υ - Degrees										
		-15.00	-12.00	-9.00	-6.00	-3.00	.00	3.00	6.00	9.00	12.00	15.00
10.	0.	3.20	3.43	3.74	4.03	4.23	4.31	4.25	4.03	3.74	3.43	3.20
10.	5.	5.76	6.15	6.47	6.70	6.82	6.81	6.68	6.43	6.09	5.68	5.24
10.	10.	8.06	8.37	8.59	8.72	8.75	8.68	8.51	8.25	7.90	7.48	6.99
10.	15.	9.86	10.04	10.16	10.20	10.16	10.05	9.87	9.62	9.29	8.91	8.46
10.	20.	11.12	11.21	11.25	11.23	11.16	11.03	10.85	10.62	10.34	10.01	9.64
10.	25.	11.91	11.94	11.93	11.88	11.79	11.67	11.52	11.32	11.10	10.84	10.55
10.	30.	12.28	12.28	12.26	12.21	12.13	12.03	11.91	11.77	11.60	11.42	11.22
10.	35.	12.29	12.30	12.29	12.26	12.22	12.15	12.06	11.99	11.89	11.78	11.65
10.	40.	12.01	12.05	12.08	12.09	12.09	12.07	12.05	12.02	11.98	11.93	11.88
10.	45.	11.52	11.60	11.67	11.73	11.79	11.83	11.86	11.89	11.90	11.91	11.91
10.	50.	10.89	11.02	11.14	11.25	11.35	11.45	11.53	11.61	11.67	11.72	11.76
10.	55.	10.20	10.37	10.53	10.68	10.83	10.96	11.09	11.20	11.30	11.39	11.46
10.	60.	9.53	9.71	9.89	10.06	10.23	10.40	10.55	10.69	10.81	10.92	11.00
10.	65.	8.91	9.08	9.25	9.42	9.60	9.76	9.92	10.07	10.20	10.31	10.40
10.	70.	8.37	8.49	8.63	8.77	8.92	9.07	9.22	9.35	9.47	9.58	9.66
10.	75.	7.88	7.91	8.01	8.10	8.20	8.31	8.42	8.52	8.62	8.70	8.76
10.	80.	6.80	7.03	7.24	7.38	7.41	7.45	7.50	7.56	7.61	7.64	7.67
10.	85.	5.76	5.97	6.16	6.33	6.45	6.47	6.44	6.41	6.39	6.36	6.33
10.	90.	4.49	4.66	4.82	4.95	5.05	5.11	5.12	5.00	4.87	4.75	4.63
10.	95.	2.86	2.97	3.08	3.16	3.21	3.22	3.17	3.06	2.88	2.76	2.86
10.	100.	.67	.66	.47	.66	.62	.54	.39	.40	.56	.65	.67
10.	105.	-2.53	-2.67	-2.93	-3.24	-3.48	-3.17	-2.90	-2.69	-2.55	-2.49	-2.53

*EIN